

Recent progress in quantum cascade lasers and applications

To cite this article: Claire Gmachl *et al* 2001 *Rep. Prog. Phys.* **64** 1533

View the [article online](#) for updates and enhancements.

You may also like

- [Observation and characterisation of trapped electron modes in Wendelstein 7-X](#)
A Krämer-Flecken, J H E Proll, G Weir et al.
- [Novel InP- and GaSb-based light sources for the near to far infrared](#)
Sprengel Stephan, Demmerle Frederic and Amann Markus-Christian
- [III-nitride semiconductors for intersubband optoelectronics: a review](#)
M Beeler, E Trichas and E Monroy

www.hidenanalytical.com
info@hiden.co.uk

HIDEN ANALYTICAL

Instruments for Advanced Science

Mass spectrometers for vacuum, gas, plasma and surface science

Residual Gas Analysis

Perform RGA at UHV/XHV. Our RGA configurations include systems for UHV science applications including temperature-programmed desorption and electron/photon stimulated desorption.

Thin Film Surface Analysis

Conduct both static and dynamic SIMS analysis with a choice of primary ions for full chemical composition and depth profiling. Our SIMS solutions include complete workstations and bolt-on modules.

Plasma Characterisation

Fully characterise a range of plasmas: RF, DC, ECR and pulsed plasmas, including neutrals and neutral radicals. Extend your analyses to atmospheric pressure processes using the HPR-60, with time-resolved mass/energy analysis.

www.HidenAnalytical.com info@hiden.co.uk

Recent progress in quantum cascade lasers and applications

Claire Gmachl, Federico Capasso, Deborah L Sivco and Alfred Y Cho

Bell Laboratories, Lucent Technologies, 600 Mountain Avenue, Murray Hill, NJ 07974, USA

E-mail: cg@lucent.com

Received 7 June 2001

Published 25 October 2001

Online at stacks.iop.org/RoPP/64/1533

Abstract

Quantum cascade ('QC') lasers are reviewed. These are semiconductor injection lasers based on intersubband transitions in a multiple-quantum-well (QW) heterostructure, designed by means of band-structure engineering and grown by molecular beam epitaxy. The intersubband nature of the optical transition has several key advantages. First, the emission wavelength is primarily a function of the QW thickness. This characteristic allows choosing well-understood and reliable semiconductors for the generation of light in a wavelength range unrelated to the material's energy bandgap. Second, a cascade process in which multiple—often several tens of—photons are generated per electron becomes feasible, as the electron remains inside the conduction band throughout its traversal of the active region. This cascading process is behind the intrinsic high-power capabilities of the lasers. Finally, intersubband transitions are characterized through an ultrafast carrier dynamics and the absence of the linewidth enhancement factor, with both features being expected to have significant impact on laser performance.

The first experimental demonstration by Faist *et al* in 1994 described a QC-laser emitting at $4.3\text{ }\mu\text{m}$ wavelength at cryogenic temperatures only. Since then, the lasers' performance has greatly improved, including operation spanning the mid- to far-infrared wavelength range from 3.5 to $24\text{ }\mu\text{m}$, peak power levels in the Watt range and above-room-temperature (RT) pulsed operation for wavelengths from 4.5 to $16\text{ }\mu\text{m}$. Three distinct designs of the active region, the so-called 'vertical' and 'diagonal' transition as well as the 'superlattice' active regions, respectively, have emerged, and are used either with conventional dielectric or surface-plasmon waveguides. Fabricated as distributed feedback lasers they provide continuously tunable single-mode emission in the mid-infrared wavelength range. This feature together with the high optical peak power and RT operation makes QC-lasers a prime choice for narrow-band light sources in mid-infrared trace gas sensing applications. Finally, a manifestation of the high-speed capabilities can be seen in actively and passively mode-locked QC-lasers, where pulses as short as a few picoseconds with a repetition rate around 10 GHz have been measured.

Contents

	Page
1. Introduction	1535
2. Basics of quantum cascade lasers	1537
2.1. Gain and loss	1539
2.2. Carrier transport	1542
3. Different designs of active regions	1544
3.1. Three-well vertical-transition active region	1544
3.2. Superlattice active region	1552
3.3. Diagonal transition active region	1559
4. Mid-infrared waveguides and resonators	1563
4.1. Fabry–Perot type quantum cascade lasers with dielectric waveguides	1563
4.2. Distributed feedback quantum cascade lasers	1566
4.3. Surface-plasmon waveguides	1573
4.4. Micro-cavity and whispering-gallery type resonators	1575
5. Special quantum cascade laser designs	1581
5.1. Multiple-wavelength superlattice laser	1581
5.2. Bi-directional, dual-wavelength, quantum cascade laser	1583
5.3. Injectorless quantum cascade laser	1585
6. High-speed operation of quantum cascade lasers	1586
6.1. Gain switching	1587
6.2. Active mode locking	1589
6.3. Evidence for passive mode locking	1591
7. Application to trace-gas detection by optical methods in the mid-infrared	1594
7.1. Single-mode tuning of distributed feedback lasers	1594
7.2. Direct and modulated absorption measurements	1595
7.3. Cavity ring-down spectroscopy	1596
7.4. Photo-acoustic spectroscopy	1596
7.5. Other types of spectroscopy	1597
8. Conclusion and outlook	1597
Acknowledgments	1598
References	1598

1. Introduction

Semiconductor injection lasers are mainstream devices greatly familiar to every scholar of physics at any level of sophistication. The first semiconductor laser was demonstrated in 1962. The invention of the double heterostructure laser (DHL) shortly thereafter by Kroemer in 1963 and its demonstration in the late sixties by Alferov and Hayashi and Panish allowed a dramatic reduction of the threshold current density and hence room temperature continuous wave operation. In the DHL the active region is sandwiched by semiconductors of larger bandgap. The resulting band discontinuities confine the injected carriers in the active region. Similarly, the attendant refractive index difference between the materials creates a waveguide forcing light generated by stimulated emission to propagate parallel to the layers. The next important step occurred with the invention of the quantum well (QW) laser by Dingle and Henry in 1974 and its demonstration in 1975. The QW laser is a DHL with multiple QWs at its core (active region). The use of QWs further reduces the threshold and allows some control over the wavelength by changing the QW thickness. Population inversion is achieved by a strong, forced current flow across the p–n junction formed between the p-contact region (valence band transport) and n-contact region (conduction band transport), which contained the active region QW. Light travelling along the QW experiences gain by stimulated emission and laser action if the loss per round-trip in the cavity is compensated by the gain. Laser light is then emitted from the end-facets of the thin slice of active material. This picture of the ideal semiconductor laser was disrupted in the early 1990s with the experimental demonstrations of alternative device and laser concepts. First, all-semiconductor vertical-cavity surface emitting lasers (VCSELs) had been proposed and demonstrated, in which the laser cavity is rotated by 90° to emit normal to the QW plane. Then, quantum-dot (QD) lasers, with fully quantized energy levels in both bands and a strongly inhomogeneously broadened gain spectrum, were demonstrated, allowing for pronounced temperature insensitivity in laser operation. Long-lived, blue and green emitting conventional semiconductor lasers made from the InGaN/GaN/AlGaN material system challenged the view that only high-purity and high-quality materials will provide commercially successful laser devices. These examples—and there would be more to name—depict the vitality enjoyed recently by the field of semiconductor laser research. Finally, in 1994 quantum cascade (QC) lasers were invented. They differ essential from conventional semiconductor lasers in that they typically do not involve a transition of the electron from the conduction band into the valence band. This report is dedicated to review the particulars of the QC-laser, its basics, strengths, state-of-the-art results, and applications.

That light amplification is possible in intersubband transitions, i.e. transitions between quantized energy states within one energy band of a semiconductor, was first predicted by Kazarinov and Suris in 1971 in a seminal paper [1] describing what would later be called a ‘diagonal’ or ‘photon-assisted’ tunneling transition. However, while the cascading of many stages as well as population inversion of electrons had been discussed, this structure could not achieve a uniform electric field or stable current flow due to space charge injection. The understanding of electron tunneling and relaxation rates was still in its infancy and the known ultrafast scattering by emission of optical phonons, typically in the order of a picosecond, made it appear unlikely that a laser could be achieved with a subband spacing larger than the optical phonon energy. A spontaneous emission time in the nanosecond range, i.e. several orders of magnitude slower than the non-radiative scattering events, supported the notion of a highly inefficient optical system. The stimulated optical emission time, however, easily approaches the fast non-radiative scattering times.

Recognizing that the fast non-radiative longitudinal optical (LO) phonon emission rate, rather than being a hindrance for intersubband laser action, can be harnessed for the laser

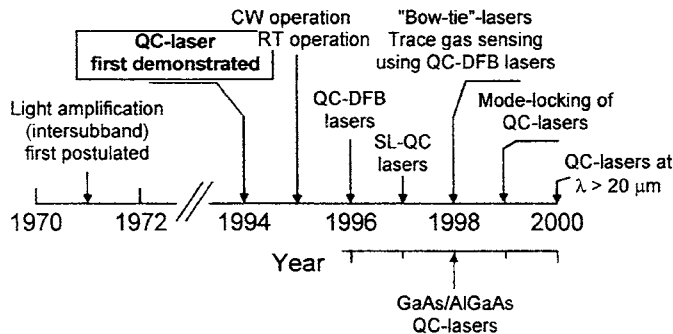


Figure 1. Schematic timeline of significant QC-laser developments.

process, Faist *et al* [2] demonstrated the first intersubband laser, designed to emit at $4.3 \mu\text{m}$ wavelength and grown by molecular beam epitaxy (MBE), in 1994. They named the new laser the ‘QC laser’. Progress advanced quickly after that; figure 1 shows a timeline. Already a year after their invention the lasers operated in cw at cryogenic temperatures [3], and in pulsed mode up to RT [4]. This rapid progress is mostly due to the quickly advancing understanding of how bandstructure engineering, pioneered by F Capasso, can be most successfully used to control the electron flow and thus increase population inversion and modal net gain, which ultimately controls the laser threshold.

After the first high-performance active region, the so-called ‘three well vertical’ design was established in a wavelength range from 5 to $11 \mu\text{m}$, the focus shifted to improved waveguide designs. Distributed feedback (DFB) lasers were first introduced in 1996 [5], providing continuously tunable single-mode laser output. Parallel to that, the quest for higher-power and longer-wavelength devices led to the invention of the superlattice active region in 1997 [6]. Rather than providing population inversion between subbands through careful design, minibands in active region superlattices achieve an intrinsic inversion and furthermore allow for large current flow. The latter is most valuable for large optical power, which is typically obtained for large current, and long wavelengths, where the larger losses require an active region able to sustain a large threshold current.

In the following year, the similarly researched QC micro-disc and micro-cylinder laser had evolved into the ‘bow-tie’ lasers, micro-lasers with distinct directionality and a several-order-of-magnitude increased optical output power [7]. QC-DFB lasers were demonstrated for the first time in trace-gas sensing applications [8], the pursuit of which is actively ongoing by many.

Until then, QC lasers had exclusively been demonstrated in the InGaAs/AlInAs on InP material system. In 1998, finally, Sirtori and coworkers [9] demonstrated the first QC laser in the GaAs/AlGaAs on GaAs material system, followed closely by other groups. The number of groups growing functional QC lasers amounts at present to approximately ten, with at least twice as many groups publishing in the field. More recently, starting in 1999, high-speed operation of QC lasers including mode locking was explored [10], and the first far-infrared QC lasers with wavelengths larger than $20 \mu\text{m}$, i.e. at 21.5 and $24 \mu\text{m}$, were demonstrated late in 2000 [11].

At present, efforts are underway to increase the maximum cw operating temperature of the lasers into the temperature range accessible with thermo-electric coolers and to RT [12]. This is a strong requirement for unlimited use of the lasers in trace-gas sensing applications. Other strong efforts focus on increasing the emission wavelength of the lasers into the Terahertz

regime, i.e. wavelengths longer than $50\text{ }\mu\text{m}$ [13], which includes an energy separation of the laser states smaller than one LO phonon, and on the opposite end of the wavelength scale to reduce the emission wavelength to $1.55\text{ }\mu\text{m}$, i.e. into the communications wavelength range [14]. The latter can only be achieved with a material system providing very large band offset, such as GaN/AlGaN or a few others.

We also notice a clear tendency to an increased family of material systems, for example the inclusion of InGaAs in the GaAs/AlGaAs system, or luminescence measurements on Sb-based electronic structures [15], as well as on Si/SiGe-based QC structures operating with holes in the valence band [16].

Fueled by and parallel to the QC laser, different types of cascaded semiconductor laser still based on an *interband* transition were developed. The so-called type-II cascade lasers, pioneered by Yang and coworkers [17], and greatly advanced by several groups [18], rely on diagonal, i.e. interwell, interband optical transitions with the electron entering the valence band, recombining with a hole and emitting light in its course. Accelerated by an applied electric field, the electron transfers back from the valence band into the conduction band in a region of the active material that is either a semimetal or has type-II band alignment, which allows very efficient re-tunneling of the electron into the conduction band, therefore allowing for repeated use of the electron, the key characteristic for the cascading process. These lasers have shown excellent performance particularly in the short-wavelength mid-infrared range around $4\text{--}5\text{ }\mu\text{m}$.

Another type of cascaded laser uses highly degenerate p–n transitions between conventional n–p laser active regions to allow re-transfer of the electron from the valence into the conduction band by Zener tunneling [19]. A differential power efficiency, i.e. number of photons per electron–hole pair injected through the contacts larger than unity has been measured.

The so-called ‘quantum-fountain’ laser, pioneered by Julien and coworkers [20], on the other hand, relies on optically pumped intersubband emission in an active region very similar to that of QC-lasers but does not include a cascading effect.

In parallel to the rapid development of the QC-lasers there has also been considerable progress in conventional, mid-infrared semiconductor lasers [21] and applications of all types of mid-infrared lasers, such as trace gas-sensing for pollution control and environmental monitoring, combustion diagnostics and medical diagnostics (breath analysis), or counter-measures. We are also pursuing free-space optical communications [22] in the two atmospheric windows ($3\text{--}5$ and $8\text{--}13\text{ }\mu\text{m}$).

This article is organized as follows. In section 2 we briefly discuss the basics of QC lasers; we shall give the basic considerations and equations that allow us to estimate and predict a laser’s performance. Section 3 then discusses different types of active region design, and section 4 does the same for the various waveguide designs used with QC lasers, including DFB designs. One strength of the QC laser is its large design flexibility; therefore, section 5 shows various examples of this design flexibility, where we discuss two types of multi-wavelength QC laser and a new ‘injectorless’ QC laser. Section 6 is focused on the high-speed capabilities of the lasers, and section 7 attempts to give an overview over the QC laser’s performance in various trace-gas sensing applications. A conclusion and outlook section completes the article.

2. Basics of quantum cascade lasers

QC lasers are based on intersubband transitions between quantized states in multiple-QW heterostructures. Despite the known ultra-fast carrier relaxation mechanisms within one band of a semiconductor, population inversion—which ultimately allows laser action—can

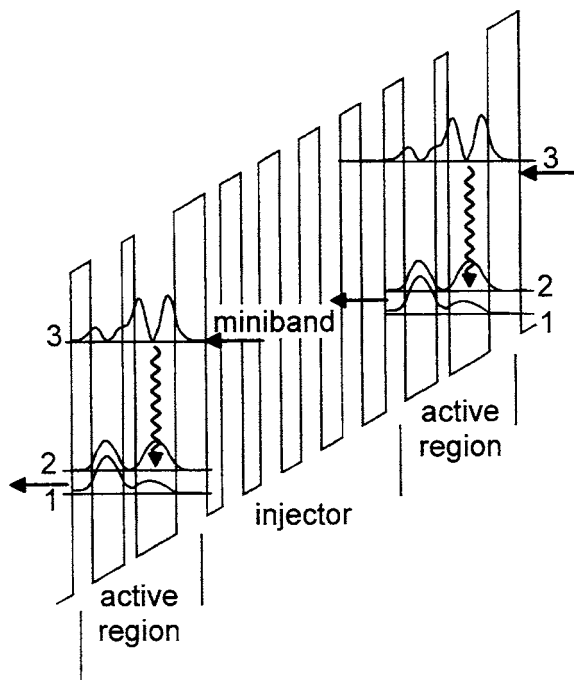


Figure 2. Schematic conduction band energy diagram of two QC-laser active regions with the intermediate injector region and the moduli squared of the wavefunctions involved in the laser transition (labelled 1, 2, and 3). The laser transition is indicated by the wavy arrows, and the electron flow by the straight arrows.

be achieved between such states by means of ‘band-structure engineering’ [23]. That entails that QW and barrier thicknesses and band-offset are designed, ‘engineered’, to tailor the fundamental properties of energy levels, carrier scattering rates, optical dipole matrix elements and tunneling times within given fundamental limits, to optimize population densities and transition probabilities for the various energy states. The designed structures are then grown by MBE, requiring the control for layer thicknesses between 0.5 to 10 nm, and through a total of 500–1000 subsequently grown layers. However, MBE is well suited to this task [24].

Figure 2 shows one of the simplest embodiments of a QC laser. Shown are two active regions, i.e. the QW and barrier regions that support the electronic states, between which the laser transition is taking place, and—schematically—the intermediate injector region. We draw the conduction band edge of InGaAs QWs and AlInAs barriers using the 520 meV low-temperature conduction band-offset usually associated with the materials’ compositions ($\text{In}_{0.53}\text{Ga}_{0.47}\text{As}$, $\text{Al}_{0.48}\text{In}_{0.52}\text{As}$) lattice matched to the InP substrate. An external electric field is applied as visualized by the linear slope of the electronic potential. Solving Schrödinger’s equation for this potential results in the energy levels drawn and the moduli squared of the wavefunctions; only the most interesting, first three confined states of each active region are drawn. The multiplicity of wavefunctions and energy levels in the injector region, its miniband, are shown only by a shaded polygon. Extrinsic electrons are supplied to the injector region through doping with silicon to a sheet density of typically $1\text{--}5 \times 10^{11} \text{ cm}^{-2}$ per period of active region and injector. This typically relates to a bulk doping level of $3\text{--}5 \times 10^{16} \text{ cm}^{-3}$. This low carrier density justifies solving only Schrödinger’s equation using the QW and external bias potential while neglecting an additional potential resulting from the ionized donors and

extrinsic electrons. As we shall see later, in special types of superlattice active region QC laser, the inclusion of this potential is essential.

In the particular example of figure 2 we chose the QW thicknesses in the active region as 6.0 and 4.7 nm, and the thickness of the intermediate barrier as 1.6 nm. This results in energy separations between levels 3 and 2 of 207 meV (corresponding to a wavelength of 6.0 μm) and between levels 2 and 1 of 37 meV. The latter is deliberately chosen to be very close to the energy of the LO phonon modes of the InGaAs/AlInAs/active region materials.

Under an appropriate applied bias—in the case of figure 2, where the applied electric field is 62 kV cm⁻¹, 0.29 V per stage of active region and injector—electrons tunnel from the injector region into energy level 3, the upper laser state, of the active region. Electrons scatter from this level into both lower-lying levels 2 and 1, very rapidly emitting LO phonons. We calculate scattering times, using a Froehlich interaction model, of $\tau_{32} = 2.2$ ps and $\tau_{31} = 2.1$ ps. This results in a total upper-state lifetime of $\tau_3 = 1/(1/\tau_{32} + 1/\tau_{31}) = 1.1$ ps. Similarly, we calculate a scattering time between levels 2, the lower laser state, and level 1 of $\tau_{21} = \tau_2 = 0.3$ ps. This scattering time is ultra-short due to the resonant nature of this transition with the LO phonon. With $\tau_{32} \gg \tau_2$ we also immediately recognize the population inversion occurring between the laser levels 3 and 2. Laser action is possible. Electrons need only be supplied fast enough into level 3, by tunneling from the preceding injector region, and need to exit from levels 2 and more so from level 1 into the following downstream injector region at a high rate by tunneling. Inside this injector region and brought about by the externally applied electric field, electrons gain again in energy (relative to the band bottom) and are injected into the following downstream active region. Typical QC lasers have a cascade containing 20–30 active regions alternated with injector regions, although laser action has been achieved for a single active region [25], and has been tested for as many as 100 active regions [26].

2.1. Gain and loss

Using the scattering times established in the previous section and calculating the optical dipole matrix element $z_{32} = 2.0$ nm, we can estimate the gain that we can achieve from this structure. The gain coefficient follows from the usual rate equation model with inclusion of a phenomenological broadening of the transition (which includes the Fermi-distributions in states 3 and 2) and is given by [4]:

$$g = \tau_3 \left(1 - \frac{\tau_2}{\tau_{32}}\right) \frac{4\pi e z_{32}^2}{\lambda_0 \varepsilon_0 n_{\text{eff}} L_p} \frac{1}{2\gamma_{32}} \quad (1)$$

where g is the gain coefficient, λ_0 (= 6.0 μm for the structure in figure 2) the wavelength in vacuum, ε_0 the vacuum dielectric constant, e the elementary charge, n_{eff} (= 3.25) the effective refractive index of the mode, L_p (= 47 nm) the length (thickness) of one period of active region and injector and $2\gamma_{32}$ (estimated from measurements as 20 meV) the full width at half maximum value of the luminescence spectrum. For the example in figure 2 we obtain a gain coefficient of 30 cm kA⁻¹.

The derivation of equation (1) follows very closely any textbook derivation of gain in a semiconductor QW laser. However, one difference should be pointed out; we include here as the length of the active region the total length of one period of active region and injector although the optical transition is taking place only in a small portion of this region. This is equivalent to defining an equivalent, distributed, gain coefficient, and will be appropriately taken into account in the later calculation of the threshold current, when the optical confinement of the mode is similarly taken as distributed over active regions and injectors alike. However, it is a deliberate choice of normalization of gain per period, recognizing the importance of the injector region for laser action.

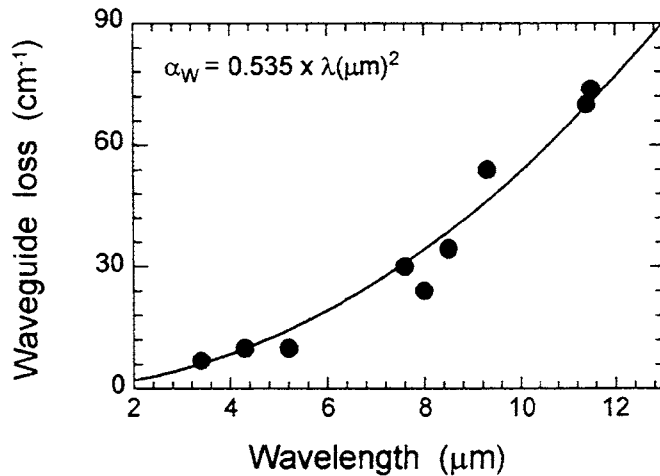


Figure 3. Measured waveguide loss versus mid-infrared wavelength (circles) for several QC-lasers. The solid curve is a least-square quadratic fit to the data.

After determining the gain coefficient, i.e. gain per current density, the second important factor for the threshold current are the losses experienced by the light traveling in the waveguide. Three major losses are discernible. First, the laser resonator will be formed by two semi-transparent mirrors, typically un-coated, as-cleaved, and parallel semiconductor facets. They provide a reflectivity of $R = ((n_{\text{eff}} - 1)/(n_{\text{eff}} + 1))^2$ each. This results in a mirror- or outcoupling loss of $\alpha_m = (1/L) \cdot (\ln(R))$, with L being the length of the resonator. This loss can certainly be reduced/enlarged using high-reflection/anti-reflection coating at the mirror facets. As an additional outcoupling loss one could include scattering losses and roughness scattering at imperfections. Quantifying these losses is however difficult.

The second important source of losses is free-carrier absorption in the doped semiconductor regions and the metallic contact layers. While the influence of the metallic layers can be suppressed as will be shown later in section 4.1, the semiconductor Drude losses are unavoidable. We shall call them waveguide losses α_w . Figure 3 shows measured values of the waveguide losses for various QC lasers in the wavelength range from 5 to 11 μm. As one can see, the loss increases approximately quadratically with the wavelength, as expected from a simple Drude model [27].

A third source of potential absorption losses are resonant intersubband transitions. Due to the considerable optical dipole matrix element of interminiband transitions, it is in general conceivable that the extrinsic electrons in the injector region can cause significant absorption if there are optical transitions resonant with the laser wavelength present. It is therefore necessary, but generally achievable, during the design of the QC-laser active regions and injectors that such resonantly absorbing intersubband or interminiband transitions are avoided.

Having established the loss mechanisms for our laser, we can continue to give an equation for the threshold current density J_{th} , as

$$J_{\text{th}} = \frac{\alpha_w + \alpha_m}{g\Gamma} \quad (2)$$

where Γ is the confinement factor, i.e. the overlap of the guided mode with the stack of active regions and injectors. The number of stages in the cascade enters the threshold current density via that quantity. For the exemplary structure of figure 2, and assuming mirror losses of

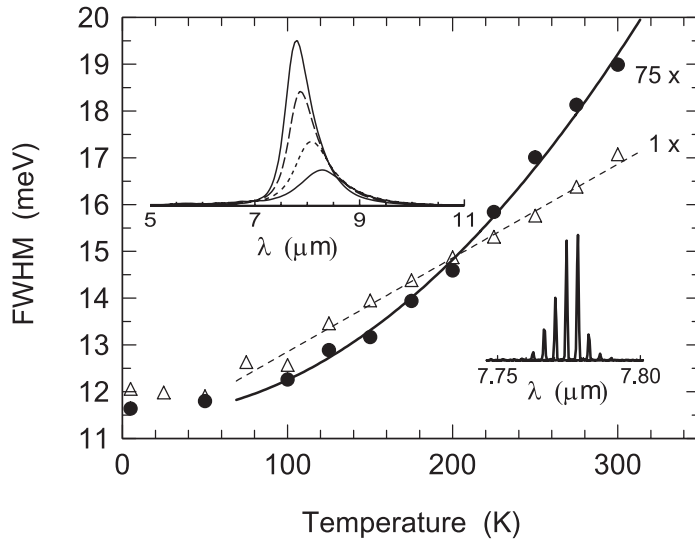


Figure 4. Measured full width at half maximum (FWHM) of the luminescence emission line as a function of the heat sink temperature for two samples with $N_p = 1$ (open triangles) and 75 (solid circles) stages of active regions and injectors. The solid curves represent best-fits to the data, for $T \geq 75$ K. The devices are driven at constant current density levels of 26.5 and 8.8 kA cm⁻², respectively. These levels were chosen to result in comparable linewidths at low temperatures. Upper inset, electro-luminescence spectra measured at four different heat sink temperatures (100, 150, 225, 300 K—top to bottom) from the device containing $N_p = 75$ stages. Lower inset, a typical laser spectrum.

$\alpha_m = 5.1$ cm⁻¹ for a cavity length of 2.5 mm and waveguide losses $\alpha_w = 19$ cm⁻¹ from figure 3, this results in a threshold current density of 1.6 kA cm⁻². This value is typical for a simple two-well active region structure; however, by optimizing the design within more complicated structures, a threshold current density as low as 0.2–0.5 kA cm⁻² can be achieved.

So far the threshold current density has been described only for low, cryogenic temperature. One can safely assume that the waveguide loss, mirror loss and confinement factor remain practically unchanged with temperature, hereby neglecting thermally generated free carriers and changes in the electron band structure, which could result in resonant absorption. The gain coefficient, however, is clearly temperature dependent. Electron scattering times for LO phonon emission are reduced by the Bose factor through the larger phonon population at higher temperatures. Typically, the scattering times are reduced by a factor of two from cryogenic to RT. In addition, the width of the gain spectrum is broadened at higher temperatures, again amounting to roughly a factor of two between cryogenic and RT. An example of a measured luminescence spectrum as a function of temperature is shown in figure 4. As reasons can be cited the larger thermal spread of carriers, which makes non-parabolicity effects more visible [28], increases in other electron scattering mechanisms, such as impurity and interface roughness scattering, and others. There are no quantitative measurements of the determining factors, yet. Finally, extrinsic electrons from the injector region can thermally be back excited into the bottom laser level, where they reduce population inversion. A modified, temperature-dependent gain and threshold current density has been given by Faist *et al* [29], and reasonable agreement with the experiment has been observed.

$$J_{\text{th}} = \frac{1}{\tau_3(T) \left(1 - \frac{\tau_2(T)}{\tau_{32}(T)}\right)} \left[\frac{\varepsilon_0 n_{\text{eff}} L_p \lambda_0 (2\gamma_{32}(T))}{4\pi e \zeta_{32}^2} \cdot \frac{\alpha_w + \alpha_m}{\Gamma} + e n_g \exp\left(-\frac{\Delta}{kT}\right) \right] \quad (3a)$$

where

$$\tau_i(T) = \tau_{i0} \frac{1}{1 + \frac{2}{\exp\left(\frac{E_{LO}}{kT}\right) - 1}} \quad i = 1, 2, 3 \quad (3b)$$

and τ_{i0} is the scattering time at low temperature, E_{LO} the LO-phonon energy, k the Boltzmann constant, T the temperature, n_g the carrier sheet density in the injector ground state and Δ the energy separation between the injector ground state and level 2 of the preceding active region.

Nevertheless, for QC lasers as well as for conventional semiconductor lasers a typical description of the temperature dependence of the laser threshold invoking a so-called ‘characteristic temperature, T_0 ’ has proven useful.

$$J_{th}(T) = J_0 \exp\left(\frac{T}{T_0}\right). \quad (4a)$$

Typically a single T_0 value can be found in the temperature range between 100 and 300 K. It ranges for the different QC lasers and laser types from 100 to 200 K, which is a very large value compared with all other semiconductor lasers, which typically have T_0 values below 100 K. Sometimes a modified version of equation (4a) is used,

$$J_{th}(T) = J_0 \exp\left(\frac{T}{T_0}\right) + J_1 \quad (4b)$$

which then typically allows us to fit the threshold current versus temperature over the entire temperature range of laser operation, i.e. from 4.2 K to above RT. Splitting off a constant, temperature independent portion of the threshold current proved useful in particular for superlattice active region QC-lasers.

After the calculation of the laser threshold, knowledge of the loss mechanisms also lets us estimate the slope efficiency, i.e. the increase in optical power (per outcoupling facet) per unit current, as

$$\frac{\partial P}{\partial I} = \frac{1}{2} \frac{h\nu}{e} N_p \frac{\alpha_m}{\alpha_m + \alpha_w} \left(1 - \frac{\tau_2}{\tau_{32}}\right) \quad (5)$$

where $h\nu$ is the photon energy and N_p the number of stages of active regions and injectors. It is obvious that a large number of stages will result in a large slope efficiency, and subsequently a large optical output power in general; values in the range of W A^{-1} and W , respectively, are common. A study of the performance of QC lasers as a function of the number of stages also demonstrated what we termed ‘unit cascade efficiency’, i.e. that within the experimental error all stages of a cascade are in fact participating in laser action. We demonstrated this experimentally for the case of a very high-performance QC-laser structure around 8 μm wavelength [30].

2.2. Carrier transport

The previous section described how QC-laser action can be achieved by carefully designing layer thicknesses and electric field in the active region of a QC laser to achieve population inversion between states 3 and 2, the upper and lower laser state respectively. This discussion, however, assumed that electrons are sufficiently quickly and exclusively injected into level 3 from the preceding injector region, and can exit from the bottom states 2 and 1 into the following injector equally fast, such that those states are practically devoid of electrons. In the following we will discuss whether and to what extent this assumptions hold up to in-depth scrutiny. For the structure in figure 2 electrons are injected into level 3 from the injector ground state g through the injection barrier I by resonant tunneling. The injection barrier is tailored

in thickness such that in resonance, i.e. under fully ‘anti-crossed’ conditions, states 3 and g are split, separated in energy, by $\Delta E = \hbar\Omega = 4\text{--}6\text{ meV}$. At exact resonance and in the strong coupling regime a tunneling time and current density of

$$\tau_{\text{tunnel}} \approx \frac{\hbar}{2 \cdot \Delta E} \quad (6a)$$

and

$$J = \frac{en_g}{2\tau_3} \quad (6b)$$

respectively, can then be calculated [31]. Typical tunneling times are sub-picosecond and current densities are determined by the doping level. The latter is chosen as low as possible, to reduce the waveguide loss, but large enough to support the maximum current as needed. Similarly, the exit barrier is designed to allow fast sub-picosecond tunneling out of the active region by similar deliberation.

If the applied bias is too low, no current will flow, and similarly if the bias is raised too high, resonant injection will cease and laser action will stop, often suddenly. The latter allows information about the number of free carriers in the active and injector regions. While equations (6) only describe the situation at maximum anti-crossing, i.e. fully resonant conditions, sufficient tunneling current can flow over a certain range of applied electric fields. Remember, for laser action the current has only to be large enough that the gain compensates the loss. Therefore, for a QC laser with a large gain coefficient and a low-loss waveguide, laser action can be observed for a wide range of electric fields, e.g. from 45 to 70 kV cm⁻¹ for the example of [30].

So far, the ideal carrier transport path has been described, i.e. electrons following the path $g \rightarrow 3 \rightarrow 2 \rightarrow 1$ and back into the injector and via thermalization and, if possible, relaxation via LO phonons to the next level g of the following down-stream stage. However, in reality other scattering paths for the electrons are conceivable, and will add to the threshold current as leakage currents. Figure 5 shows a revised version of figure 2 including these detrimental current paths. It is part of the optimization of QC-laser designs to minimize their effect.

First, scattering from the injector ground state directly into the bottom states 2 and 1 bypasses the laser transition $3 \rightarrow 2$. This can be treated as a parallel current to the actual laser current and is usually described by an injection efficiency η into the upper state 3. Similarly, electrons can scatter directly from state 3 into lower states of the injector. This amounts to a shorter upper laser state lifetime τ_3 , and therefore, directly reduces the gain coefficient. Hereby it is important to note that the injector regions are typically designed to provide electron Bragg reflection, i.e. a region of low electron probability density, around the energy range of the upper laser state. This effectively suppresses resonant tunneling out of level 3 and was the key improvement beyond the very first QC-laser, early on allowing for cw operation [3].

Finally, and in particular in short-wavelength lasers, where the upper laser state 3 is located energetically high up in the band and close to the quasi-continuum above the barriers, electrons may experience thermal excitation, i.e. thermionic emission, from the confined states, or even at low temperatures tunneling into the continuum. Once in the continuum, electrons are freely accelerated by the electric field and are not expected to participate in laser action any longer (until they thermalize back into the structure, if at all). The next section will demonstrate how several optimized QC-laser designs minimize the influence of these unwanted current paths.

Finally, we would like to note that much of the above assumes that electrons are injected from the injector ground state directly into the upper laser state. It ensures as fast and efficient filling of the upper laser state as possible. However, recent work by Scamarcio *et al* [32] used resonant tunneling injection of electrons from the injector ground state into a state one

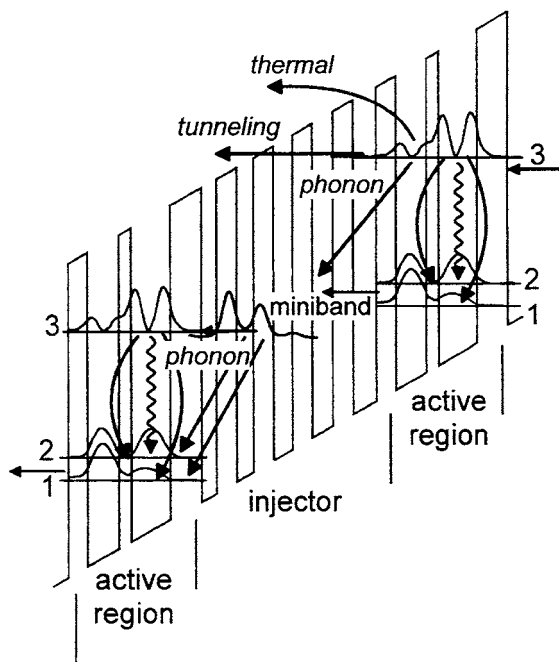


Figure 5. Conduction-band structure of the QC-laser design of figure 2; the modulus squared of the injector ground-state wavefunction is added. The additional arrows indicate the various electron scattering mechanisms beyond those participating in laser action (figure 2).

LO-phonon energy above the designated upper laser state. This has the advantage that with changing electric field the upper laser level is less perturbed, since it is not undergoing anti-crossing with the injector ground state, and is able to keep a large optical matrix dipole element over a larger range of applied bias. In a companion paper, Scamarcio *et al* also discuss electron thermalization in QC-related miniband structures [33].

3. Different designs of active regions

Since their inception in 1994 many designs of QC lasers have emerged, and can basically be characterized by their number of QWs in the active region (1–8 have been used so far) and the spatial extent and number of the wavefunctions in the active regions. A few characteristic and high-performance structures will be reviewed in the following.

3.1. Three-well vertical-transition active region

In the so-called ‘three-well vertical’ transition a thin well is inserted between the injector region and an active region similar to the one described in section 2 (which could also be termed a ‘two-well vertical-transition active region’). The additional QW leads to a significant reduction of electron scattering (leakage) from the injector directly into the laser ground state 2 and also level 1. The improvement led to the first high-performance, RT operation of QC lasers [4]. Here, we want to focus on one particular laser design, emitting at $8\text{ }\mu\text{m}$ wavelength, which has been extensively used for various studies due to its high optical gain and concomitant robustness for laser action [30].

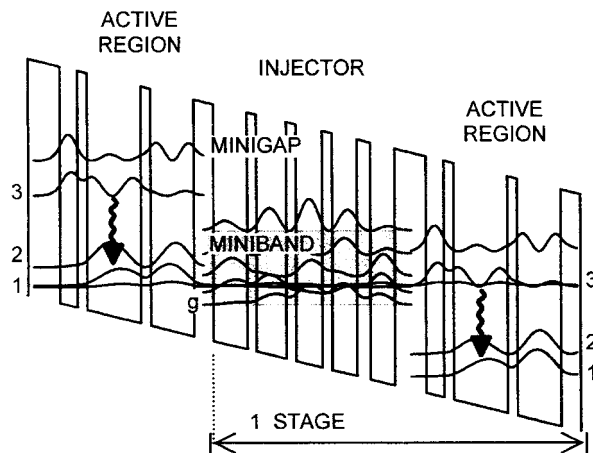


Figure 6. Conduction band diagram of two active regions with the intermediate injector region and the moduli squared of the wavefunctions involved in the laser transition. The wavy arrows indicate the laser transition. The layer thicknesses in nanometres of one period of active material and injector are, from left to right starting from the injection barrier (left-most layer): **3.8/2.1/1.2/6.5/1.2/5.3/**2.3**/4.0/I.**1**/3.6/I.**2**/3.2/I.**2**/3.0/I.**6**/3.0**. The underlined layers are n-type doped. The barriers are indicated in bold symbols; italic style shows the injector region. The applied electric field is 45 kV cm⁻¹.

A portion of the active material conduction-band structure, two active regions with the intermediate injector/relaxation region, is shown in figure 6. The active region consists of three InGaAs QWs closely coupled by thin AlInAs barriers. At the electric field of 45 kV cm⁻¹, corresponding to the measured laser threshold, the upper laser level (level 3) is separated from the lower laser level (level 2) by $E_{32} = 153.6$ meV ($\lambda_0 = 8.08 \mu\text{m}$). The LO-phonon scattering time τ_{32} between the two levels is calculated as 3.1 ps and the dipole matrix element of the optical transition as $z_{32} = 1.9$ nm. The lower laser level is closely coupled to the ground state (level 1) of the active material, such that the two levels are strongly anti-crossed. This increases the matrix element z_{32} with respect to z_{31} and maximizes τ_{32} with respect to τ_{31} . The energy difference is $E_{21} = 38.3$ meV, designed to efficiently deplete the lower laser level of electrons via resonant LO-phonon scattering ($E_{\text{LO}} \approx 34$ meV). The corresponding lifetime is calculated as $\tau_2 \approx \tau_{21} = 0.3$ ps $\ll \tau_{32} = 3.1$ ps. The LO-phonon scattering time from level 3 to level 1 is $\tau_{31} = 3.6$ ps, and the scattering time into all states of the following injector region is estimated as $\tau_{3i} = 14.6$ ps, i.e. significantly longer than intra-active region scattering times.

The injector ‘miniband’—more accurately, the manifold of energy levels in the injector—has been designed as ‘flat’. Its ground level is located 40 meV in energy below the upper laser level. Even the next-higher level of the injector miniband is energetically lower (14 meV) than the upper laser level. The injector has been doped in the centre part resulting in an electron sheet density of $n_g = 1.6 \times 10^{11} \text{ cm}^{-2}$ per period. This results in a quasi-Fermi level of ≈ 7.5 meV under operating conditions. This level scheme implies that at laser threshold, electrons are not injected from the Fermi-surface into the upper laser level. Furthermore level 1 of the preceding active region is in resonance with level 3 of the following active region, allowing for resonant carrier transport between successive active regions without significant carrier relaxation in the injector. We estimate a transit-time through the superlattice injector (length 21.9 nm, ‘width’ of the miniband ≈ 150 meV) of ≈ 0.5 ps. In comparison, the relaxation time within the injector is long since the energy separation to the adjacent lower energy level is well below the

LO-phonon energy and the ground level of the injector region is partly filled with electrons.

The advantage of this design is that it avoids a too early ‘shut-down’ of the laser due to suppression of resonant tunneling [31]. Once the electric field is increased above 45 kV cm^{-1} and the resonance between levels 1 and 3 is destroyed, there is still strong injection from the ground state of the injector, allowing for a wide dynamical range of current and concomitant high optical power.

From the values of τ_2 , τ_3 , τ_{32} and z_{32} and the measured value of the luminescence linewidth ($2\gamma_{32} \approx 10 \text{ meV}$) we calculate the gain coefficient g from equation (1) using $L_p (= 44.3 \text{ nm})$ the length of one period, $n_{\text{eff}} (= 3.27)$ the effective refractive index of the waveguide and $\lambda_0 (= 8.0 \mu\text{m})$ the emission wavelength as $g \approx 60 \text{ cm kA}^{-1}$ [34].

The mirror-losses α_m for a $L = 2.25 \text{ mm}$ long laser with as-cleaved facets are calculated as 5.59 cm^{-1} . The waveguide losses at threshold have been measured from sub-threshold spectra using the Hakki–Paoli method [35] resulting in $\alpha_w \approx 24 \text{ cm}^{-1}$. These values allow us to estimate the threshold current density using equation (2) and $\Gamma (= 0.5)$, the confinement factor of the laser mode for the entire stack of 30 periods of active regions and injectors, as $J_{\text{th}} = 0.98 \text{ kA cm}^{-2}$. This is in excellent agreement with the experimental value of $J_{\text{th}} \approx 1 \text{ kA cm}^{-2}$.

The slope efficiency—the increase in output laser power per unit current increase above threshold—is given by $\partial P / \partial I = 394 \text{ mW A}^{-1}$ per facet for $N_p = 30$. This is similarly in very good agreement with the experimental value of $\approx 400 \text{ mW A}^{-1}$.

This good agreement between calculated and experimentally measured values implies that besides excellent growth quality, the major physical effects are understood to a satisfactory degree; i.e. we can account for about almost all electrons traversing the structure. Being confident about the quality of this material, we used it for our study of the dependence of the device performance on the number of stages in QC lasers, which ranged from $N_p = 1$ to 75 [30], with a QC laser with $N_p = 100$ grown at a later time, and with a lower-loss waveguide [26]. While laser action from a QC laser with only one stage ($N_p = 1$) [25] is remarkable as it underlines the high optical gain that can be achieved by bandgap engineering, the QC laser with $N_p = 100$ stages—and a few watts of peak output power—highlights the cascading scheme, that allows stacking a very large number of active regions into a single cascade. Figures 7–10 summarize the results of the study on the dependence on N_p .

The most important consequence of the variation of N_p for waveguide considerations is the increase in the confinement factor Γ with increasing N_p . The confinement factor grows approximately linearly with the number of stages up to $N_p \approx 30 (\Gamma(30) = 0.49)$ and saturates visibly for higher N_p . We calculate $\Gamma(75) = 0.81$, $\Gamma(100) = 0.88$ and $\Gamma(200) = 0.97$.

The threshold current density $J_{\text{th}}(N_p)$ can be estimated using the gain coefficient g , the sum of the losses ($\alpha_w + \alpha_m$) and the confinement factor $\Gamma(N_p)$, as

$$J_{\text{th}}(N_p) = \frac{\alpha_m + \alpha_w}{g \cdot \Gamma(N_p)}. \quad (7)$$

Figure 7 shows the calculated function $J_{\text{th}}(N_p)$ using the previously obtained fit function for $\Gamma(N_p)$. The experimental values of J_{th} measured in pulsed as well as in cw mode are also displayed. A low-temperature threshold current density $J_{\text{th}} \leq 2 \text{ kA cm}^{-2}$ is consistently achieved for $N_p \geq 15$. For smaller N_p , J_{th} rises rapidly, approximately proportional to N_p^{-1} , as a direct consequence of the reduced confinement factor. Selected values of J_{th} , measured in pulsed mode at 10 K, are 25.6 kA cm^{-2} ($N_p = 1$), 3.68 kA cm^{-2} (12), 1.38 kA cm^{-2} (30) and 0.72 kA cm^{-2} (75). At this low temperature, the cw threshold current density does not significantly differ from the pulsed value. Cw operation has been obtained for samples with $N_p = 3$ –30.

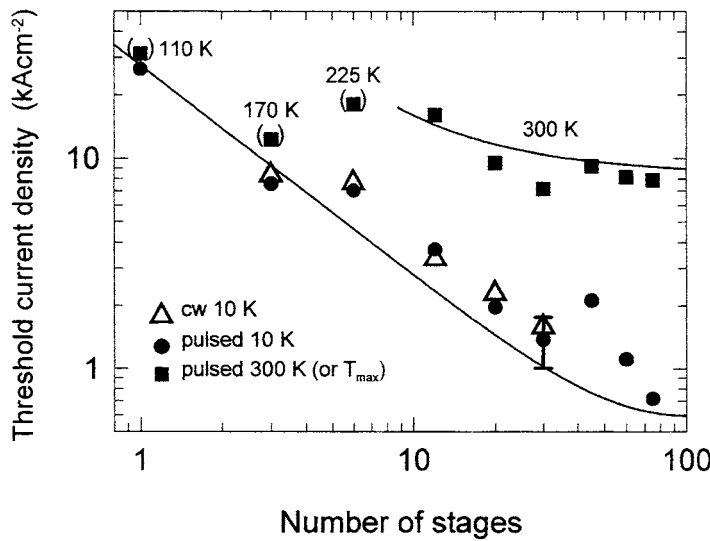


Figure 7. Threshold current density as a function of the number of stages measured at cryogenic temperatures in pulsed mode (solid circles) and in cw mode (open triangles), and in pulsed mode at RT (solid squares). Lasers with $N_p \leq 6$ stages did not show laser action at RT. The respective highest operating temperature is displayed. The solid curves are calculated for cryogenic temperature and RT. The error-bar shown for the $N_p = 30$ -stage device indicates the range of values that are obtained for nominally identical devices from a variety of wafers and processing cycles.

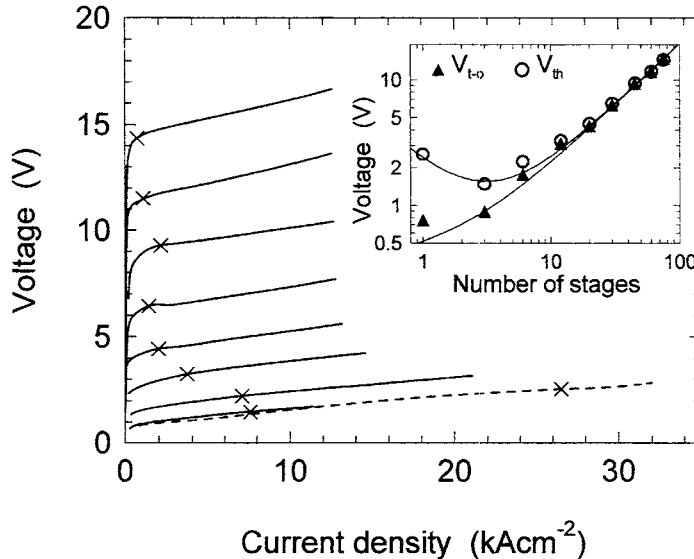


Figure 8. Voltage-current characteristics of various QC-laser devices with $N_p = 1, 3, 6, 12, 20, 30, 45, 60$, and 75 ; the uppermost trace corresponds to the sample with $N_p = 75$ stages, the lowermost to $N_p = 3$. The trace of $N_p = 1$ is drawn as a dashed curve. The 'x' on each curve denotes the voltage at which the laser threshold is reached. Inset, turn-on voltage (V_{to} , solid triangles) and threshold voltage (V_{th} , open circles) as a function of N_p . The symbols indicate measured data, the solid curves model calculations.

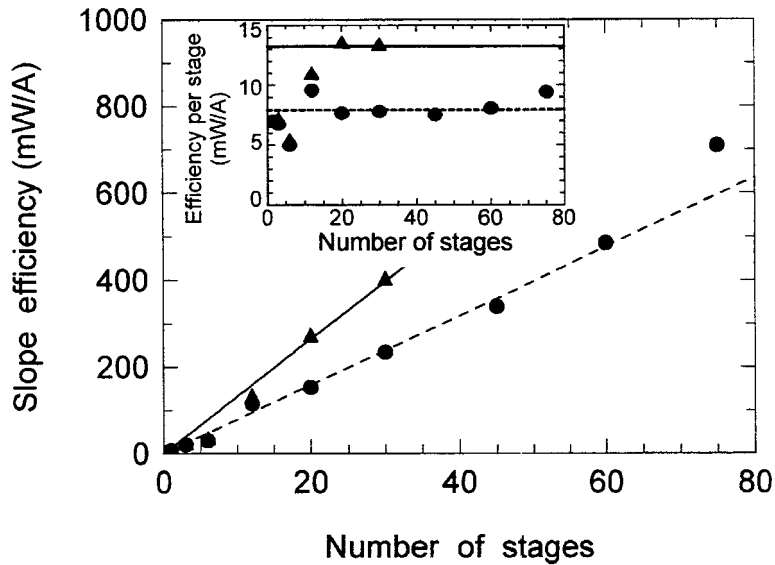


Figure 9. Measured slope efficiency per facet as a function of N_p ; the triangles correspond to data obtained in cw, the circles to pulsed data. The curves are the best fit to the data. The discrepancy between the two curves is due to the different collection efficiencies of the two measurements: $\sim 100\%$ for cw, and $\sim 60\%$ for pulsed. The data have been obtained at cryogenic temperatures. However, the slope efficiency degrades only marginally with temperature (e.g., for $N_p = 75$, the slope efficiency remains essentially constant up to 200 K). Inset, slope efficiency per facet *per stage* as a function of N_p , for the same conditions as in the main graph.

Devices with $N_p \geq 12$ stages displayed laser action in pulsed mode at and above RT. The respective threshold current densities, ranging from 16.0 kA cm^{-2} ($N_p = 12$) to 7.9 kA cm^{-2} (75), are shown in figure 7. Conversely, the samples with six, three and one stages were limited to maximum pulsed operating temperatures of 225, 170 and 110 K, respectively. We can then calculate the expected value of J_{th} at RT as a function of N_p , following [29] and equation (3) and using the previously obtained fit function for $\Gamma(N_p)$. The theoretical predictions coincide well with the data, as can be seen in figure 7, resulting in $J_{\text{th}} \leq 10 \text{ kA cm}^{-2}$ for $N_p \geq 20$.

For each laser, the threshold current density was measured as a function of the temperature recorded at the laser heat sink. These data can be well fitted for each device over the entire temperature range, 10–300 K, with the empirical function (see also equation (4b))

$$J_{\text{th}}(T; N_p) = J_0(N_p) \cdot \exp(T/T_0) + J_1(N_p). \quad (8)$$

For $N_p \geq 20$, the parameters, in particular $J_0 \approx 0.4 \text{ kA cm}^{-2}$ and $T_0 \approx 100 \text{ K}$, are almost constant, confirming that the temperature performance is largely independent of the number of stages. However, as N_p falls below 20, T_0 drops sharply and J_1 rises while J_0 is decreased for small N_p . The latter may partly be a numerical effect from the reduced temperature range over which the fit-function is taken, and from the already high value of J_{th} at low temperatures. However, numerical effects do not account for the drop in T_0 . We explain it by two effects: first, the large threshold currents of low- N_p devices and the concomitant high injected carrier densities result in an increased value of $2\gamma_{32}$ [25], which in turn decreases the gain coefficient. Second, carrier heating becomes important as the dissipated power is increased with increasing threshold current, again resulting in an excess $2\gamma_{32}$. As is easily understood, both effects enhance each other.

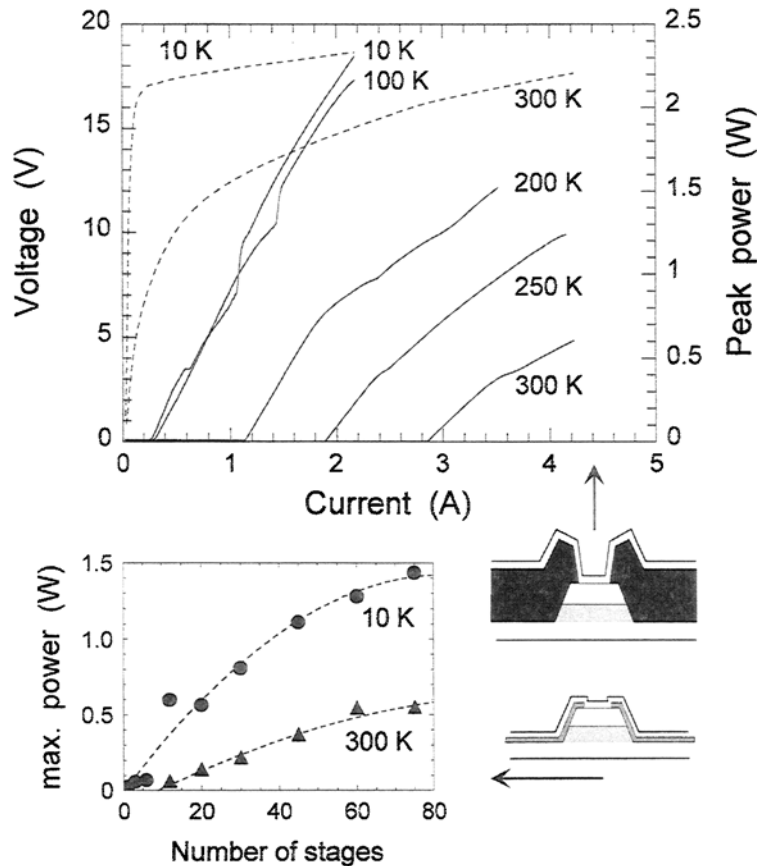


Figure 10. Light output versus current (solid) and voltage versus current (dashed) characteristics at various heat-sink temperatures of the laser containing $N_p = 100$ active region and injector stages. The collection efficiency is $\sim 90\%$, and the power is collected from one facet. The device is driven in pulsed mode. Lower left inset, maximum peak power as a function of N_p measured for various lasers in pulsed mode at 10 and 300 K heat sink temperature (symbols). The dashed curves are a guide to the eyes. Lower right inset, cross-sections of the various device layouts used for those measurements.

Figure 8 shows the measured current–voltage (I – V) characteristics for all wafers at low temperature. The energy drop per stage is given by $E_{32}+E_{21}=E_{\text{Photon}}+E_{\text{LO-Phonon}}=193\text{ meV}$, and the voltage drop across the entire N_p -stage cascade is given by

$$V_S(N_p)=\frac{(E_{32}+E_{21})}{e}\cdot N_p \propto N_p. \quad (9)$$

We introduce the turn-on voltage V_{to} , in accordance with conventional semiconductor diodes, as the measured bias level at which current starts to flow through the device. The inset in figure 8 shows the measured values of V_{to} as a function of N_p . The data are well fitted with a linear function $V_{\text{to}}(N_p)=V_S(N_p)+V_{\text{offset}}=e^{-1}\cdot(E_{32}+E_{21})\cdot N_p + V_{\text{offset}}$, with V_{offset} as the only fit parameter. We obtain $V_{\text{offset}}=0.33\text{ V}$. As was confirmed from measurements on a sample which contained only waveguide layers but no active or injector regions ($N_p=0$), $\sim 0.1\text{ V}$ of this residual voltage drop can be attributed to the non-alloyed contacts and graded-gap regions. The remaining voltage offset is explained by the fact that no

graded-gap regions were used to connect the first (~ 0.05 V) and last (~ 0.2 V) injector region to the adjacent bulklike InGaAs-layers of the waveguide.

Using the turn-on voltage $V_{\text{to}}(N_p)$, the differential series resistance and the threshold current density $J_{\text{th}}(N_p)$, the voltage at laser threshold $V_{\text{th}}(N_p)$ can be calculated as

$$V_{\text{th}}(N_p) = \frac{(E_{32} + E_{21})}{e} \cdot N_p + V_{\text{offset}} + \frac{\partial V}{\partial J}(N_p) \cdot J_{\text{th}}(N_p). \quad (10)$$

The last term, $\partial V/\partial J(N_p) \cdot J_{\text{th}}(N_p)$, accounts for the bias acquired above V_{to} by the current that is needed for the gain to overcome the losses (laser threshold condition). The inset in figure 8 reports the function of equation (10) and the results of the respective measurement (made at cryogenic temperature). As can be seen from the figure, the calculations are in excellent agreement with the data.

As N_p is decreased, $V_{\text{to}}(N_p)$ monotonically decreases as well. $V_{\text{th}}(N_p)$ follows this general trend; however, for very low $N_p (\leq 3)$, it increases due to the high threshold current and the series resistance.

An operating voltage approximately proportional to N_p (equation (9)) is a direct consequence of cascading. On the other hand, the slope efficiency being directly proportional to the number of stages is certainly the most useful feature, since it provides the basis for the high-power capabilities of QC lasers.

Figure 9 shows the measured slope efficiency—the increase in optical output power per unit current above laser threshold—at cryogenic temperature, for all devices of this study [30]. The inset gives the corresponding slope efficiency per stage. Pulsed and, where available, cw data are in good agreement, once corrected for the different collection efficiencies. The best fit to the data results in a slope efficiency per facet and per stage of 13.24 mW A^{-1} .

From the slope efficiency the total external differential quantum efficiency per facet is calculated as

$$\eta_D(N_p) = \frac{e}{E_{32}} \frac{\partial P}{\partial I}(N_p) \quad (11)$$

resulting in 8.5 and 8.3% per stage, for the theoretical and experimental value, respectively. Consequently, values of $\eta_D(N_p)$ larger than unity are obtained for QC structures with $N_p \geq 12$ stages, with $\eta_D(75) \approx 6.4$ per facet.

The inset in figure 10 shows the maximum peak power obtained from the lasers in pulsed operation at low temperature (10 K) and at RT. At low and intermediate values of N_p , the maximum peak power increases approximately linearly with N_p , and saturates slightly for large values of N_p , as expected.

Nevertheless, record high peak powers are still achieved with high- N_p devices. Figure 10 shows the pulsed L - I -characteristics of the device with $N_p = 75$ stages at various temperatures: peak output powers of 1.4, 1.1 and 0.54 W are obtained at 50, 200 and 300 K (RT), respectively.

We finally determined the wall-plug efficiency of our lasers. As reliable cw operation is only obtained from devices with $N_p = 3$ –30 stages, we limit our study to these lasers. At cryogenic temperatures, i.e. ≤ 30 K, we obtain maximum values of $\sim 7\%$ wall-plug efficiency for devices with $N_p = 20$ and 30 stages. For devices with a lower number of stages this value drops rapidly, resulting in $\sim 5\%$ for $N_p = 12$, and $\sim 1\%$ for $N_p = 6$ and 3 (all at heat sink temperatures ≤ 30 K).

Finally, we focus on the electrical power dissipation at laser threshold. This parameter and its minimum value are important for applications that provide limited possibilities for device cooling, such as field portable systems and trace-gas monitors.

It is a reasonable assumption that, below laser threshold, the entire electron energy is dissipated into heat via the emission of phonons, since the radiative efficiency of spontaneous

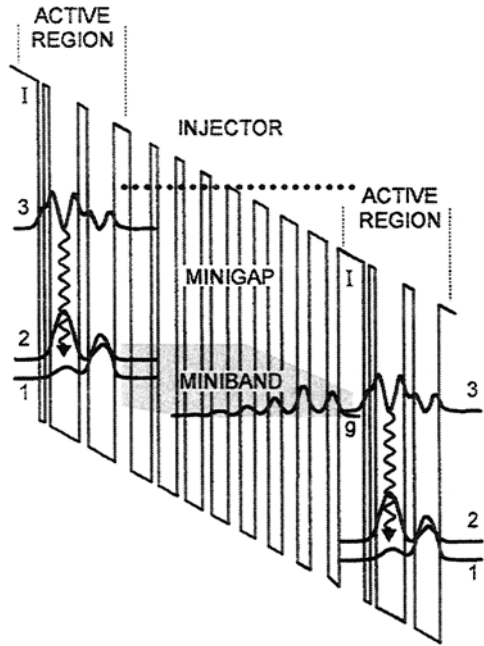


Figure 11. Conduction-band profile of two active regions with the intermediate injector under an applied electric field of 70 kV cm^{-1} of a ‘three-well vertical-active-region’ QC laser employing strain-compensated material compositions. The moduli squared of the relevant wavefunctions are labelled 1, 2, 3 and g ; ‘I’ indicates the injection barrier. The wavy arrows denote the laser transition. The shaded region in the injector represents a bandlike manifold of states. The thick dotted line shows the bottom of the second injector miniband. The actual layer thicknesses in nanometres for one period of active region and injector are from left to right, starting from the first injection barrier, **4.4/0.9/0.9/4.8/1.7/4.4/2.8/3.4/1.2/3.1/1.4/2.8/1.6/2.8/2.0/2.5/2.3/2.3/2.8/2.1/3.0/1.9**. The $\text{Al}_{0.6}\text{In}_{0.4}\text{As}$ layers (barriers) are in bold alternated with the $\text{Ga}_{0.38}\text{In}_{0.62}\text{As}$ wells. The underlined layers are doped to $n = 3 \times 10^{17} \text{ cm}^{-3}$; italic style indicates the injector region.

emission is negligible. Therefore we calculate the dissipated power density (per unit area) at threshold directly as

$$\begin{aligned} P_{\text{th}}(N_p) &= V_{\text{th}}(N_p) \cdot J_{\text{th}}(N_p) = \frac{(E_{32} + E_{21})}{e} \cdot N_p \cdot J_{\text{th}}(N_p) + V_{\text{offset}} \cdot J_{\text{th}}(N_p) \\ &\quad + \frac{\partial V}{\partial J}(N_p) \cdot J_{\text{th}}(N_p)^2. \end{aligned} \quad (12)$$

An optimum number of stages ($N_p = 22$) exists, where the dissipated power reaches a minimum $P_{\text{min}} = 6.3 \text{ kW cm}^{-2}$. This value increases by $\sim 10\%$ for shorter and longer cascade lengths of $N_p \sim 10$ and $N_p \sim 40$ stages, respectively. If the parasitic voltage V_{offset} were to be reduced, ideally to zero, the optimum number of stages would be $N_p = 18$ with a minimum power dissipation of $P_{\text{min}} = 5.7 \text{ kW cm}^{-2}$.

Three-well vertical active regions have been successful for wavelengths as long as $13 \mu\text{m}$ and have been particularly successful for shorter wavelengths. In particular, the very short length of the active region combined with the large flexibility to design injector regions makes it a prime choice design for very short-wavelength structures using strained material and strain compensation. Figure 11 shows the band-structure design of a QC laser emitting at $4.65 \mu\text{m}$ [36]. The active and injector regions are built from $\text{In}_{0.62}\text{Ga}_{0.38}\text{As}$ QWs and $\text{Al}_{0.6}\text{In}_{0.4}\text{As}$ barriers, which are all strained with respect to the InP substrate. The layer thicknesses are designed such that the compressive and tensile strains of these layers cancel each other out for each stage (and care is also taken that no single layer exceeds the critical thickness for strain relaxation). Under such conditions a cascade of $N_p \approx 30$ stages can be epitaxially grown by MBE with zero net strain. The local strain, however, inside the active regions and injectors increases the band offset—in our example of figure 11—to 720 meV, and allows very large energy separations E_{32} and concomitant short wavelengths. Figure 12 shows a transmission electron microscope image of the structure of figure 11. QC lasers with wavelengths as short as $3.5 \mu\text{m}$ have been demonstrated using this approach [37].

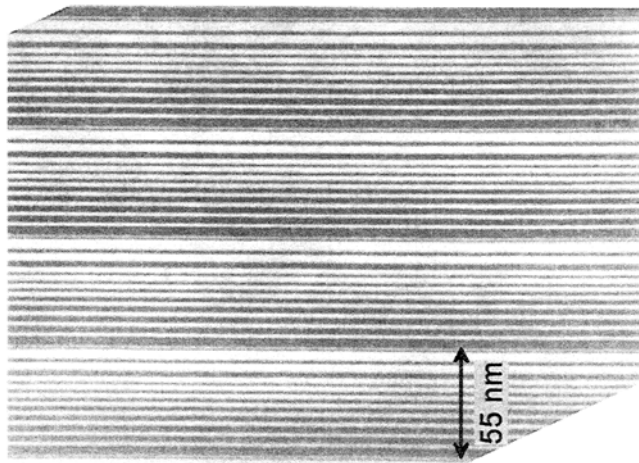


Figure 12. Transmission electron microscope image of four periods of active regions and injectors of the QC-laser structure of figure 11. Electron transport is top to bottom. InGaAs layers are shown in light grey, AlInAs layers in dark grey.

3.2. Superlattice active region

Superlattice (SL) active region QC lasers were first introduced in 1997 [6]. In short, laser action takes place between minibands, rather than between the subbands of few- and single [38] well active region QC-lasers. SL-QC lasers excel through their high gain, large current carrying capabilities, and weaker temperature sensitivity. SLs have been employed for some of the best performing QC lasers to date. However, they can generally only be applied for the longer-wavelength range (i.e. $\lambda_0 \geq 7 \mu\text{m}$, for lattice-matched InP-based SL-QC lasers) as the wider minibands take up more energy space than simple subbands.

In general, semiconductor SLs consist of a periodic stack of nanometre-thick layers of QWs and barriers. The period of this artificial crystal is typically much larger than the lattice constant of the bulk crystalline constituents. This superimposed crystal potential splits the conduction band (and the valence bands as well) along the direction normal to the layers into a series of narrow (typically, tens to a few hundreds of meV wide) minibands separated by energy gaps ('minigaps') in the strong-tunnel-coupling regime. For a given set of materials, miniband and minigap widths can be engineered by suitable choice of the layer thicknesses. In the generic case of the simple periodic SL, however, those widths are not independent of each other.

Figure 13 illustrates the original interminiband SL-QC laser concept and its first realization [6]. The SL consists of eight strongly coupled QWs, i.e. the intermediate barriers are very thin (typically 1–2 nm for conduction band discontinuities of several hundreds of meV). This results in two minibands substantially confined within the SL with 520 meV band offset. The SL is homogeneously doped to $6\text{--}7 \times 10^{16} \text{ cm}^{-3}$ in order for the extrinsic charges to screen the electric field that will be applied externally under laser operation. The ensuing quasi-Fermi level (~ 12 meV) is still located well below the top of the first miniband, which has a width ~ 100 meV, so that even at elevated temperatures the states near the top of the latter can be assumed essentially empty. Electrons are injected electrically from a preceding, equally doped, injector region directly into the ground state near the bottom of the second 'upper' miniband, as was the case with the simple three-well active region discussed in the

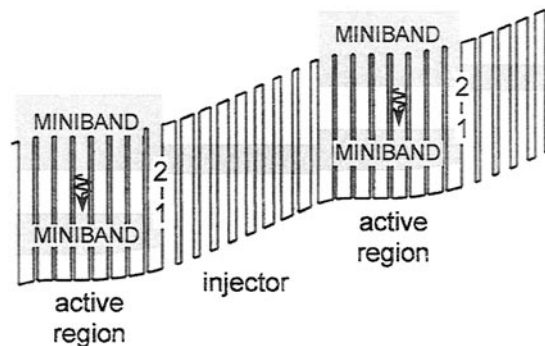


Figure 13. Schematic conduction-band structure of the original SL-QC laser. Two active region SLs with the preceding injector regions are shown. The shaded regions indicate the minibands. Laser action, as denoted by the wavy arrows, takes place across the first miniband 2–1. The applied electric field is screened from the flat SLs through extrinsic electrons.

previous sections. From there, electrons can make an optical transition to the top of the lower miniband. In k -space, this transition occurs at the so-called ‘mini-Brillouin-zone boundary’.

As in QC lasers in general, the interminiband scattering processes are dominated by LO phonon emission. Specifically, an electron thermalized near the bottom of the higher miniband can relax down to states near the top of the lower miniband by scattering via LO phonon emission employing a high momentum transfer. This process is characterized by a comparatively long scattering time of ~ 10 ps. Within each miniband, the electrons relax much faster—in a few tenths of a picosecond—by intraminiband scattering, because it involves the emission of small-wavevector optical phonons. The resulting large ratio of relaxation times of inter- versus intra-miniband scattering events ensures an intrinsic population inversion across the miniband gap. A second unique design feature of the SL-QC laser is the high oscillator strength for the optical transition at the mini-Brillouin zone boundary of the SL. The oscillator strength of radiative transitions between the first two minibands of a SL increases with wavevector and is maximum at the zone boundary [39]. In particular, it strongly increases with decreasing barrier thickness. In the original SL-QC laser structure shown in figure 13, the wavelength was selected as $8\text{ }\mu\text{m}$, using an eight-period SL with 1 nm thick AlInAs barriers and 4.3 nm thick InGaAs QWs in lattice-matched composition. The structure was optimized for maximum oscillator strength with an optical dipole matrix element of 3.6 nm , i.e. approximately twice as large as that of similar-wavelength QC lasers featuring few-well active regions.

To properly compute the energy levels and optical dipole matrix element of the laser transition, as well as the scattering times between the relevant levels, one has first to calculate the actual band profile of the structure. This requires knowledge of both the applied external bias and the electric field generated by the charge distribution of the donor ions and of the extrinsic electrons. The latter, in turn, is determined by the wavefunctions of the electronic levels. Therefore, one has to solve self-consistently Schrödinger’s equation and Poisson’s equation, which relates the charge distribution to the electrostatic potential. The rolling, steplike potential profile shown clearly in figure 13 is the result of such a calculation. The extrinsic electrons are separated from their donor ions, generating the additional undulating potential.

Once energy levels and wavefunctions are properly calculated most parameters of laser operation can just be estimated in the same fashion as before for few-well QC lasers based on intersubband transitions. For example, we re-write the gain coefficient for SL-QC lasers as

$$g = \tau_2 \left(1 - \frac{\tau_1}{\tau_{21}} \right) \frac{4\pi e z_{21}^2}{\lambda_0 \varepsilon_0 n_{\text{eff}} L_p} \frac{1}{2\gamma_{21}} \quad (13)$$

where τ_2 (~ 1 ps) and τ_1 (~ 0.1 ps) are the lifetimes of the upper ('2') and lower ('1') laser state, respectively. τ_2 is calculated from the sum of all scattering events from level 2, the bottom-most state of the upper miniband, into all states of the lower miniband, and τ_{21} is estimated as ~ 10 ps. For the structure shown in figure 13 we can then calculate a gain coefficient of 25 cm kA^{-1} [6], using the measured value of $2\gamma_{21} \sim 30 \text{ meV}$.

Used with a conventional waveguide ($\alpha_w \sim 30 \text{ cm}^{-1}$), a threshold current density of 8.5 kA cm^{-2} at 5 K heat-sink temperature, and a peak output power of 850 mW at 5 K and still 750 mW at 80 K (measured with 50% collection efficiency from one facet) were achieved, all in pulsed operation. Already these first SL-QC lasers [6] excelled through their high optical output power, which at that time was primarily a result of the much larger current carrying capabilities compared with conventional QC lasers.

In a comparison of threshold current densities, high-temperature and cw operation and slope efficiency, however, these first SL-QC lasers were inferior to QC lasers. This was mostly due to the large waveguide loss brought about by the generally high doping level, the broad luminescence linewidth ($2\gamma_{21} \sim 30 \text{ meV}$ at $8 \mu\text{m}$ wavelength) as a result of ionized impurity scattering and interface roughness scattering at the increased number of interfaces in the active region and reduced population inversion at elevated temperatures, again caused by high electron densities in the active regions. Unfortunately, such substantial extrinsic doping levels were originally needed to screen the externally applied electric field from penetration into the SLs. Therefore, subsequent efforts to improve SL-QC laser performance focused on retaining the advantages of the SL active region, while reducing the required doping levels.

The first major performance improvement came with an SL-QC laser design that places the dopants only in the injector regions [40]. The underlying idea of this design is to significantly spatially separate the extrinsic electrons from the donor ions ('modulation doping') in such a way that the field generated by these charges exactly compensates the external applied electric field across the SLs. This is illustrated in figure 14. For our best structures, we chose as active region a seven-period SL with 4.6 nm thick InGaAs QWs and 1.0 nm thick AlInAs barriers, which results in a 153 meV wide minigap ($\lambda_0 = 8.1 \mu\text{m}$). Each graded injector is n-type doped to $4.5 \times 10^{17} \text{ cm}^{-3}$ in the layers near the adjacent SL 'downhill' in the energy diagram, but the thicknesses are engineered so that the ground state of the lowest resulting miniband is concentrated near the preceding SL. Figure 14 shows the band diagram calculated self-consistently for an applied field of 29 kV cm^{-1} . As one can see, the SL regions are almost field free, with the first miniband of each period aligned in energy with the second miniband of the next period, to ensure efficient carrier transport between the stages. The energy separation between the first two states in the upper miniband at the design field has been chosen equal to the LO phonon energy ($\sim 32 \text{ meV}$). This has been found to alleviate phonon-bottleneck problems associated with reduced intraminiband scattering rates resulting from a too close level spacing [40]. The active region layer sequence is also optimized so that most of the oscillator strength is again concentrated in the 2–1 laser transition; we calculate an optical dipole matrix element of $z_{21} = 3.1 \text{ nm}$. Scattering times and a gain coefficient very similar to those of doped SL-QC lasers are obtained. Nevertheless, used with a waveguide design routinely employed in our QC lasers, which now displays a clearly lower waveguide loss α_w due to the reduced effective bulk doping of the active waveguide core, we easily obtain RT pulsed and low-temperature cw operation [40]. A RT threshold current density of 10 kA cm^{-2} and a peak optical power of 175 mW collected from one facet with 50% efficiency have been obtained for the structure depicted in figure 14.

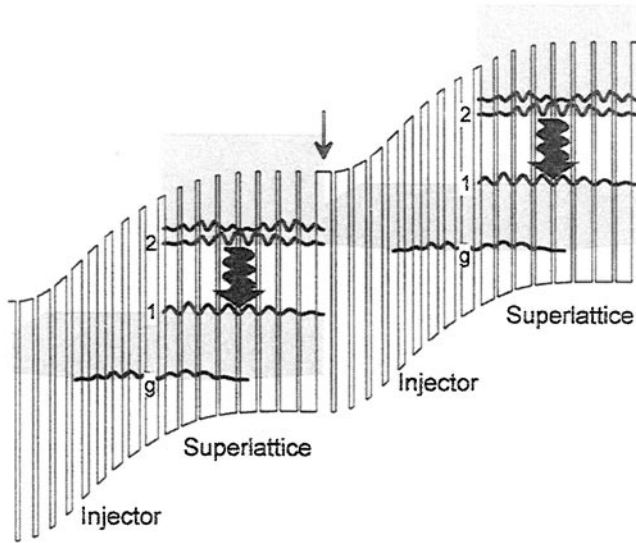


Figure 14. Calculated energy diagram of an optimized SL-QC laser with undoped SL active regions. The SLs are kept field free through modulation doping of the injector regions. The laser transition $2 \rightarrow 1$ is indicated by the wavy arrow, and by the moduli squared of the respective wavefunctions. The straight arrow indicates the injection barrier.

This design of SL-QC lasers has been optimized by further reducing the effective doping level using a structure which is only doped in a *single* QW [41]. A sheet density doping level of $4.5 \times 10^{11} \text{ cm}^{-2}$ corresponding to a 1.3 nm thick QW doped to $3.5 \times 10^{18} \text{ cm}^{-3}$ is required to still obtain a flat band profile across the adjacent SL. Such doping translates into an effective bulk doping of the active material of $5 \times 10^{16} \text{ cm}^{-3}$, which is very similar to that of few-well active region QC lasers. The performance of these lasers is described in [41], and is—as expected—very close to those of QC lasers based on intersubband transitions.

However, an even further improved design of SL-QC lasers was found in the so-called ‘chirped SL’ QC lasers. This is an alternative SL-QC laser design to achieve flat minibands with undoped active regions. It is based on SL active regions with gradually decreasing well thicknesses in the direction of electron motion (‘downhill’ in figure 15). At zero bias, the states of the QWs are localized because the variation in the thickness of adjacent layers is such that the corresponding energy levels of the isolated wells are out of resonance. As an electric field of the appropriate value, e.g. 45 kV cm^{-1} for the example of figure 15, and polarity is applied, these states are brought into resonance so that they anti-cross forming manifolds of closely spaced extended states, i.e. ‘minibands’, see figure 15. This situation is analogous to that of a compositionally graded semiconductor in which the conduction-band quasi-electric field associated with the bandgap grading is compensated by an applied electric field [42].

Initial results on this new laser were presented in [43]. The schematic band diagram of the device is shown in figure 15 for a structure with a so-called ‘funnel-type’ injector [4]. Two well defined minibands are created in the chirped SLs, matched to a single injection miniband that bridges them together across the cascading stages. The states involved in the interminiband laser transition with wavelength $7.5 \mu\text{m}$ are uniformly delocalized over at least six periods, which ensures a large optical dipole matrix element of 2.7 nm. Their scattering lifetimes, controlled by LO phonon emission, are computed to be $\tau_2 \sim 1 \text{ ps}$, $\tau_1 \sim 0.1 \text{ ps}$ and $\tau_{21} \sim 5.3 \text{ ps}$. Various samples were grown for device optimization, e.g. with varying

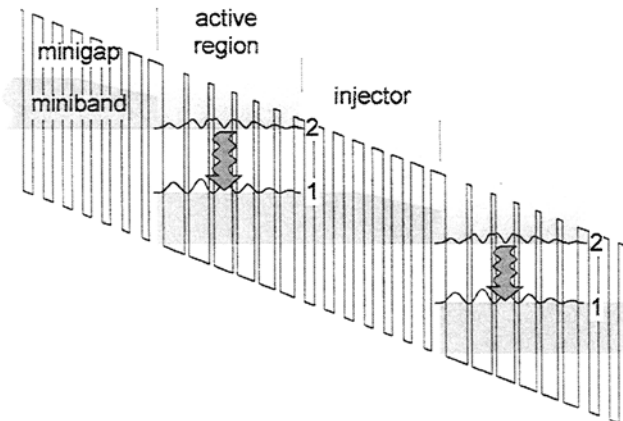


Figure 15. Calculated conduction-band profile of two so-called ‘chirped’ SL active regions and their respective preceding injector regions. The darker-shaded areas indicate the extent of the electron minibands. The laser transition between levels 2 and 1 (wavy arrow) is characterized by well delocalized electron wavefunctions, shown via their squared moduli.

doping levels, which however are all smaller than any other SL-QC lasers using non-chirped, i.e. truly periodic SLs, varying injector designs and varying but conventional waveguides. A summary is found in [43]. Optimized performance is shown in figures 16 and 17 for pulsed and cw operation, respectively. Pulsed peak powers of almost 900 mW at 5 K and nearly 300 mW at RT are obtained for devices processed with broad-area waveguide configuration. Cw performance is summarized in figure 17. Highest cw operating temperatures of 150 and 175 K were measured for substrate-side- and epilayer-side- [44] mounted devices. A maximum cw optical power of 300 mW at 5 K, and still 200 mW at 80 K was measured from one facet.

The ‘chirped’ SL active region design was subsequently used for demonstration of long-wavelength laser operation at 17 [45], 19 [46], 21.5 and 24 μm [47]. These lasers were the first demonstration of semiconductor injection lasers based on intraband transitions at wavelengths beyond the atmospheric windows (3–5 and 8–13 μm). In general, the extension to these longer wavelengths is problematic. Above the optical phonon energy, i.e. $\lambda_0 \leqslant 30 \mu\text{m}$, in fact, intersubband transitions are characterized by an increasingly smaller radiative efficiency with decreasing transition energy, owing to the enhanced phonon emission rate [48]. Furthermore, the intraband free-carrier absorption coefficient in doped semiconductors is roughly proportional to λ_0^2 , which translates into increasingly larger optical waveguide losses at longer wavelengths; finally two-phonon absorption becomes a noticeable factor. All these aspects lead to prohibitively high threshold current densities for conventional intersubband QC laser structures, which rely on resonant tunneling injection into a single electron subband. In contrast, QC lasers based on interminiband transitions in semiconductor SLs can be driven with very large current densities (up to 30 kA cm^{-2} and above) without compromising laser performance.

A schematic conduction band diagram of the SL-QC laser designed to emit at 24 μm wavelength is shown in figure 18. Laser action takes place at the edge of the minigap, 52 meV wide, between minibands 2 and 1, where well delocalized wavefunctions result in a large transition dipole matrix element of 4.8 nm. The injector miniband has been designed with a funnel shape, while the energy separation between the individual states of miniband 2 has been chosen to be of the order of the optical phonon energy (~ 32 meV) to facilitate fast

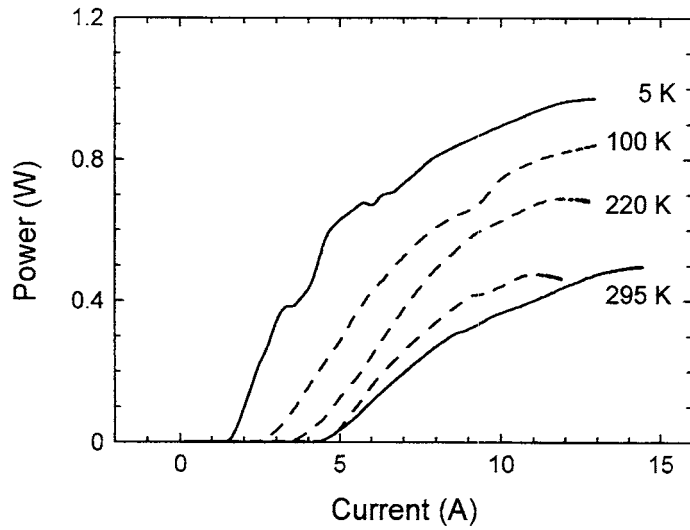


Figure 16. Pulsed light output versus current characteristic of an optimized ‘chirped’ SL-QC laser as shown in figure 15. Results of two devices (solid and dashed curves) are depicted at various heat sink temperatures. The lasers were processed as conventional deep-etched ridge waveguide lasers. Pulsed operating conditions comprise typically 50 ns long pulses at a repetition rate between 5 and 100 kHz, i.e. low duty cycle.

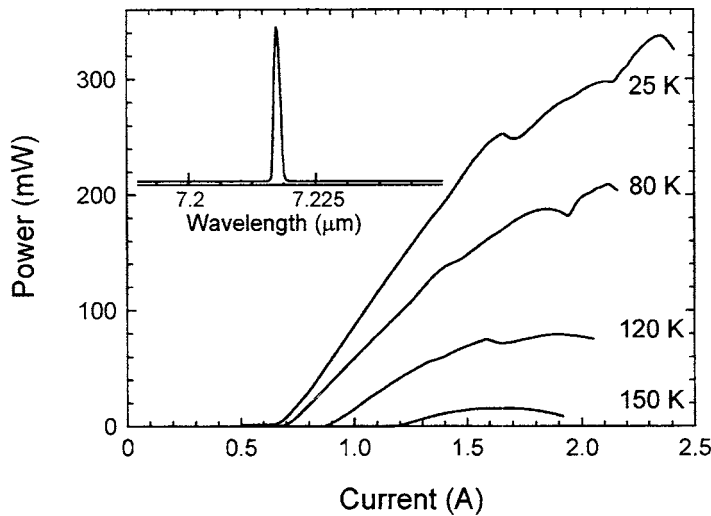


Figure 17. Cw light output versus current characteristics at various heat-sink temperatures of an optimized ‘chirped’ SL-QC laser as shown in figure 15. The device was a conventionally processed ridge waveguide structure mounted substrate side to the heat sink. A maximum operating temperature of 150 K is achieved. Inset, single-mode spectrum of a chirped SL-QC laser operated in cw mode.

intraminiband relaxation. We compute for the lowest state of miniband 2 a scattering lifetime into the topmost state of miniband 1 of $\tau_{21} = 2.4$ ps at cryogenic temperatures and a relaxation time of the uppermost state of miniband 1 of $\tau_1 = 0.7$ ps. The latter value is more difficult

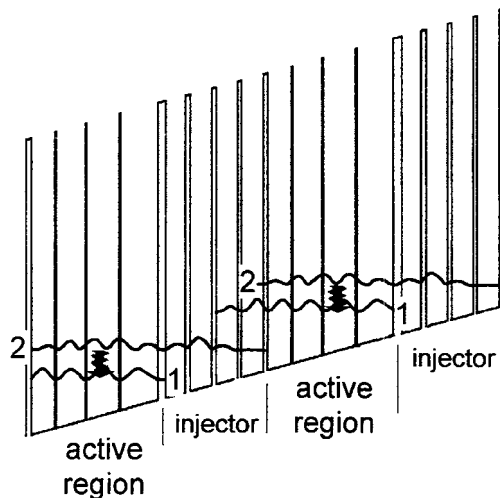


Figure 18. Calculated conduction-band profile of two ‘chirped’ SL active regions and their respective preceding injector regions. The laser is designed for operation at $24\text{ }\mu\text{m}$ wavelength. The shaded areas indicate the extent of the electron minibands. The laser transition occurs between levels 2 and 1 (wavy arrow), which are separated by $\sim 52\text{ meV}$.

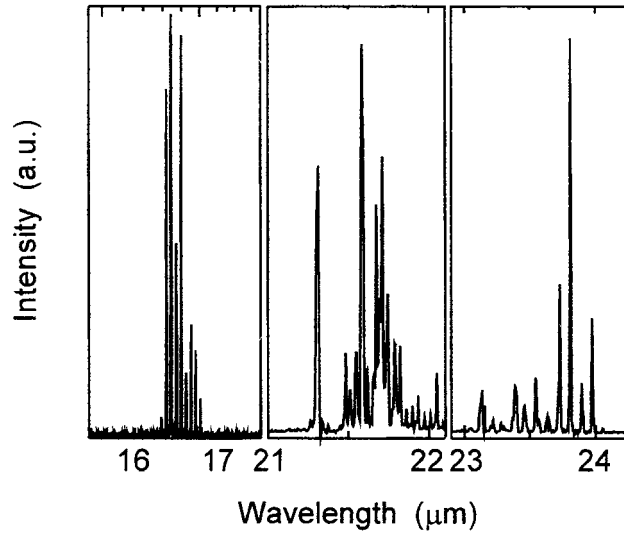


Figure 19. Fabry–Perot type emission spectra of various long-wavelength SL-QC lasers using the chirped SL active region design. The spectra are taken at cryogenic heat-sink temperatures and under pulsed operation of the lasers.

to derive accurately due to the almost continuous energy distribution of the states in the lower miniband 1. We finally calculate expected threshold current densities around 1 kA cm^{-2} .

The long-wavelength QC lasers were customarily processed with surface plasmon waveguides, which are discussed in more detail in the following section 4.3. Figure 19 shows pulsed spectra obtained of the lasers at low temperatures. The laser structure at $19\text{ }\mu\text{m}$ was optimized by choice of the injector region doping level to also operate in cw mode, as is shown in figure 20. Figure 21 finally shows a light output (L) and voltage (V) versus current (I) characteristic of the longest-wavelength SL-QC laser to date, at $24\text{ }\mu\text{m}$. Threshold current densities, pulsed peak power levels and highest pulsed operating temperatures of $\sim 5\text{ kA cm}^{-2}$, $\sim 5\text{ mW}$ and $\sim 130\text{ K}$, respectively, are obtained.

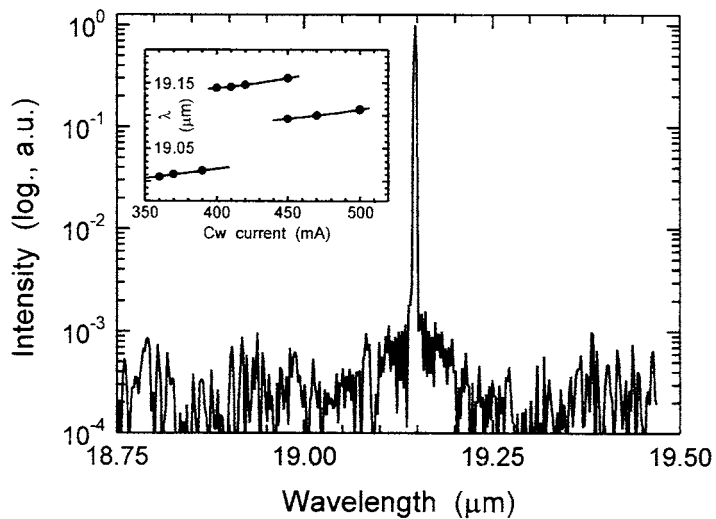


Figure 20. Single-mode emission spectrum (in logarithmic scale) of a chirped SL-QC laser designed to emit around $19\ \mu\text{m}$. The heat-sink temperature is $10\ \text{K}$. A side-mode suppression ratio of $30\ \text{dB}$ is achieved (which coincides with the noise floor of the measurement set-up). Inset, peak wavelength (circles) as a function of cw current. Piece-wise continuous linear tuning is observed (solid curves). Regions of continuous tuning are interrupted by jumps between different modes.

A recent extension to chirped SL-QC lasers, termed ‘bound-to-continuum’ transition active region design by Faist *et al* [49], has shown very good performance in high-temperature, high-duty-cycle and high-optical-power operation.

3.3. Diagonal transition active region

The QC and SL-QC laser designs described in the previous two sections had in common that the wavefunctions directly involved in laser action, of the upper and lower laser state, respectively, are essentially located in the same region of real space, hence the title ‘vertical’ (in the energy versus growth direction diagram) transition. The two wavefunctions being collocated has several distinctive consequences. First, from an energy level point of view, the energy separation of the two states is largely independent of the applied electric field in a fairly wide range around the design field. This gives lasers based on such a vertical design a clear robustness in terms of wavelength versus applied voltage and, as a consequence, also versus temperature. (Typically, as the heat-sink temperature is raised the laser threshold voltage first drops and later rises, the former being due to thermally induced changes in the band offset and the latter to an increased threshold current density and a small though non-negligible differential resistance.) On the other hand, and relating to the calculation of the gain coefficient, the collocation of the wavefunctions leads to a comparatively large optical dipole matrix element, but also comparatively short electron scattering times. Both are a result of the large overlap of the wavefunctions of upper and lower laser states.

In this section, we discuss the so-called ‘diagonal’ transitions, using as an example a structure in which the upper and lower state wavefunctions are clearly located in spatially different regions. In contrast to ‘vertical’ transitions, QC lasers based on such active regions

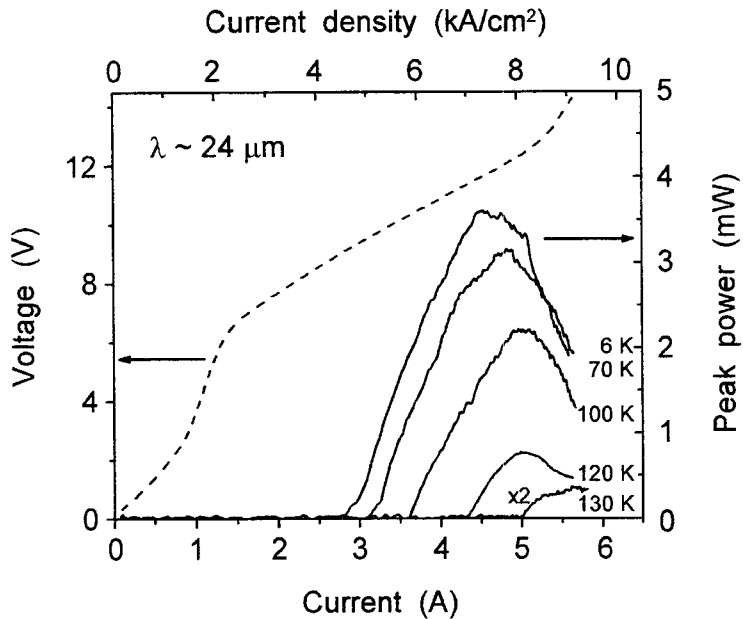


Figure 21. Pulsed light output (solid curves) and voltage (dashed curve) versus current characteristics at various heat-sink temperatures, indicated, of an SL-QC laser designed for long-wavelength ($\lambda \sim 24 \mu\text{m}$) operation.

show a strong dependence of the wavelength on the applied electric field through a voltage-induced Stark effect. The design parameters are furthermore characterized through a smaller dipole matrix element but also clearly longer scattering times, thus allowing again for sufficient gain to achieve laser action.

In the design shown in figure 22, under an appropriate applied positive bias, laser action takes place from level G_+ to level **1**, via a photon-assisted tunneling or diagonal transition (wavy arrow) since the two states have reduced spatial overlap [50]. (In section 5.2 it will become clear why we term the upper laser state here ' G_+ ' rather than '2' [51] as in the previous sections.) Level **1** is the ground state of the active region QW, while G_+ is the ground state of the miniband in the superlattice injector. This miniband is designed so that under application of a suitable electric field, G_+ is spatially localized close to the injection barrier. The emitted photon energy is controlled, for a given active region QW, by the thickness of the injector layers in the immediate vicinity of the injection barrier and by the applied electric field.

An in-depth description of QC lasers based on photon-assisted tunneling, including the implications of the reduced spatial overlap of the electron wavefunctions involved in laser action, can be found in [50]. Here, we focus only on the calculation of the threshold gain, an important component of which is $k_+ = z_+^2 \cdot E_+ \cdot \tau_+$. The product of the first two factors, that is, the square of the optical matrix element z_+ and the energy of the transition E_+ , is proportional to the oscillator strength f_+ . τ_+ is the lifetime of level G_+ , determined mainly by the relaxation time from G_+ to **1**, due to the emission of an LO phonon. For the laser design shown in figure 22 under an electric field of $+90 \text{ kV cm}^{-1}$ corresponding to laser threshold, we calculate $z_+ = 0.35 \text{ nm}$, $\tau_+ = 46 \text{ ps}$ and $E_+ = 198 \text{ meV}$ ($\lambda_{0+} = 6.3 \mu\text{m}$), respectively. This results in $k_+ = 1.12 \text{ nm}^2 \text{ ps eV}$. The population inversion necessary for laser action is guaranteed by the long lifetimes τ_+ between the upper and lower laser levels, due to the relatively large spatial

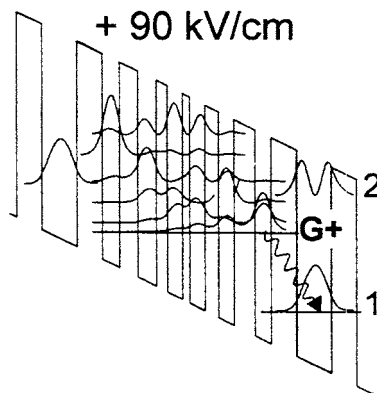


Figure 22. Conduction band diagram of two active regions with the intermediate injector region of a diagonal transition active region QC laser under a positive applied electric field of 90 kV cm^{-1} , approximately corresponding to laser threshold. The actual layer thicknesses in nanometres are from left to right starting from the first injection barrier: **3.5/4.8/3.5/2.4/2.5/2.6/1.5/2.2/1.0/2.2/1.9/2.2/2.9/2.2/3.5/4.8/3.5**. The $\text{Al}_{0.48}\text{In}_{0.52}\text{As}$ layers (energy barriers) are in bold symbols alternated with the $\text{Ga}_{0.47}\text{In}_{0.53}\text{As}$ wells. The underlined layers are doped to $n = 4 \times 10^{17} \text{ cm}^{-3}$; italic style indicates the injector region. The moduli squared of the wavefunctions in the active and injector regions are shown. The wavy arrow indicates the laser transition $G_+ \rightarrow 1$.

separation of the states (G_+ and **1**) of the diagonal laser transition. In comparison, the time for electrons to tunnel resonantly from level **1** into a state of the injector region is calculated as 0.5 ps; the lifetime of G_+ due to the combined LO-phonon scattering rates into all states of the following, down-stream injector region is ~ 380 ps. The large ratio of the scattering time from G_+ to level 1 to the tunneling time out of level 1, make it unnecessary to add the usual ‘phonon-doublet’ familiar from conventional QC-lasers.

The gain coefficient, defined as the quantity that multiplied by the current density J gives the peak material gain ($G_+ = g_+ J$), is given by $g_+ = (2e)/(\epsilon_0 \hbar c L_p n_{\text{eff}} (2\gamma)) \cdot k_+$ under the somewhat simplified assumption that the entire current passes through levels G_+ and **1**. $L_p = 35.4 \text{ nm}$ is the length of one stage (one active region plus injector), e the unit charge, ϵ_0 the vacuum dielectric constant, \hbar the reduced Planck constant, c the vacuum speed of light, $n_{\text{eff}} = 3.26$ the effective refractive index of the waveguide and $2\gamma \approx 35 \text{ meV}$ the luminescence linewidth. The latter has been measured from sub-threshold emission spectra. Inserting the above values into the equation for the gain coefficient results in $g_+ \approx 32 \text{ cm kA}^{-1}$. This value is of the same order of magnitude as previously optimized vertical-transition QC and SL-QC lasers.

All of the laser samples contain a cascade of 36 active regions alternated with electron injectors. This stack is embedded in a dielectric waveguide very similar to those previously used with QC lasers. We estimate a waveguide loss of $\alpha_w \approx 20 \text{ cm}^{-1}$. The lasers are processed as deep-etched ridge waveguide lasers with stripe widths ranging from 10 to $20 \mu\text{m}$. They are cleaved into bars with a length of $\sim 3 \text{ mm}$ and the facets are left uncoated, which results in an outcoupling (mirror) loss of $\alpha_m \approx 4.2 \text{ cm}^{-1}$.

The device characteristics of a representative diagonal-transition active region QC-laser are displayed in figure 23. Part (a) shows the emission wavelength as a function of the heat-sink temperature. The low-temperature wavelength is $\lambda_{0+} \approx 6.33 \mu\text{m}$ and it clearly blue-shifts with increasing temperature. This trend is contrary to that of vertical-transition active region QC lasers, which typically show a red-shift with temperature. This discrepancy is a direct consequence of the increased voltage accompanying the larger threshold current at elevated temperatures. In figure 23(b) the voltage (V) versus drive current (I) characteristics are shown at 20 K, and the light output power (L) versus I characteristics at several heat-sink temperatures. The $L-I-V$ curves display a low-temperature threshold current density of $J_{\text{th}} \approx 3.5 \text{ kA cm}^{-2}$. This result should be compared with the calculated threshold of $J_{\text{th}} = (g_{\pm} \cdot \Gamma) / (\alpha_m + \alpha_w) \approx 1.7 \text{ kA cm}^{-2}$, using the values of g_{\pm} , α_w , and α_m given above, and Γ , the mode confinement factor, being 0.45. We believe the difference between the measured and calculated values of J_{th} to be due to decreased injection efficiency into the levels of the laser transition. In fact, electrons can tunnel from the injector region into the first excited

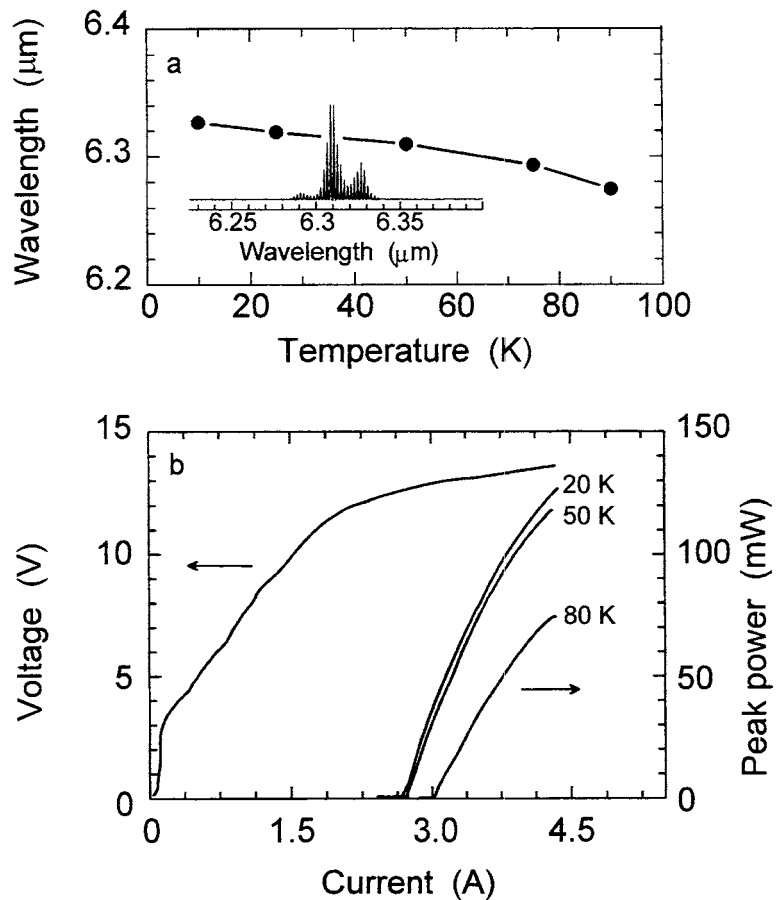


Figure 23. (a) Peak wavelength (circles) as a function of heat sink temperature of the QC-laser described in figure 22. Inset, Fabry-Perot spectrum as obtained in pulsed operating conditions. (b) Pulsed light output and voltage versus current characteristics at various heat sink temperatures as indicated of a QC-laser with diagonal transition design of the active region.

state of the active region QW. From there electrons either tunnel into the continuum region of the conduction band or scatter into the active region ground state. Both paths are deleterious for laser action, as they reduce the lifetime τ_+ of state G_+ , and in the latter case also temporarily add an electron to the lower laser level. This, in turn, leads to a reduced gain and a weaker inversion than previously estimated [51]. However, the lasers still display an optical peak output power of > 100 mW and a slope efficiency of > 120 mW A $^{-1}$.

Similar, optimized, lasers have been operated up to RT and have been exploited for large wavelength tunability [50]. Nevertheless, we chose to discuss this somewhat lower-performing structure here as we shall see that this particular design can be used to fabricate QC lasers that operate under both bias polarities and with nearly independent attributes, such as two different wavelengths [51] depending on bias polarity.

4. Mid-infrared waveguides and resonators

In the previous sections we focused on the various designs of active regions and injectors presently in use with QC lasers. Thereby we calculated the gain coefficients and discussed how a large gain coefficient can be achieved by band-structure engineering. A second important contribution to the laser threshold, the slope efficiency and the peak power are the total losses. This has briefly been discussed in section 2.1. As it was shown there, a low waveguide loss is crucial for high-quality QC-laser performance. Taking into account the bigger impact of free carrier absorption in the doped semiconductor and in the metallization for the mid-infrared wavelength range, it is obvious that the question of waveguide design is more complex here than it is at near-infrared wavelengths, where the obvious choice are semiconductor dielectric waveguides. In the following we shall discuss several advantageous QC-laser waveguide designs.

4.1. Fabry–Perot type quantum cascade lasers with dielectric waveguides

The dielectric waveguide is a straightforward choice if the material system in use provides the appropriate and sufficiently large refractive index variations to build a high-refractive-index waveguide core, which contains the active material, and lower-refractive-index cladding layers. The confinement factor, i.e. the overlap of the optical guided mode with the active regions and injectors (see the comment in section 2.1), should be as large as possible to obtain a low laser threshold. This can be achieved with an as large as possible refractive index step between the core and cladding layers.

In the material system most commonly used with QC lasers at present, the InP substrate with a refractive index $n_{\text{InP}} \sim 3.10$ and AlInAs with a refractive index $n_{\text{AlInAs}} \sim 3.20$ are natural cladding layers for the waveguide core. The latter consists of the stack of 500 or more alternated ultra-thin layers of InGaAs and AlInAs. The refractive index of this stack is usually modelled through a linear interpolation between the refractive indices of AlInAs and InGaAs ($n_{\text{InGaAs}} \sim 3.49$) according to the volume fraction of the two constituents. It is therefore clearly higher, often around $n_{\text{QC-stack}} \sim 3.35$, than the refractive indices of the cladding layers. In order to increase the average refractive index of the waveguide core even more, in particular when the actual cascade stack is chosen rather thin, i.e. with a small number of stages, the active region and injector stack is sandwiched between two several hundred nanometres thick InGaAs layers. The resulting waveguides typically contain $N_p \sim 30$ stages of active regions and injectors, and have operating voltages ≤ 10 V (see equation (10)), and confinement factors of $\Gamma \sim 0.5$.

So far, we have only given the refractive indices of the materials without taking into account their doping levels. However, being current injection lasers, all or at least a significant portion of the waveguide layers have to be doped for carrier transport. Free-carrier absorption in these layers, and at high doping levels the strongly noticeable onset of the plasma edge, usually reduce the refractive index by a few per cent over the purely dielectric value. In addition a noticeable attenuation coefficient is introduced, which is ultimately responsible for the waveguide loss α_w .

In addition to the free-carrier loss from the doped semiconductor layers, the coupling of the mid-infrared wavelength light to the surface plasmon at the semiconductor–metal interface—with the metal being the top contact—can introduce a large additional waveguide loss. Sirtori *et al* [52] early on designed a waveguide which alleviates this unwanted coupling to the surface plasmon. In general, making the dielectric layers thick enough to separate the top metal from the waveguide core would alleviate the problem as well, but this approach conflicts with

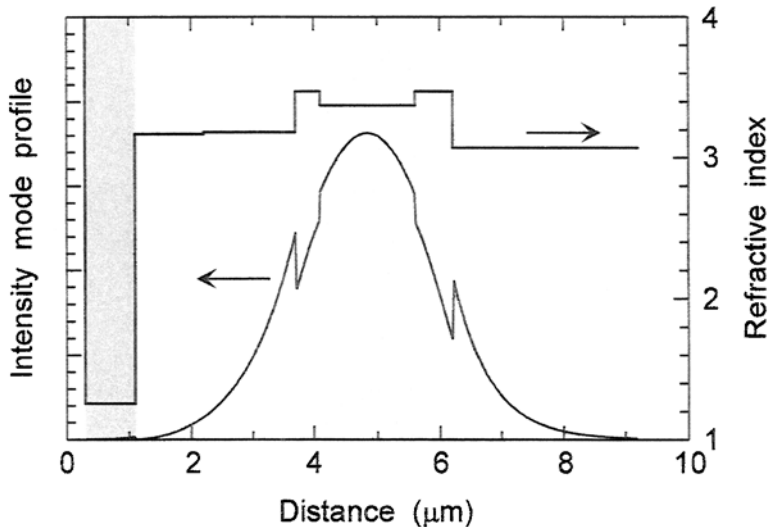


Figure 24. Intensity mode profile and profile of the real part of the refractive index in the (reverse) growth direction of an optimized dielectric QC-laser waveguide incorporating so-called plasmon-enhanced confinement (dark-shaded area), employing a highly doped, very low-refractive-index semiconductor layer. The stack of active regions and injectors is indicated by the lightly shaded area. This waveguide is optimized for $8.5\text{ }\mu\text{m}$ wavelength.

the desirable requirement of thin epilayers for reduced growth time in MBE. The solution by Sirtori *et al* [52] has been termed a ‘plasmon-enhanced’ waveguide, as it uses the bulk plasmon resonance in a highly doped semiconductor layer.

Figure 24 shows a cross section of an optimized plasmon-enhanced waveguide for $\lambda = 8.5\text{ }\mu\text{m}$ wavelength. The low-doped ($\sim 2 \times 10^{17}\text{ cm}^{-3}$) InP substrate is the lower waveguide cladding layer. Note that the fact that the InP substrate can be used as a cladding layer helps to reduce MBE growth thickness considerably. The top AlInAs cladding region consists of a thick low-doped ($\sim 1-3 \times 10^{17}\text{ cm}^{-3}$) layer to reduce waveguide losses and provide low-loss optical confinement. The following topmost highly doped InGaAs layer plays a crucial role in suppressing the coupling between the fundamental waveguide mode and the surface plasmon mode propagating along the metal contact–semiconductor interface. The doping level in this layer is high enough, here $7 \times 10^{18}\text{ cm}^{-3}$, that the plasma frequency (equivalent to $9.1\text{ }\mu\text{m}$ wavelength) approaches but does not exceed that of the waveguide mode at $8.5\text{ }\mu\text{m}$. At such a high doping level we can take advantage of the anomalous dielectric dispersion near the plasma frequency. The resulting strong decrease of the refractive index—from $n_{\text{InGaAs}} \sim 3.49$ to 1.26—enhances the confinement factor of the mode. Figure 24 illustrates the calculated refractive index and mode profile. Note the large drop in the refractive index in going from the AlInAs cladding, $n_{\text{AlInAs}} \sim 3.20$, into the ‘plasmon-enhanced’ waveguide layer, which strongly suppresses the mode penetration in the latter region, thus also reducing the waveguide losses, and suppressing the coupling to the surface plasmon. The confinement factor is calculated as 0.51, the effective refractive index of the mode is $n_{\text{eff}} \sim 3.27$ and the calculated waveguide loss $\alpha_w \sim 8.7\text{ cm}^{-1}$. Calculations show that if the plasmon-enhanced confinement layer were eliminated the loss would be significantly increased ($\alpha_w \sim 15.1\text{ cm}^{-1}$) and the confinement factor would be reduced to 0.44.

In general, the actual choice of the material, InGaAs or AlInAs, of this highly doped topmost waveguide cladding layer is not important, as the refractive index can be reduced

by choice of the doping level alone. Nevertheless, a combined study of the reduction of the refractive index and the increase of the attenuation coefficient with doping level suggests using InGaAs for wavelengths longer than $\sim 5 \mu\text{m}$, while using AlInAs for shorter wavelengths.

Whereas AlInAs provides a natural cladding material, if InP is available for growth by MBE, then this is a favourable approach due to its generally lower refractive index and better thermal conductivity. A plasmon-enhanced design of the waveguide is also indicated in this case.

QC lasers have not only been fabricated in the InGaAs/AlInAs on InP material system but also in the GaAs/AlGaAs system. There, the substrate, GaAs, has the highest refractive index, and does not, therefore, provide a natural cladding layer. Furthermore, in order to achieve a strong index contrast between the GaAs/AlGaAs multilayer core and AlGaAs cladding layers, a high-AlAs-mole-fraction material would have to be used for the latter. This is, however, generally ill advised as it difficult to dope this material at a sufficiently high level for efficient current transport [9]. Sirtori *et al* [53] and other groups working on GaAs-based QC lasers therefore employ with great success ‘plasmon-enhanced’ dielectric waveguides with highly doped GaAs for both claddings.

So far, we have discussed the layer structure in the growth direction. The waveguide in this direction, as shown in figure 24, is usually single mode, i.e. no higher-order transverse mode exists, or—if it does, as is sometimes possible for short wavelengths—it has such high losses and low confinement factor that it will not be excited during laser operation. Next, we shall discuss waveguiding in the in-plane direction.

Conventional semiconductor lasers are often processed as entirely planar structures, where waveguiding is provided only by current flow from a top stripe contact into the large-area bottom contact. Such ‘gain-guiding’ works in principle also for QC-lasers. However, a very large in-plane current spreading—aided by a high turn-on bias and large differential resistance (\sim few 10Ω to few $10 \text{ k}\Omega$ depending on wavelength) below turn-on—makes this a very inefficient waveguide. The preferred QC-laser waveguides are therefore etched to various depths for efficient current and light confinement. The resulting stripe widths can range from a few to several $10 \mu\text{m}$, depending on the application. Stated qualitatively, the wider the stripe the larger the output power; however, larger stripes often allow excitation of higher-order transverse modes.

For best performance, QC lasers are processed into narrow, deep-etched ridges for strong current confinement and efficient heat removal as a result of the larger surface-to-volume ratio. Conventionally, the narrow ridges are passivated by thin (few 100 nm thick) layers of SiN, SiO or ZnSe [54], and then overlaid with contact metallization. The latter inherently increases the waveguide loss due to the interaction of the mode with the metal layers. Several improvements in the lateral QC-laser waveguide design have previously been published, such as a buried-heterostructure waveguide [55], or lateral wet oxidation [56]. Both approaches show clear improvements in laser performance, but suffer form the fact that they do not provide a strong lateral optical confinement for the guided mode.

Another approach for an improved QC-laser lateral waveguide has recently been published, using $\text{Ge}_{0.25}\text{Se}_{0.75}$ chalcogenide glass as a thick side-wall coating and, in fact, burying layer for narrow laser ridges [57]. We measure a decrease in waveguide loss up to $\sim 50\%$ (for a $7 \mu\text{m}$ wide ridge waveguide laser emitting at $8 \mu\text{m}$ wavelength), and a concomitant decrease in threshold current density and improvement in thermal and optical power performance.

Chalcogenide glasses are well known low-loss mid-IR materials [58], which exist in a variety of chemical compositions with respectively varying optical constants. The refractive indices vary around 2.3, thus are considerably below that of the semiconductor material and allow strong optical confinement. As such they can be used to tailor the effective refractive

index of the waveguide ridge. They can also be deposited in very thick layers without accumulative strain, which helps to reduce parasitic capacitance and improves the high-speed performance of the lasers [59]. They are furthermore electrostatically robust, which is important in light of the sometimes high operating voltage of QC lasers. Finally, we have confirmed that the fabrication methods for chalcogenide glasses are fully compatible with conventional QC-laser fabrication technology.

For our experimental demonstration of the improved waveguide structure we chose the ‘three-well vertical’ design of the active region of section 3.1. The wafers were processed by wet-chemical etching into deep-etched narrow ridges with a width ranging from 5 to 10 μm , measured at the centre of the waveguide core. The lasers were then finished either using conventional side-wall passivation (300 nm of SiN) overlaid with top-contact metallization (10 nm Ti followed by 400 nm Au), or burying the ridges with chalcogenide glass.

In the latter case, a thick layer of $\text{Ge}_{0.25}\text{Se}_{0.75}$ was deposited by pulsed laser ablation. The deposited layer was typically thicker than the height of the laser ridges, i.e. $\sim 6\text{--}8 \mu\text{m}$ thick. Following deposition, a window was etched into the $\text{Ge}_{0.25}\text{Se}_{0.75}$ layer using optical lithography for masking and freon plasma for removal of the chalcogenide from the top of the laser ridges. Conventional top-contact metallization was then applied. The insets in figure 25 show cross-sections of both waveguides.

Figure 25 shows the net gain as a function of current density for two comparable, 10 μm wide and 2.32 mm long devices, one processed with a chalcogenide lateral waveguide, one with a conventional waveguide. The data have been extracted from sub-threshold cw emission spectra following the method of Hakki *et al* [35]. After fitting the data with linear functions, the waveguide loss can be read directly from the intersections of those linear functions with the vertical axis. We obtain a waveguide loss of 20.6 and 26.4 cm^{-1} for the GeSe and conventional waveguide, respectively: a clear improvement for the former. As a consequence, the threshold current density of the chalcogenide-clad laser was also reduced from 1.64 to 1.25 kA cm^{-2} , measured at a heat-sink temperature of 10 K.

Figure 25 also shows results of the device for which we have measured the lowest waveguide loss. The laser was a 7 μm wide and 2.7 mm long device. Hakki–Paoli measurements resulted in a waveguide loss of 13.5 cm^{-1} , much smaller than the $\sim 24 \text{ cm}^{-1}$ obtained for 14 μm wide conventionally processed (metallized) stripes.

In both pulsed and cw operation threshold current densities are lower, by $\sim 10\%$, for the laser with the $\text{Ge}_{0.25}\text{Se}_{0.75}$ waveguide compared with the wider, metallized waveguide laser, despite the smaller confinement factor and increased sensitivity to ridge width fluctuation of the former. If—as in [30]—the dependence of the pulsed threshold current density J_{th} on the heat-sink temperature T is fitted with a function $J_{\text{th}} = J_0 \cdot \exp(T/T_0) + J_1$, with J_0 , T_0 and J_1 as fit parameters (equation (4b)), a characteristic temperature $T_0 = 102 \text{ K}$ is obtained, a clear improvement over $T_0 = 84 \text{ K}$ of the conventional waveguide [30]. This improvement in temperature performance also resulted in cw operation up to 170 K heat-sink temperature (mounted substrate-side). The highest cw operating temperatures of the conventionally processed lasers were 130 and 150 K for substrate- and epilayer-side-mounted devices, respectively.

4.2. Distributed feedback quantum cascade lasers

Most trace gases of importance, from byproducts of fossil fuel burning to constituents of human breath, have telltale absorption features in the mid-infrared wavelength range—their ‘fingerprint’ region of the spectrum—as a result of molecular rotational–vibrational transitions. Narrow-linewidth, tunable semiconductor lasers in this wavelength range are used to spectrally

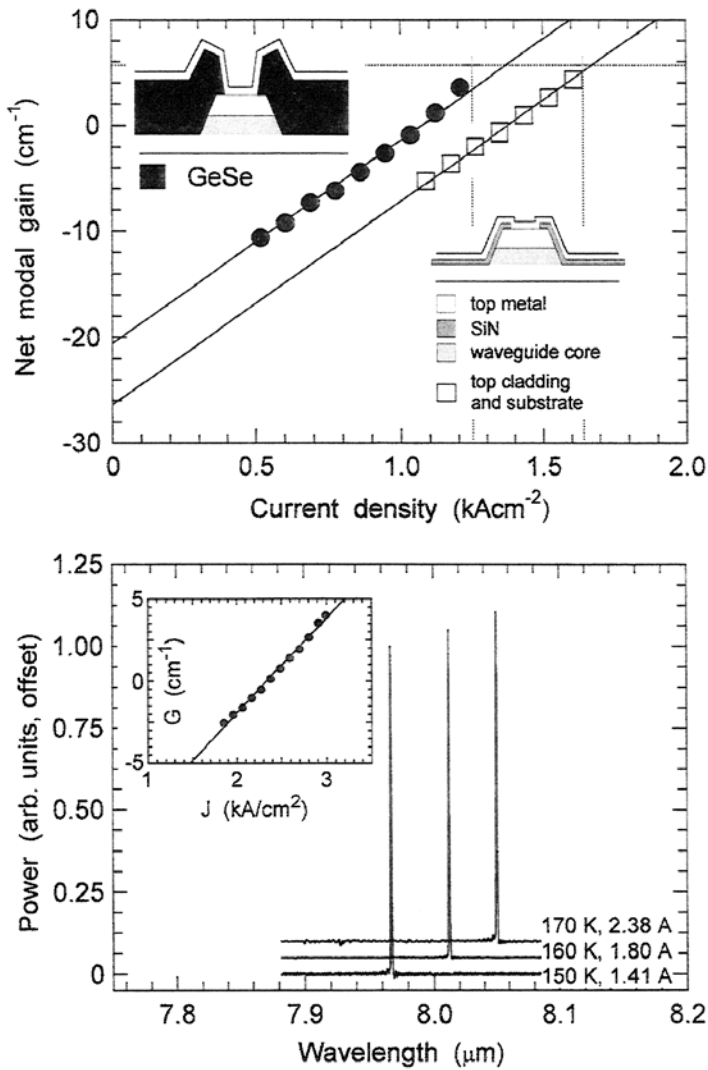


Figure 25. Top, net modal gain as a function of the current density of two $10\text{ }\mu\text{m}$ wide and 2.32 mm long QC-lasers, solid circles representing a device with GeSe lateral cladding (the upper inset shows a schematic cross section), open squares representing a device with conventional metallic lateral claddings (lower inset). The data have been processed following the technique of Hakki and Paoli. The dashed lines indicate the respective laser threshold current densities. Bottom, cw emission spectra of a $7\text{ }\mu\text{m}$ wide and 2.7 mm long QC-laser with GeSe lateral waveguide at various heat sink temperatures and current levels. The inset shows the net modal gain G as a function of the current density J measured at 10 K . A waveguide loss of 13.5 cm^{-1} is deduced from these data.

map out and qualitatively and quantitatively detect these trace gases, by a measurement technique called ‘tunable infrared laser diode absorption spectroscopy’. Its advantage is the high sensitivity and specificity, usually combined with the advantages of the solid state device approach, i.e. the compactness and robustness of a packaged semiconductor laser device.

In order to provide the required narrow-band emission, however, a simple Fabry–Perot type resonator as described above is not sufficient. The typically $1\text{--}3\text{ mm}$ long cavity leads

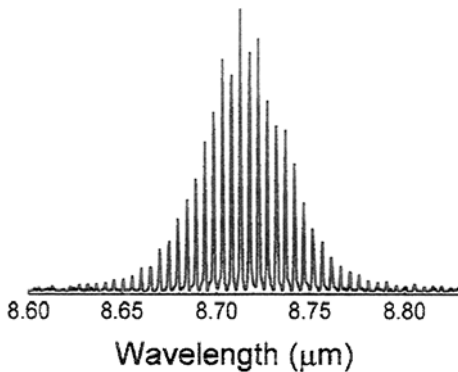


Figure 26. Characteristic Fabry-Perot type emission spectrum of a QC laser operated in pulsed mode.

to a spacing of the Fabry-Perot modes which is narrow ($\sim 0.7 \text{ cm}^{-1}$ for a 2.25 mm long laser) compared with the width of the gain spectrum ($> 50 \text{ cm}^{-1}$). This is the cause for the lasers operating in multiple modes under ordinary conditions, certainly in pulsed but also in cw at high current levels. A Fabry-Perot type emission spectrum as shown in figure 26—while acceptable for some spectroscopy applications targeting liquids and solids, where the characteristic absorption features are broad continuous bands—is not useful for demanding gas sensing applications. Rather a single-mode output with good side-mode suppression ratio (SMSR) which can be controlled and tuned over a certain wavelength range is needed. With that aim, QC lasers are fabricated as DFB lasers incorporating a first-order Bragg grating.

DFB lasers provide a very elegant and reliable method to achieve the required single-mode operation. Repeated scattering from a Bragg grating, which is incorporated into the waveguide, favours one wavelength (the Bragg wavelength) and it is the grating period rather than the laser gain spectrum which determines the single-mode emission wavelength. QC-DFB lasers were first demonstrated in 1996 [5, 60]. Very rapidly they have evolved and have already shown great promise in many different gas sensing applications (see section 7).

As described in section 4.1, the top cladding of the conventional QC-laser waveguide is usually composed from several layers, low-doped inner ones capped by a highly doped layer. This characteristic QC-laser waveguide [52] provides several possibilities to produce a grating modulation strong enough to supply the necessary wavelength selective feedback. In the first type the grating is etched into the surface of the waveguide; figure 27 shows a partial photograph of such a device. If the highly doped topmost waveguide layer is made thin or entirely removed and then directly overlaid with metal in a grating pattern as shown e.g. in figure 27 three phenomena appear. First, the waveguide loss in the position of the grating grooves is higher than in the position of the grating ridges (the non-etched portion of the grating), leading to a loss modulation of the waveguide. Secondly, the metal layer in the grating grooves—now closer to the low-doped section of the waveguide—pulls the mode towards itself, giving it some characteristics of a surface plasmon. As the mode is pulled into the top-cladding layer, its effective refractive index (roughly defined as the average refractive index of the various waveguide layers, weighted by their overlap with the optical mode) is modulated. Thirdly, this displacement of the mode also results in a modulation of the overlap of the guided mode with the active material, inducing a modulation of the modal gain, which has the same character as a loss modulation and usually is designed to increase the effect of the latter. Depending on the actual etch depth compared with the thickness of the cladding layers, one component of waveguide modulation may win over the others (the modulation of the gain via the confinement factor is usually the weakest component). All

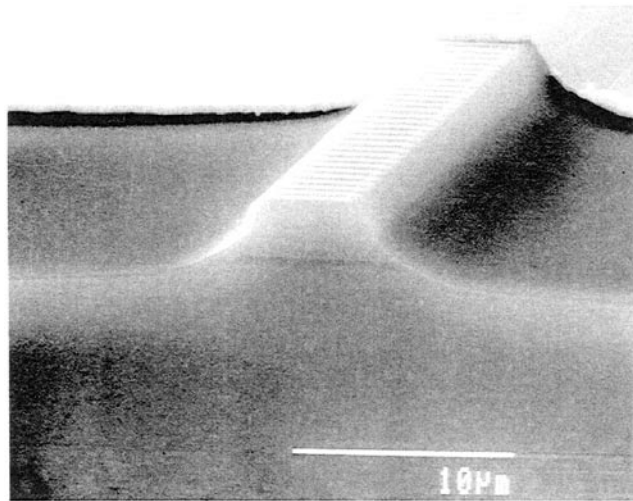


Figure 27. Scanning electron microscope image of a portion of a QC-DFB laser featuring a top grating. The cleaved mirror section of the deep-etched laser stripe is shown. In the background the top metallization pad is visible. The grating period of this $\lambda \sim 5.3 \mu\text{m}$ wavelength QC-DFB laser is 850 nm.

our gratings were fabricated by optical contact lithography (the grating periods vary from 800 nm for $\lambda \sim 5 \mu\text{m}$ emission wavelength to 1.25 μm for $\lambda \sim 8 \mu\text{m}$) and wet chemical etching in aged HBr:HNO₃:H₂O = 1:1:10. Since a duty cycle of the grating (i.e. the ratio of groove to ridge width) close to unity is preferred in order to obtain a strong first Fourier component of the grating shape function, the obtainable etch depth is for practical reasons limited (e.g. to ~ 350 nm for a grating period of $\sim 1 \mu\text{m}$). (Reactive ion etching or ion-milling as used e.g. in [61] allows more flexibility in the trade-off between grating depth and duty cycle.)

The first QC-DFB lasers were ‘complex-coupled’ structures; i.e. they had both a modulation of the loss and the refractive index, with both being comparable in strength. The plasmon-enhancement layer thickness was $> 0.6 \mu\text{m}$ and was only partly etched by the grating. Single-mode emission was achieved in pulsed operation for two different QC-DFB lasers around 5.3 and 7.8 μm [5]. The best lasers operated single mode in a temperature range from ~ 100 K up to RT (300 K) and displayed single-mode tuning ranges of 70 and 150 nm, respectively. As the temperature is increased both the Bragg resonance via the temperature dependence of the refractive index and the gain spectrum via the temperature dependence of the intersubband structure are shifted to longer wavelength. The red-shift of the peak gain is approximately twice as strong as the shift of the Bragg resonance. The interplay of this temperature-induced detuning with the strength of the Bragg grating is ultimately responsible for the extent of the single-mode tuning range (an initial blue-detuning of gain peak and Bragg resonance can be favourably used to increase the tuning range and single-mode yield). The grating ‘strength’ can be roughly approximated by the coupling coefficient $\kappa = \pi \cdot \Delta n_{\text{eff}} / (2\lambda_0) + i \cdot (\Delta\alpha_w \omega + \Delta\Gamma \cdot g_{\text{th}}) / 4$ [36, 62]. The emission wavelength is denoted by λ_0 ; g_{th} is the gain coefficient at laser threshold; Δn_{eff} , $\Delta\alpha_w$ and $\Delta\Gamma$ are the differences between the effective refractive indices (n_{eff}), waveguide attenuation coefficients (α_w), and confinement factors (Γ) for the waveguides at the locations of the grating grooves and plateaus, respectively. For our early devices we estimated a coupling coefficient $|\kappa| \sim 2\text{--}3 \text{ cm}^{-1}$.

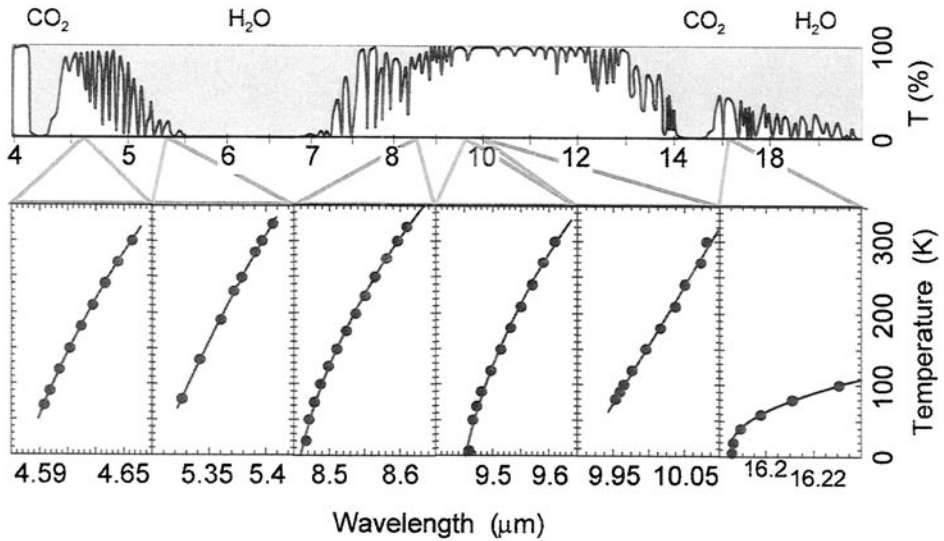


Figure 28. Top, transmission trace of the open atmosphere; the two big ‘windows of atmospheric transmission’ between 3 and 5 μm and 8 and 13 μm wavelength are visible. Bottom, single-mode tuning ranges, shown by the wavelength (circles) versus temperature characteristics, of several exemplary QC-DFB lasers. Tuning characteristics are customarily fitted with quadratic functions or over a reduced temperature range approximated by a linear function (solid lines).

Recent QC-DFB laser designs [36, 63] improved the top-grating approach by using a thinner highly doped, topmost waveguide layer, which could be entirely removed in the grating grooves by etching. This resulted in a greater grating strength with a coupling coefficient $|\kappa| \geq 15 \text{ cm}^{-1}$, which is now clearly dominated by the modulation of the effective refractive index (by a factor of ~ 4). The lasers were designed for $\sim 4.6 \mu\text{m}$ wavelength and also for the wavelength range of 9.5–10.5 μm . The single-mode tuning ranges with heat sink temperature and the lasers operated in pulsed mode were 65 and 150 nm, respectively. Figure 28 shows the tuning curves of some representative lasers (including the 4.6 and 9.5–10.5 μm ones) operated in pulsed mode. The devices at 4.6 μm wavelength were also the first QC-DFB lasers with a top grating to operate in cw; 20 nm of single-mode tuning range were achieved at LN2 temperature, increasing the current through the device from threshold current to approximately twice that value. The heat dissipated in the device by the current is responsible for the temperature increase that leads to the red-tuning of the wavelength.

Although the top grating approach yields quite good results and provides for a straightforward time-saving processing technology, it suffers the fundamental drawback that the Bragg-grating is located only in the exponential tail of the waveguide mode. This ultimately limits the maximum achievable strength of the grating.

Therefore, early on we took another, parallel, approach to QC-DFB lasers, which positions the grating close to the active waveguide core, where the mode intensity is high [60, 64]. In a first growth cycle by MBE, the active waveguide core—a several 100 nm thick InGaAs layer followed by the stack of many (~ 30) periods of alternated active regions and injectors and capped by another ~ 500 nm thick InGaAs layer—is grown. The wafer is then removed from the growth chamber, and the Bragg grating is fabricated into the upper InGaAs layer using the conventional technique. The wafer is then transferred back into another growth chamber, where an InP top cladding is grown on top of the Bragg grating using solid-source MBE. The

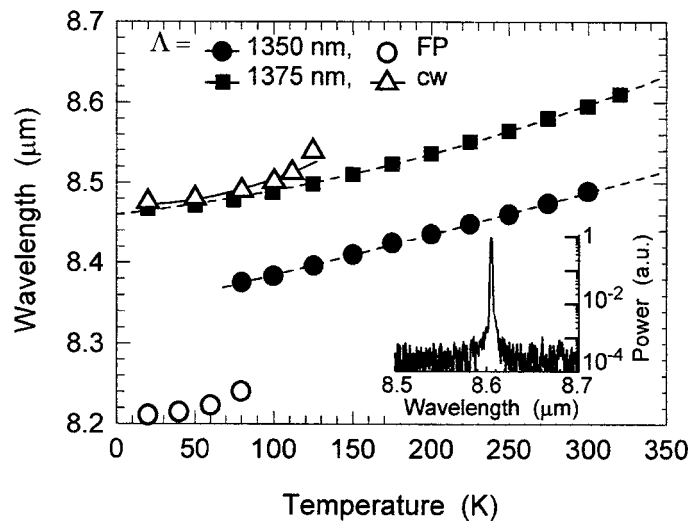


Figure 29. Single-mode tuning characteristics of two lasers with two different grating periods (Λ_p). The squares and circles are data obtained under pulsed operation, the triangles under cw operation. The laser with $\Lambda = 1350 \text{ nm}$ displays laser action on Fabry–Perot modes below $\approx 80 \text{ K}$. This is due to the detuning of the peak gain with respect to the Bragg resonance. This allows Fabry–Perot modes, which emit at the peak gain, to reach laser threshold under high-pumping conditions. The data shown for $\Lambda = 1350 \text{ nm}$ are from a shallow-etched device, which is driven at high current levels due to the lateral current spreading. Inset, single-mode spectrum of a laser operating in pulsed mode at RT. A side mode suppression ratio of $\leq 30 \text{ dB}$ is obtained (\equiv noise level of the measurement set-up). The apparent linewidth is an envelope over the frequency chirp of the single-mode emission during the current pulse.

refractive index contrast between InGaAs (~ 3.49) and InP (~ 3.10) and the strong overlap of the grating with the mode provide for a strong modulation of the effective refractive index of the waveguide and a large coupling coefficient $|\kappa| \sim 30\text{--}80 \text{ cm}^{-1}$. Although the procedure of two growth cycles increases the fabrication efforts, QC-DFB lasers with buried gratings made for the best single-mode laser devices [64]. We have worked extensively in the 5 and $8 \mu\text{m}$ wavelength range with this type of device. Figure 29 shows the single-mode spectrum of such a device at $8.6 \mu\text{m}$ wavelength operated in pulsed mode at RT. The SMSR for QC-DFB lasers readily reaches 30 dB, which qualifies them as ‘single-mode’ lasers. A precise determination of this value is however difficult due to the intrinsic noise floor and lineshape obtained from spectral measurements using a Fourier transform spectrometer and various mid-infrared detectors. Figure 29 also displays the single-mode tuning range ($\sim 150 \text{ nm}$) for this device. QC-DFB lasers with buried gratings also operate without difficulty single mode in cw. Figure 30 shows the cw single-mode spectra and tuning ranges (with heat-sink temperature and drive current) of a similar laser around $7.95 \mu\text{m}$ wavelength. An equivalent performance was demonstrated for lasers around $5.2 \mu\text{m}$. Their cw light output versus current characteristics are equally shown in figure 30. Very high single-mode output power $\sim 150 \text{ mW}$ at LN₂ temperature is achieved for these lasers, and $\sim 120 \text{ mW}$ for the lasers at $7.95 \mu\text{m}$ wavelength.

A third method of incorporating a Bragg grating into a QC-laser waveguide has recently been discussed and demonstrated [65]. Very long wavelength ($\lambda \sim 17 \mu\text{m}$) QC lasers are difficult to fabricate with dielectric waveguides. Furthermore, Bragg gratings for this long wavelength would have to be very deep in order to result in an effective modulation, which makes re-growth on top of such a grating quite difficult.

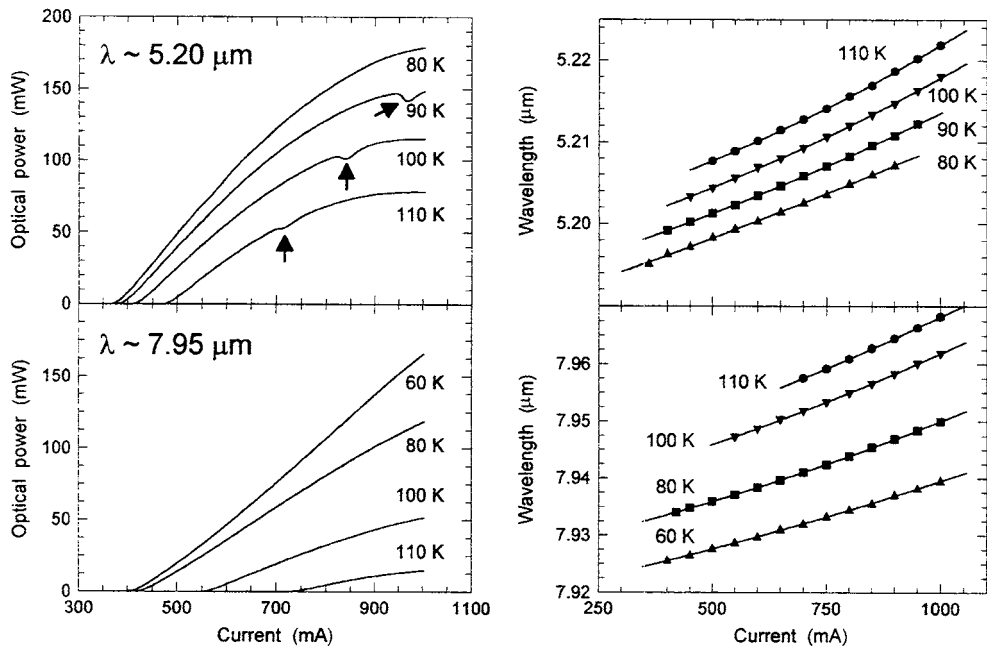


Figure 30. Left, light output versus current characteristics at various constant heat-sink temperatures obtained for two QC-DFB lasers emitting around 5.2 (top) and 7.95 μm (bottom) wavelength and operated in cw mode. The dip in the top traces marked by an arrow is due to an absorption feature in ambient air (identified as water vapour). Right, emission wavelength as a function of the cw current at various constant heat-sink temperatures measured for the same respective lasers. The symbols represent measured data; the curves are quadratic functions fitted to the data.

A fundamentally different waveguide has been found to work well for these long-wavelength lasers; the surface plasmon [45, 47], pinned at the metal–semiconductor interface, functions as the laser mode, with its intensity maximum right at this interface. This type of waveguide will be discussed in more detail in the next section 4.3; nevertheless, here we focus on its use for DFB lasers. The waveguide only consists of the stack of active regions and injectors and the overlying metal layer (which at the same time may act as the top contact). The waveguide parameters (n_{eff} , α_w , Γ) strongly depend on the metal’s dielectric function. Therefore, a Bragg grating fabricated from alternating stripes of two different metals can have sufficient strength for single-mode operation at the very long wavelengths. We demonstrated a pulsed single-mode QC-DFB laser based on this principle using a Bragg grating of alternating titanium and gold (resulting in $\kappa \sim 7 \text{ cm}^{-1}$) with a periodicity of $2.0 \mu\text{m}$; see the photograph in figure 31. The lasers emitted at $16.2 \mu\text{m}$ wavelength with 50 nm tuning range (between 10 and 100 K heat-sink temperature—which was also the temperature range of laser action for this device).

Hofstetter *et al* [66] of the University of Neuchâtel, Switzerland, demonstrated QC-DFB lasers using a so-called ‘surface skimming approach’ and also surface emitting QC-DFB lasers [67] using a higher-order Bragg grating. Schrenk *et al* [61] from the Technical University of Vienna, Austria, demonstrated single-mode DFB devices for QC lasers in the GaAs/AlGaAs material system, and an in-depth mathematical treatment of QC-DFB waveguides can be found in Finger *et al* [62].

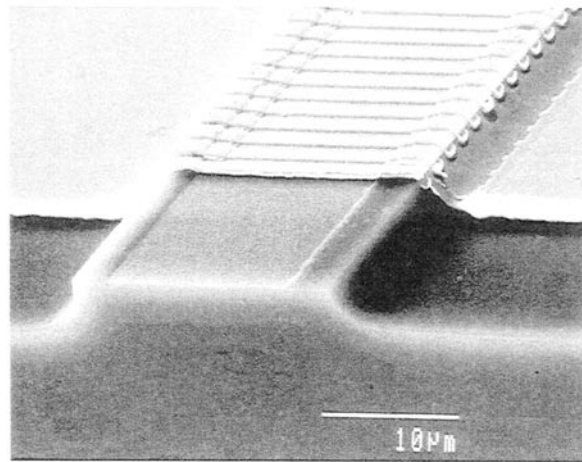


Figure 31. Scanning electron microscope image of a portion of an SL-QC-DFB laser featuring a surface-plasmon waveguide and two-metal-grating approach. The cleaved mirror section of the deep-etched laser stripe is shown. The top metallization features a grating of alternating gold and gold-over-titanium stripes. The grating period of this $\lambda \sim 16.2 \mu\text{m}$ wavelength QC-DFB laser was $\sim 2 \mu\text{m}$.

4.3. Surface-plasmon waveguides

The typical dielectric waveguide as described in the previous sections is based on refractive index contrast and consists of the waveguide core, with high refractive index, sandwiched between waveguide cladding layers of lower refractive index. The ratio between the refractive indices, the thickness of the waveguide core and the polarization of the electro-magnetic field determine the transverse dimension (i.e. the full width at half maximum (FWHM) value) of the mode intensity profile normal to the layers and the confinement factor Γ of the guided mode.

The transverse dimension of the confined modes is roughly proportional to the effective wavelength of the radiation in the layered material. For semiconductor lasers with emission wavelength in the mid-infrared or even far-infrared, growth of very thick core and cladding layers would then be required to efficiently confine the electromagnetic modes. Here we describe a successful approach for long-wavelength semiconductor laser waveguides in which the modes are not supported by a layered transparent medium but are electromagnetic surface waves (surface plasmons) at a metal–semiconductor interface [45–47, 65, 68]. In principle, no additional confinement layer is needed since the amplitude of the optical wave decreases exponentially in the two directions normal to that interface. These guided transverse-magnetic (TM) modes exist always at the interface between two media which have dielectric constants of opposite sign, as it is the case with a metal and a semiconductor. Therefore, the metal layer, which is usually deposited as electrical contact on the top surface of a semiconductor laser, is now deposited directly above the active material of the device and is used as the guiding interface. This allows us to omit the cladding layers and drastically (often by a factor of two to three) reduces the total thickness of the layers grown by MBE. However, surface waves at a metal–dielectric interface suffer from high optical losses if the mode penetrates into the metal. These losses are therefore less effective in the mid-infrared, where the penetration depth is smaller, than at shorter wavelengths, where the absorption coefficient of the metals is less strong. It follows that the losses at the interface can be minimized by choosing metals having a complex refractive index ($\bar{n} = n + i \cdot k$) with a strong imaginary component ($k \gg n$) [68].

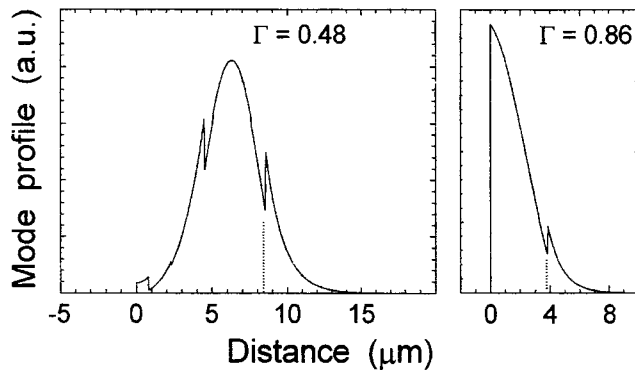


Figure 32. Left, mode intensity profile of an optimized dielectric plasmon-enhanced waveguide designed for $\lambda \sim 17 \mu\text{m}$ wavelength. Right, mode intensity profile of a surface-plasmon waveguide designed for the same wavelength. The stack of active regions and injectors is indicated through a shaded bar. The dashed lines show the respective substrate–epilayer interfaces, and the origin of the horizontal axis is located at the metal–semiconductor interface.

Among those metals, which are commonly used for device fabrication, gold is optically the most suitable for application to QC lasers at wavelengths $\lambda \geqslant 15 \mu\text{m}$.

Optimized waveguide structures, though, are more complicated than a simple metal–semiconductor interface. The significant difference is the low-doped InGaAs layer and the InP substrate beneath the QC-active region and injector stack. This layer combination strongly reduces the penetration of the mode into the substrate, and therefore increases the confinement factor of the active regions. To obtain a more accurate prediction of the intensity pattern and modal losses of the TM interface modes a numerical calculation based on the transfer matrix method has been used. The results are presented in figure 32 for a laser wavelength of $17 \mu\text{m}$. These waveguides achieve a clear enhancement of the confinement factor (often $\Gamma \geqslant 0.8$) over a regular dielectric waveguide ($\Gamma \sim 0.4\text{--}0.5$) with the same thickness of the waveguide core and comparable waveguide loss.

The extension of QC lasers to the far-infrared wavelength range ($\lambda_0 \geqslant 20 \mu\text{m}$) is of particular interest due to the lack of narrow-band, powerful and compact sources in this wavelength range. The surface-plasmon waveguides are particularly attractive for such long wavelengths—due to the clearly reduced penetration depth—and are essential to reduce the otherwise prohibitively high threshold current densities. In section 3.2 several far-infrared SL-QC lasers with surface plasmon waveguides were described [47].

While the surface-plasmon waveguide solution provides very high performance for long-wavelength ($\lambda_0 = 17\text{--}24 \mu\text{m}$) QC lasers, it is obvious from waveguide calculations that for the realization of QC lasers at wavelengths on the lower-energy side of the reststrahlen band ($\lambda_0 \geqslant 50 \mu\text{m}$), the waveguide design must be further improved. For this reason, Colombelli *et al* [47] designed and fabricated a laser in which the low-doped InGaAs layer directly below the cascade stack was replaced by a 750 nm thick highly doped ($\geqslant 10^{19} \text{ cm}^{-3}$) InGaAs layer. This highly doped semiconductor acts as a bottom ‘metal’, thus realizing a ‘double-sided’ surface-plasmon waveguide, with an extremely high confinement factor $\Gamma = 0.98$. However, in order to keep the calculated waveguide losses at the level of comparable single-sided surface plasmon waveguides, the thickness of the waveguide core was roughly doubled by increasing the number N_p of active region and injectors. The device exhibited a threshold current density of $J_{\text{th}} = 7.1 \text{ kA cm}^{-2}$, approximately 1.7 times the threshold of a comparable single-sided surface-plasmon SL-QC laser, likely a result of a deeper penetration of the guided mode into

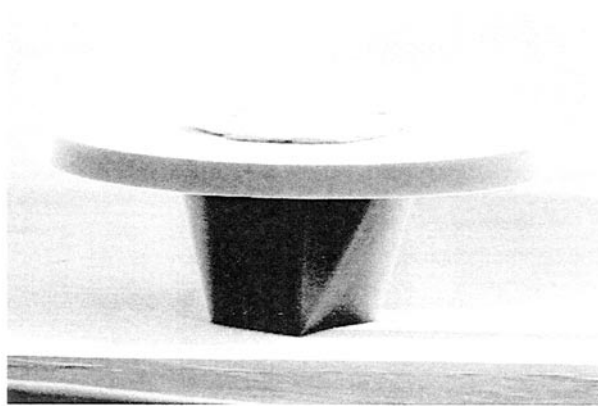


Figure 33. Scanning electron microscope image of a QC microdisc laser. Discs are typically 2–4 μm thick, and range in diameter from 10 to 150 μm , for wavelengths around 5–9 μm . The disc is made from ternary InGaAs/AlInAs material; the pedestal is composed of Highly doped InP and acts as bottom contact. The top metal contact pad is also visible. Light emission occurs in the plane of the disc.

the highly doped InGaAs layer. Nevertheless, the ‘double-plasmon’ laser should prove useful for even longer far-infrared and submillimetre-wavelength QC lasers.

4.4. Micro-cavity and whispering-gallery type resonators

Microcavity lasers have attracted intense attention in recent years in light of their potential as spectrally narrow, low-threshold, and low-noise laser sources. By reducing the size of an ideal resonator towards the limit of a ‘half-wavelength cube’ the number of modes within the resonator is reduced to one and spontaneous emission is entirely coupled into a single mode, thus eliminating the optical losses into other modes. In the limit of negligible losses, i.e. a very high-quality (Q) resonator, this results in a virtually thresholdless laser.

One straightforward and particularly advantageous microcavity geometry for QC lasers is the so-called ‘whispering-gallery microdisc’ resonator. Figure 33 shows a photograph of a QC microdisc laser.

The whispering-gallery laser has an intrinsic three-dimensional mode confinement. Whispering-gallery modes correspond to light travelling close to the perimeter of and inside the disc impinging on its edge with angles larger than the critical angle of refraction. In an intuitive picture—drawn from curved-waveguide analysis [69]—the whispering-gallery mode confinement can be viewed as due to a triangular ‘potential’ well in the effective refractive index profile at the edge of the disc.

QC lasers are especially suited for the disc geometry due to their lack of surface recombination, inherently in-plane, transverse-magnetic TM mode emission and reduced Rayleigh scattering of the longer wavelength on surface imperfections. Since the emission wavelength of a QC laser is determined by the intersubband transition within the QWs in the active region, it is straightforward to approach the microcavity limit of a QC-disc laser not only by size reduction but also by increasing the emission wavelength.

QC-disc lasers have been reported with emission wavelengths of $\lambda_0 \approx 5.2 \mu\text{m}$ [70], $\lambda_0 \approx 9.5 \mu\text{m}$, $11.5 \mu\text{m}$ [71] and $\lambda_0 \approx 16 \mu\text{m}$ [72]. Thus, most of the spectral range reported for QC ridge waveguide lasers is also covered by QC-disc lasers. The latter demonstrates the

general compatibility of the disc resonator with the QC-laser active material.

QC-microdisc lasers based on the InGaAs/AlInAs on InP material system are fabricated in a two-step process. First, deep cylinders are wet-chemically etched using a material non-selective etch. Secondly, the InP substrate is selectively removed (using a heated dilute hydrochloric acid solution) from under the InGaAs/AlInAs disc, until it forms a pedestal of the desired size and shape. The discs are contacted via a probed metal contact on top, and the doped InP pedestal on the bottom.

The quality factor, one important quantity for disc lasers, can be estimated from

$$Q = \frac{2\pi n_{\text{eff}}}{\lambda_0 \cdot J_{\text{th}} g \Gamma_{\text{act}}} \quad (14)$$

where $J_{\text{th}} g \Gamma_{\text{act}} = \Gamma_{\text{core}} \alpha_{w,\text{core}} + \Gamma_{\text{clad}} \alpha_{w,\text{clad}} + \alpha_{\text{scatt}}$ equals the losses given by the sum of the waveguide and outcoupling loss. Since portions of the waveguide mode are guided in the lossless vacuum surrounding the thin disc, we needed to include a confinement—better, overlap—factor Γ also for the various waveguide layers. Also, note that there are no true mirror losses, as light is confined by total internal reflection inside the disc. g is the gain coefficient, and λ_0 the wavelength in vacuum. From these sets of parameters quality factors of $Q = 3400$ have been measured for a disc laser emitting at $\lambda_0 = 5.2 \mu\text{m}$, $Q = 206(\lambda_0 = 9.5 \mu\text{m})$ for a $2 \mu\text{m}$ thin disc and $Q = 133(\lambda_0 = 9.5 \mu\text{m})$ for a $2.5 \mu\text{m}$ thin disc. At $\lambda_0 = 11.5 \mu\text{m}$ a quality factor of $Q = 68$ was obtained. This evident decrease of the Q -factor with increasing wavelength is a direct consequence of the increase in waveguide loss (also observed in ridge-waveguide QC lasers) and the enhanced outcoupling due to loss of vertical confinement in thin discs. Unfortunately, this decrease in quality factor also prevents the fabrication of thresholdless lasers using QC-microdisc resonators.

Nevertheless, subsequent work [7] demonstrated that QC active material can be used as a very ‘clean’ model system for other studies involving whispering-gallery type resonators. Microdisc, -cylinder or -droplet lasers form a generic class of lasers based on circularly symmetric resonators, which show laser action on ‘whispering-gallery modes’ of the electromagnetic field. In such a mode—as mentioned above—light circulates around the curved inner boundary of the resonator, reflecting from the walls of the resonator with an angle of incidence always greater than the critical angle for total internal reflection, thus remaining trapped inside the resonator. There are only minute losses of light caused by evanescent leakage (tunneling) and scattering from surface roughness. Therefore, as a serious disadvantage, the tiny ‘whispering-gallery’ type lasers lack high output power and directional emission because of the high-reflectivity mirrors and the circular symmetry. In [7] a new resonator design which incorporates chaotic ray motion has been used to dramatically increase the output power and directionality of such lasers.

Recent theoretical work has provided insight into the behaviour of ‘asymmetric resonant cavities’ (ARCs), ‘whispering-gallery’ resonators with smooth deformations from cylindrical or spherical symmetry [73]. The ray dynamics in these deformed resonators is known to be either partially or fully chaotic in the generic case. The best studied example is a two-dimensional resonator with a quadrupolar deformation of the circular boundary, described in polar coordinates (r, φ) by $r(\varphi) \propto (1 + \varepsilon \cdot \text{Cos}(2\varphi))$, where ε is the deformation parameter. Partially chaotic ‘whispering-gallery’ modes in these resonators have shown directional lasing emission in low-index materials (index of refraction $n < 2$, such as glass fibres or cylindrical dye jets) [73]. The origin of the directional emission is the following: the deformed boundary causes the angle of incidence of a ray in a ‘whispering-gallery’ mode to fluctuate in time. Eventually a ray trapped by total internal reflection impinges on the boundary below the critical angle and escapes by refraction. However, it was not appreciated in this earlier theoretical work

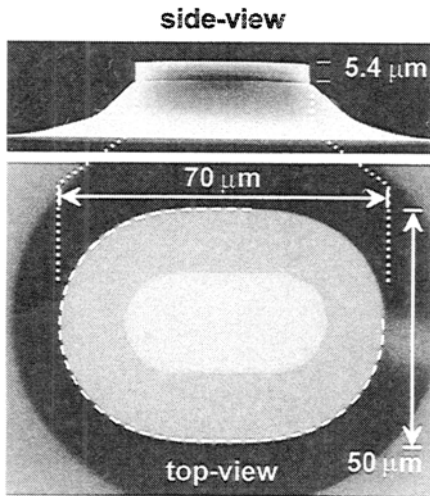


Figure 34. Scanning electron microscope image of the side and top view of a flattened quadrupolar shaped cylinder QC laser. The deformation parameter is $\varepsilon \approx 0.16$. Side view, the laser waveguide and active material is entirely contained in the disc—with vertical side walls, total thickness $d = 5.39 \mu\text{m}$ —on top of a sloped InP pedestal. Top view, the top face of the laser is shown in medium grey, the electric contact in light grey. The laser boundary is very well described by an exact flattened quadrupole with $\varepsilon = 0.16$, which is drawn as a dashed curve over parts of the circumference.

that, in high-index materials, qualitatively different modes not of the ‘whispering-gallery’ type might be relevant to the laser properties.

Here we focus on semiconductor lasers that have an effective index of $n \approx 3.3$ and a deformation of the boundary best described by $r(\varphi) \propto (1 + 2 \cdot \varepsilon \cdot \cos(2\varphi))^{1/2}$, which we shall refer to as a ‘flattened’ quadrupole. In general, one can parametrize the boundary of any convex resonator by an arbitrary Fourier series for $r(\varphi)$; the above parametrization is chosen for convenience, because it is simply analysed and describes the actual resonator shapes quite well. Figure 34 shows a photograph, top and side view, of such a laser. We show that for small deformations ε the basic picture of chaotic ‘whispering-gallery’ orbits escaping refractively, as described above, still holds for the high-index semiconductor material. However, we also present strong experimental evidence that at larger deformations a different type of laser resonance emerges and is responsible for highly directional and high-power emission. Unlike the chaotic ‘whispering-gallery’ modes of smaller deformations, these so-called ‘bow-tie’ resonances are stable resonator modes surrounded on all sides (in phase space) by chaotic motion.

The cylinder lasers are fabricated by optical lithography and wet-chemical etching from conventional QC-laser material with semiconductor dielectric cladding. The quadrupolar-like shape is obtained starting from a resist pattern that is composed of two semi-circles connected by a rectangle (stadium shape). The samples are then etched until deep mesas are obtained. Because of the smoothing action of the etch solution the straight section of the etch mask bends toward the curved parts rendering a quadrupole-like shape. Ohmic contacts are applied to the front and back surface of the lasers by using non-alloyed Ti/Au and Ge/Au/Ag/Au, respectively. The deformation parameter ε was varied in ten steps from 0 to ≈ 0.2 and the size of the cylinders is best described with a short diameter of $\approx 50 \mu\text{m}$ and the long diameter varying from $\approx 50 \mu\text{m}$ ($\varepsilon = 0$) to $\approx 80 \mu\text{m}$ ($\varepsilon \approx 0.2$).

The lasers emit light according to their symmetry into all quadrants of the two-dimensional laser plane. Light output measurements for various lasers as a function of their deformation ε are shown in figure 35(a). To generate this plot, the maximum obtainable peak power was recorded for each laser by optimizing the pulsed drive current. The collecting aperture (slit width corresponding to $\approx 15^\circ$) was oriented around $\varphi = 0^\circ$. Note that this setup precludes the observation of any changes in the far-field directionality with deformation. Similar measurements were performed with the aperture oriented around $\varphi = 45^\circ$ and 90° . The

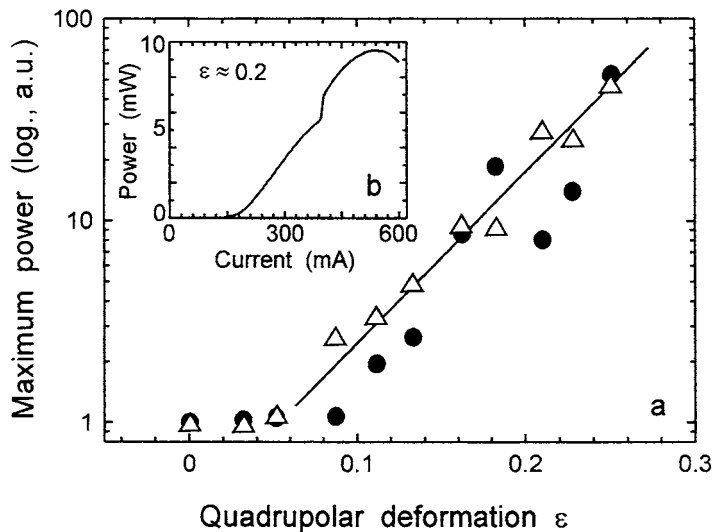


Figure 35. (a) Maximum peak optical power from various lasers as function of their quadrupolar deformation parameter ϵ . The aperture with width 15° is centred around zero degrees. Data from two independent sets of lasers are given. The power output is normalized to the power of the respective circular cylinder laser. (b) Light-output-to-current characteristics of a quadrupolar cylinder laser with deformation $\epsilon \approx 0.2$. The collecting aperture ranges from $+40^\circ$ to $+100^\circ$ (the polar coordinate system is described in figure 36(c)). The kink around 400 mA indicates the onset of a second laser mode. The measurement has been performed at 100 K heat-sink temperature.

striking result is the strong (quasi-exponential) increase of the collected optical power with deformation. For the largest deformation under consideration ($\epsilon \approx 0.2$), a power increase of a factor of ≈ 50 with respect to the circular case is observed. Figure 2(A) shows a representative measurement taken at $\varphi = 0^\circ$.

The absolute output power was measured in some highly deformed laser devices by bonding and mounting them in a calibrated setup usually used with Fabry–Perot type lasers. One example, obtained from a laser with $\epsilon \approx 0.2$, is shown in figure 35(b). The light collecting aperture was increased to its maximum size, and the sample was rotated to detect roughly the optical power in an angle from $+40^\circ$ to $+100^\circ$. The choice of this aperture, which exploits far-field anisotropy, will become clear below. A peak output power of ≈ 10 mW at 100 K was obtained. This value is approximately three orders of magnitude greater than that obtained from the non-deformed (circular cylindrical) laser or previous conventional circular QC-disc lasers [70]. For a weakly deformed laser ($\epsilon = 0.06$) we estimate a peak power output of ≈ 50 μ W (when measured with comparable collection efficiency to the laser of figure 35(b)).

A quasi-exponential increase of the collected power with increasing deformation (similar to the one shown in figure 35(a)) has been measured in numerous sets of lasers of various—flattened and less flattened—quadrupolar shapes and sizes, and with various orientations of the aperture. Thus it appears that the power increase is a reliable, universal effect. However, the increase in output power per unit angle is rather closely entangled with the actual variation of the far-field pattern with deformation. In fact, in our lasers the power increase with deformation results from the lasing of different types of mode in different ranges of ϵ . There is a cross-over at intermediate deformations ($\epsilon \approx 0.12$) from emission via ‘whispering-gallery’ modes, which dominates at smaller deformations, to laser emission from ‘bow-tie’ modes which do not exist below $\epsilon \approx 0.10$ but dominate the high-deformation regime.

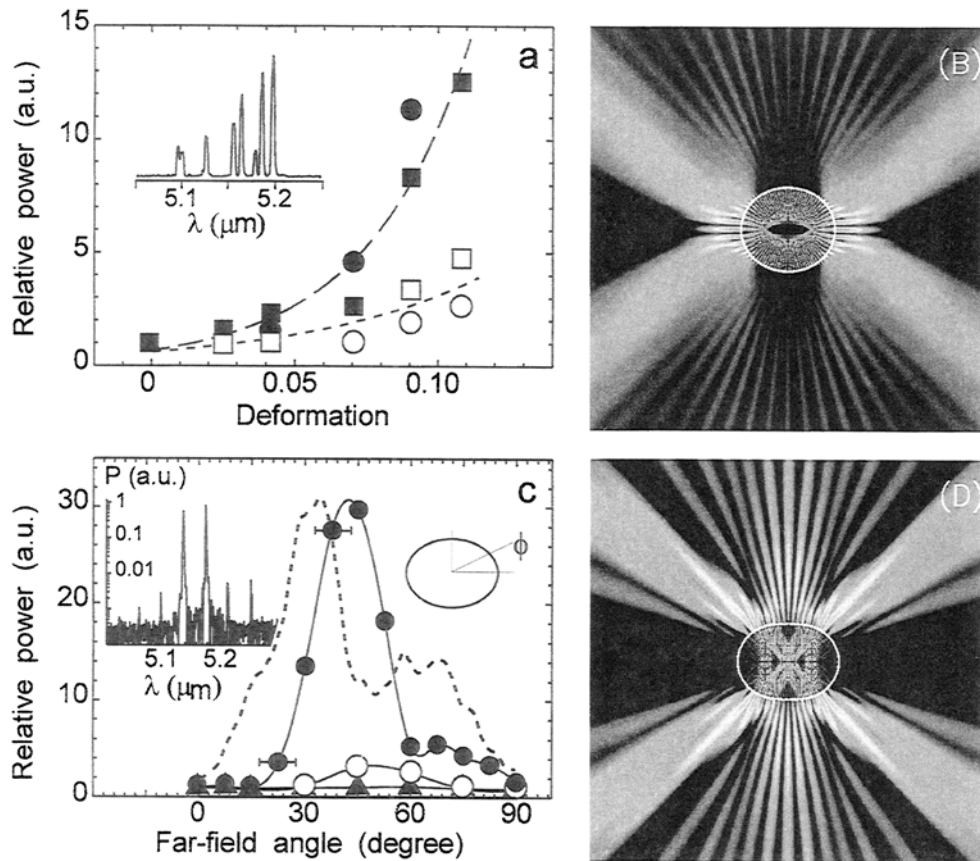


Figure 36. (a) Peak output power of different lasers as a function of deformation. The power is collected around 0° (open symbols) and 90° (filled symbols) with a width of the fixed aperture of 15° . Two independent sets of lasers are presented for each orientation of the aperture. Both curves rise approximately exponentially, as indicated by the dashes. Inset, spectrum in linear scale obtained near peak optical power from a cylinder laser with low deformation ($\epsilon \approx 0.04$). (b) Grey-scale representation of the radiation intensity pattern of a chaotic ‘whispering-gallery’ mode for a deformed cylinder with $\epsilon = 0.06$ and length of the minor axis of $50\ \mu\text{m}$. Light indicates high intensity, dark minimum intensity. (c) Symbols indicate the measured angle-resolved far-field pattern (one quadrant) of a circular (triangles) and two deformed lasers with $\epsilon = 0.14$ (open circles) and $\epsilon = 0.16$ (filled circles). The data-sets are normalized to the value measured at zero degrees. The data points are connected by splines (solid curves) for clarity. The dashed line is the far-field intensity pattern associated with the bow-tie mode shown in figure 3(d), averaged over the experimental aperture. The calculation has been scaled to match the peak emission at $\approx 45^\circ$. Left inset, logarithmic plot of the measured spectrum at maximum power (power P versus wavelength λ) of a laser with $\epsilon \approx 0.16$. Six equally spaced modes, with mode spacing $\Delta\lambda = 40.4\ \text{nm}$, are observed. This mode separation is in good agreement with the value of $39.5\ \text{nm}$ calculated for a ‘bow-tie’ orbit corresponding to the calculated intensity pattern of figure 3(d). Right inset, the polar coordinate system is oriented such that $\varphi = 0^\circ$ indicates the direction along the elongated (major) axis, and $\varphi = 90^\circ$ denotes the direction of the compressed (minor) axis. (d) Grey-scale representation of the intensity pattern of a ‘bow-tie’ mode for $\epsilon = 0.15$ and length of the minor axis of $50\ \mu\text{m}$. The linear grey scale is unrelated to the scale of figure 3(b).

In addition to the strong increase in power output, the deformed lasers can also provide strong directionality. The results of the far-field measurements are summarized in figures 36(a)

and (c). As expected, the circular cylinder laser displays *no* directionality of the emission. At small deformations ($\varepsilon \leq 0.10$), the far-field is only weakly structured with an increased emission in direction of the minor axis compared to the major axis. Figure 36(a) shows the increase of the output power with ε , collected around 0° and 90° . Both curves rise approximately exponentially, as discussed in the previous section, but ‘faster’ for $\varphi = 90^\circ$; in this case the exponent is increased by a factor of ≈ 2 with respect to the $\varphi = 0^\circ$ case.

This observation is consistent with the expected behaviour of deformed ‘whispering-gallery’ modes with an average angle of incidence near the critical angle defined by $\sin(\chi_c) = 1/n_{\text{eff}}$, where $n_{\text{eff}} \approx 3.3$ is the effective refractive index of the laser waveguide. At zero deformation such a mode has a conserved angle of incidence and emits isotropically and uniformly via evanescent leakage from all points at the boundary (neglecting disorder effects, such as surface roughness scattering). However, when the boundary is deformed the angle of incidence of a ray associated with a laser mode fluctuates and (at these deformations) is most likely to collide with the boundary below the critical angle of incidence at or near a location of high curvature ($\varphi = 0^\circ, 180^\circ$). Figure 36(b) shows the calculated intensity pattern (the modulus squared of the electric field) for a typical ‘whispering-gallery’ mode in a deformed cylinder laser with $\varepsilon = 0.06$. The pattern shows clearly the enhanced emission intensity in the near-field in the vicinity of ($\varphi = 0^\circ, 180^\circ$). The experiments are sensitive to the far-field intensity distribution, which depends also on the angle of refraction at the points of high curvature. Both the ray and wave calculations [7] indicate that at this deformation all ‘whispering-gallery’ modes with high output coupling have a minimum in emission intensity in the far-field around $\varphi = 0^\circ$ and enhanced emission between 45° and 90° . The observed experimental intensity pattern has this general trend (see figure 36(a)), but a fully angle- and mode-resolved measurement of the far-field pattern and a detailed comparison with theory is difficult due to the generally low optical power and the many modes which contribute to the laser signal in this regime of deformations.

At higher deformations ($\varepsilon \geq 0.14$) we detect a much stronger and qualitatively different directionality. Figure 36(c) shows the actual angle-resolved far-field pattern (one quadrant) of one circular and two deformed lasers. For the laser displayed in figure 34, we obtain a power increase by a factor of 30 into an emission angle of $\varphi = 42^\circ$ compared with $\varphi = 0^\circ$. The angular width of this directional emission is $\approx 23^\circ$. Around 0° we observe a clear minimum of the emission, and a smooth sloping plateau towards 90° .

At these large deformations, a typical ray characterizing a ‘whispering-gallery’ mode escapes in fewer than ten collisions with the boundary. This ray escape is now approximately isotropic and would seem unlikely to lead to the increased emission anisotropy observed experimentally. Because the general ray motion is furthermore highly chaotic in most of the phase-space, the only plausible scenario for generating directional emission is for the laser modes to be associated with the small regions of stable, regular motion that still remain.

For the range of deformations $\varepsilon \approx 0.12$ to 0.23 , there exist only two such regions. The first is the vicinity of the basic diametral orbit running along the minor axis of the resonator. The associated modes are the transverse modes of the stable, curved-mirror Fabry–Perot resonator. However, these modes correspond to normal incidence at the boundary and, as such, would result in a peak emission at 90° in the far-field, much in contrast to the observation. Furthermore, the low reflectivity of the boundary at normal incidence combined with the short length of the minor axis result in a too high threshold for laser action.

The second region is in the vicinity of the stable four-bounce periodic orbit with the shape of a ‘bow-tie’ in real space. The intensity pattern of a representative ‘bow-tie’ mode is shown in figure 36(d). This orbit comes into existence by bifurcation from the diametral orbit at $\varepsilon \approx 0.10$ and has four equal (in absolute value) angles of incidence on the boundary. At

$\varepsilon \approx 0.12$ this angle $\chi \approx 12.5^\circ$ and it is well below the critical angle, but as the deformation increases to $\varepsilon \approx 0.15$ this angle increases to approximately the critical angle, $\chi_c \approx 17.5^\circ$. This change results in a sufficiently high reflectivity of the boundary to allow for laser action. For ε of 0.125, 0.14 and 0.15, values of the reflectivity of 0.45, 0.59 and 0.72 are calculated, respectively. Thus the ‘bow-tie’ modes become the most favourable for laser action, with low thresholds, high peak optical power and strong directionality.

We would finally like to note that ‘bow-tie’-type laser resonators have also been studied carefully for GaAs-based QC lasers by Gornik *et al* [74].

5. Special quantum cascade laser designs

In the previous sections 3 and 4 we focused on the most successful, i.e. highest-performing and most broadly used, QC-laser designs. However, as we shall demonstrate in this section, band-structure engineering [23] allows one not only to optimize the lasers for general performance, but it also enables the design of very specialized QC and SL-QC lasers with features highly unusual for any other semiconductor lasers. One prime example is multiple-wavelength operation of QC lasers, two quite different versions being discussed below. Furthermore, using an ‘injectorless’ QC-laser as example, we will show that intersubband laser action can be achieved even under violation of the most basic QC-laser design rules, namely, that injector regions are needed to bridge successive active regions together.

5.1. Multiple-wavelength superlattice laser

In section 3.2 we discussed modulation-doped SL-QC lasers with effectively field-free SL active regions and also ‘chirped’ SL-QC lasers. In both cases we stressed the importance for the subband level spacing in the upper miniband to be close to the LO-phonon energy in order to provide fast carrier relaxation to the miniband edge. In this section, we summarize results on the realization of a QC laser based on an SL active region with several distinct optical transitions between miniband states in which this relaxation is purposely slowed down. Simultaneous multiple-wavelength laser action in the mid-infrared is then achieved by design of the electronic states and electron relaxation times [75, 76]. In the present device, we consider an active material intermediate between an SL structure with continuous energy minibands, and multiple QWs with individual confined subbands. Namely, the electronic states are delocalized over many wells and grouped together in miniband-like manifolds, but their energy separation is sufficiently large when compared to the linewidth broadening that they can still appear as distinct features in the luminescence spectrum. We have chosen eight-period SLs, which results in discretized minibands composed of eight states. Eight well defined optically allowed transitions, vertical in space and with relatively large oscillator strengths, are obtained between the first two minibands, each with a distinct frequency, and each corresponding to a different point of the Brillouin minizone. The structure is designed so that laser action can take place simultaneously on the transitions indicated as 4–1 and 3–2 in figure 37. The energy separation E_{43} between the upper states 4 and 3 is a critical parameter. First of all, it has to be large enough to have the difference between the emitted photon energies considerably greater than the broadening of the two transitions. On the other hand, since a sufficient population inversion has to be realized between 4 and 1, the relaxation rate of electrons from 4 to 3 must be kept small. This can be done by hindering the emission of optical phonons, which is the dominant scattering process, by designing E_{43} to be less than the LO-phonon energy. This poses stringent requirements on the maximum acceptable broadening. To minimize the latter, we have used intrinsic SLs that are kept electric-field free under the applied bias by the use of special

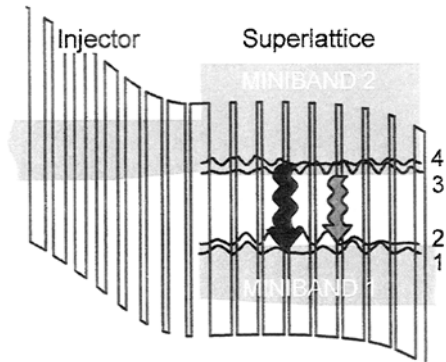


Figure 37. Calculated energy diagram of one active region with the preceding injector region of an SL-QC laser with field-free SL capable of laser action on multiple wavelengths simultaneously. The two laser transitions 3–2 and 4–1 are indicated by shaded wavy arrows. The moduli squared of the wavefunctions 1–4 are shown as well.

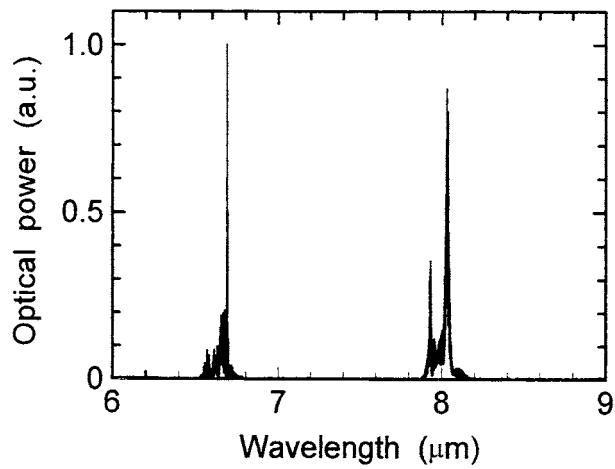


Figure 38. Emission spectrum of the SL-QC laser depicted in figure 37 operated in pulsed mode at a current level above the threshold for multiple-wavelength operation. The actual Fabry–Perot modes cannot be resolved in this plot. Multiple-wavelength operation is obtained over a very wide temperature range; the spectra shown here have been taken at cryogenic temperature.

injection regions with an appropriate doping profile, as discussed in section 3.2. This leads to luminescence linewidths as small as 15 meV. The actual conduction-band profile of one SL with the two adjacent injectors is shown in figure 37, together with the wavefunctions of the relevant levels. The miniband of each injector region is realized so as to provide fast extraction of the electrons from the first miniband of the preceding SL active region and efficient injection into states 4 and 3 of the second miniband of the next SL. We calculate for the two transitions the wavelengths $\lambda_{41} = 6.4 \mu\text{m}$ and $\lambda_{32} = 7.9 \mu\text{m}$, and the transition matrix elements $z_{41} = 1.9 \text{ nm}$ and $z_{32} = 3.2 \text{ nm}$. Relaxation through optical phonon emission into the other levels of the first miniband controls the lifetimes of states 1 and 2 (0.2–0.3 ps), that are much shorter than the optical phonon scattering times $\tau_{32} = \tau_{41} = 10.5 \text{ ps}$, thus ensuring population inversion. The total lifetimes of the upper states, neglecting the 4 to 3 relaxation processes, are computed to be $\tau_3 = 0.9 \text{ ps}$ and $\tau_4 = 1.1 \text{ ps}$, obtained from adding the scattering rates to all the states of the first miniband.

In figure 38, we show the emission spectra of one such laser at a temperature of 80 K. For current pulse amplitudes of 2 A, only one laser line is visible at $7.9 \mu\text{m}$, but above 4 A a second line sets in at $6.6 \mu\text{m}$, in good agreement with the expected wavelengths. Above 10 A, a third

emitted wavelength appears at approximately $7.3\ \mu\text{m}$. The latter originates from a transition diagonal in space, between states 4 and 2, which acquires a large enough dipole matrix element at high electric field as the latter starts to penetrate into the SL, weakening its symmetry [76].

5.2. Bi-directional, dual-wavelength, quantum cascade laser

Most optoelectronic semiconductor devices, such as conventional semiconductor lasers, light emitting diodes and solar cells, are bipolar, that is, they contain a combination of semiconductor layers doped with donor impurities (n-type doped) and with acceptor impurities (p-type doped). The resulting built-in electrostatic potential provides an inherent directionality to these devices and renders them functional for a specific voltage polarity. In contrast, unipolar optoelectronic devices such as QC lasers offer the possibility of bi-directional use.

Here, a bi-directional, unipolar QC laser is discussed [51]. Unlike all other QC and SL-QC lasers, it operates as a light source under both positive and negative bias voltage. In addition, the operating wavelength can be made different in the two polarities. These features provide new functionality not available in conventional semiconductor lasers, potentially opening the door to many useful applications.

In general, reversing the applied bias in any conventional QC laser alters the energy level structure, thus preventing laser action. The device presented here operates instead as a different QC laser in each polarity.

In the diagram describing the basic principle of operation of the bi-directional QC laser (figure 39) a portion of the conduction band structure, two active regions with the connecting injector region, is shown. In the present design, under an appropriate applied positive bias (figure 39(a)), laser action takes place from level G_+ to level 1, via a photon-assisted tunneling or diagonal transition (wavy arrow). This case has been discussed in detail in section 3.3. The emitted photon energy is controlled, for a given active region QW, by the thickness of the injector layers in the immediate vicinity of the injection barrier and by the applied electric field. A reversal of the bias polarity (figure 39(b)) will localize the injector ground state G_- at the opposite end of the injector miniband. With an injector entirely symmetric around its centre, G_+ and G_- would be equivalent and the laser wavelength would be the same in both polarities. If, however, the injector regions are designed as asymmetric, the energy position of G_- will be different from that of G_+ leading to different laser wavelengths λ_+ and λ_- .

The exact layer design, a portion of the bandstructure and the moduli squared of the relevant wavefunctions of a representative sample have already been shown in figure 22. The relevant quantity in the threshold gain is $k_{\pm} = z_{\pm}^2 \cdot E_{\pm} \cdot \tau_{\pm}$. The indices imply that these values can be set independently for each bias direction. If one is interested in a device with two different emission wavelengths, that is, $E_+ \neq E_-$, but comparable threshold current and voltage, as was the case for [51], then z_{\pm} and τ_{\pm} need to be adjusted to achieve $k_- = k_+$ at the same applied electric field, regardless of the polarity.

Other factors have to be considered in the design of bi-directional lasers. First, in a diagonal-transition QC laser the transition matrix element and photon energy vary noticeably with the applied electric field until the laser threshold is reached. This variation with applied bias has to be taken into account when z_{\pm} and τ_{\pm} are scaled to account for the desired difference in photon energy E_{\pm} between opposite polarities.

Second, although one would expect the losses to be independent of bias polarity, the respective design in either polarity has to be analysed to avoid an accidental resonant intersubband optical absorption.

Third, the injector regions are doped in their centre wells and barriers. In general, the extrinsic electrons and the electrical potential of their donor ions will modify the bandstructure.

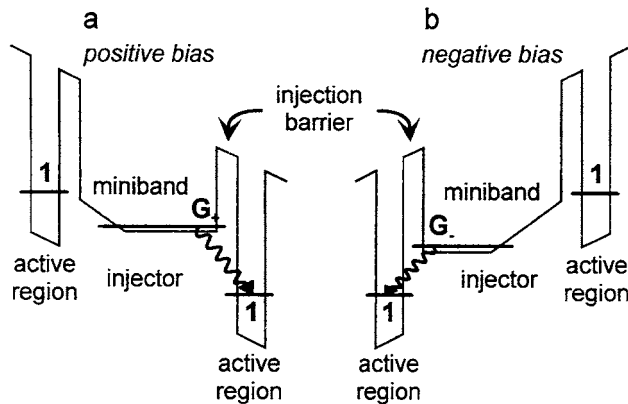


Figure 39. Schematic energy diagram for the operation of the bi-directional QC laser. (a) A portion of the conduction-band structure—two active regions with the intermediate injector region—is shown under a positive applied bias. Electrons traverse the structure from left to right. (b) Schematic band structure of the same QC laser under opposite (negative) bias. Electrons traverse the structure from the opposite direction. Depending on bias polarity, laser action takes place between different pairs of energy levels ($G_+ - 1$ versus $G_- - 1$), leading to bias-polarity-dependent laser characteristics.

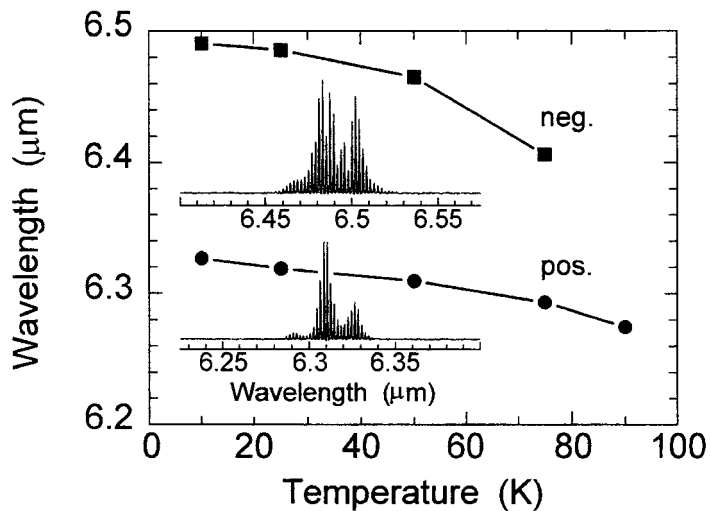


Figure 40. Device characteristics of a bi-directional QC laser with two different emission wavelengths for opposite bias polarities as depicted in figure 39. The peak emission wavelength is shown as a function of the heat-sink temperature for positive (bottom) and negative (top) polarity. The insets show examples of the corresponding Fabry-Pérot type emission spectra.

We verified that this effect is negligible through self-consistent calculations of the bandstructure including the extrinsic charges, and through measurements on two symmetric, bi-directional QC-laser samples featuring doping profiles intentionally offset with respect to each other.

Finally, the waveguide cladding layers and their interfaces and electrical contacts need to be equally functional in both bias directions. We confirmed this using a sample with identical cladding, buffer and contact layers but without active regions and injectors [30]. The $I-V$ characteristics in both polarities were, in fact, equal within a few per cent.

The most striking device characteristics of a representative bi-directional QC laser are displayed in figure 40. The emission wavelength as a function of the heat-sink temperature is shown for both polarities. The two wavelengths at low temperature are $\lambda_- \approx 6.5 \mu\text{m}$ and $\lambda_+ \approx 6.33 \mu\text{m}$. These wavelengths, although clearly distinct from each other, are closer than the design wavelengths $\lambda_- \approx 7.17 \mu\text{m}$ and $\lambda_+ \approx 6.25 \mu\text{m}$. This discrepancy can easily be accounted for by noting that the transition energy is Stark shifted in a linear fashion by a variation of the applied electric field and that the device has a somewhat higher laser threshold voltage under negative bias. Nevertheless, the $L-I-V$ curves for both polarities are very similar in shape and magnitude, as expected from the bandstructure design. Before fabricating the asymmetric device, we tested the idea of bi-directionality on a symmetric structure. This allowed us to verify that QC lasers can, in fact, be equally operated in both bias directions and with arbitrarily close emission wavelength. The device characteristics confirmed that both bias polarities result in emission at the same wavelength, $\lambda_\pm \approx 6.75 \mu\text{m}$ at cryogenic temperatures. The laser displays a good threshold current density of $\sim 3.1 \text{ kA cm}^{-2}$. Peak optical powers of $\leq 300 \text{ mW}$ are achieved at cryogenic temperatures, as well as a maximum slope efficiency of $\leq 480 \text{ mW A}^{-1}$. The latter value is excellent, even in comparison with some of the best unidirectional QC lasers.

5.3. Injectorless quantum cascade laser

Despite their variety, all QC-laser designs until recently [77] have shared one characteristic: the presence of electron injectors interleaved with the active regions. This alternation of N_p (typically $N_p \sim 30$, but $N_p = 1$ to 100 has been demonstrated [25, 26, 30]) active regions with injectors is a hallmark of the QC laser. The injector regions extract the electrons from the lower states of one active region and inject them into the upper state of the laser transition of the following down-stream active region. In addition to transferring the electrons between active regions, the injectors are usually designed so as to favour electron relaxation down into the ground state, from which electrons are injected ‘cold’ [33] into the next active region. Finally they provide an electron reservoir (from modulation doping of the central injector region) for each successive active region to provide stable current flow under bias. In a typical QC-laser structure, active and injector regions are approximately of the same length of a few tens of nanometres.

We show here, however, that by using a double-QW superlattice (DQW-SL) active region [78], we are able to incorporate the essential features of the injector into the active region itself. Therewith, injector regions are no longer a firm requirement for QC lasers.

The DQW-SL active region in the conventional configuration with injector regions has recently been discussed extensively in [78]; here we only highlight its properties for the ‘injectorless’ QC laser.

First, and most important, by using the DQW-SL active region, two ‘flat’ minibands, with the laser transition occurring across the minigap between them and with spatially symmetric states, can be designed for any applied electric field. Thus we can choose the electric field so that the voltage drop across one active region is such that the bottom of its lower miniband is energetically aligned with the bottom of the upper miniband of the following active region, even without an intermediate injector.

Secondly, using the DQW-SL active region we can independently choose the applied electric field, the width of the lower miniband and the width of the minigap, the latter being equal to the laser photon energy. A wide lower miniband (energy width much larger than an optical phonon energy) allows electrons to quickly scatter out of the final state of the optical transition and ensures a negligible thermal population of the same state, which enhances the population inversion necessary for laser action.

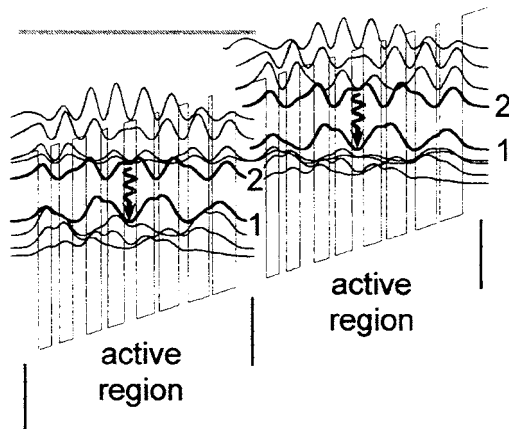


Figure 41. Conduction-band profile of two consecutive active regions and the moduli squared of the wavefunctions involved in the laser transition (2, 1) and other energy levels within the minibands of an injectorless QC laser. The shaded areas represent the minibands. The hatched line shows the lower edge of the third miniband. The wavy arrow indicates the laser transition. The layer thicknesses (in nanometres) for one active region starting at the leftmost barrier are **3.7/1.6/0.9/1.7/1.8/0.78/2.0/1.5/2.1/0.61/2.4/1.2/2.5/0.4/2.9**. The layers in bold are AlInAs, the others are InGaAs and the underlined layers are Si doped to $n = 3 \times 10^{17} \text{ cm}^{-3}$.

The foremost advantage of the injectorless QC laser is the larger optical confinement factor, i.e. the overlap of the waveguide mode with the active regions, which can now be achieved. Since the length (thickness) of the DQW-SL active region did not increase with respect to that in designs which use injectors, now approximately twice as many active regions can be concentrated into the same waveguide core and mode.

The conduction-band structure of two consecutive active regions and the moduli squared of the wavefunctions for an injectorless QC laser, designed for emission at $11.2 \mu\text{m}$, are shown in figure 41. The exact layer sequence is given in the caption.

We calculate an electron scattering time due to the emission of LO phonons of $\tau_{21} = 2.4 \text{ ps}$ between the upper and lower laser levels, which is much longer than the calculated total lifetime of level 1, $\tau_1 = 0.2 \text{ ps}$, thus ensuring strong population inversion. The total scattering lifetime of the upper laser level is calculated as $\tau_2 = 0.5 \text{ ps}$, and the optical dipole matrix element is $z_{21} = 3.5 \text{ nm}$.

The pulsed light output versus current ($L-I$) characteristics of a $24 \mu\text{m}$ wide stripe is shown in figure 42. The measured threshold current density J_{th} of this laser was 3.5 kA cm^{-2} at 7 K heat-sink temperature, increasing to 10.5 kA cm^{-2} at 195 K , its highest operating temperature. The slope efficiency was 225 mW A^{-1} at 7 K and the peak power 270 mW at 7 K and 10 mW at 195 K .

Using the calculated values of the optical dipole matrix element, scattering times, length ($L_a = 27.6 \text{ nm}$) of one active region, number ($N_a = 75$) of active regions and the measured width ($\gamma_{21} = 16 \text{ meV}$) of the luminescence spectrum we can estimate the low-temperature gain coefficient as 48 cm kA^{-1} . Using the measured value of the waveguide loss ($\alpha_w = 70 \text{ cm}^{-1}$) for a nominally identical waveguide, the mirror loss ($\alpha_m = 8.53 \text{ cm}^{-1}$) and the confinement factor ($\Gamma = 0.51$), a threshold current density of 3.2 kA cm^{-2} is estimated, which compares well with the measured value of 3.5 kA cm^{-2} .

6. High-speed operation of quantum cascade lasers

Ultrafast intersubband scattering rates ($\sim 1 \text{ ps}$) have major implications for the high-speed operation characteristics of QC lasers, which will be the focus of this section. Three efforts to develop QC-laser-based sources of ultra-short mid-infrared pulses are described: gain-switching, and active and passive mode locking. Pulses as short as a few picoseconds are obtained with repetition rates of $\sim 100 \text{ MHz}$ to $\sim 10 \text{ GHz}$. In future, such pulsed mid-infrared

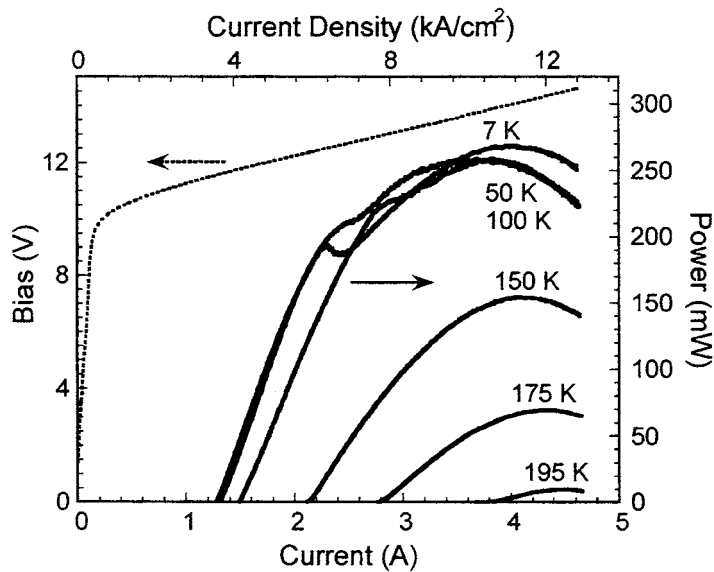


Figure 42. Pulsed peak optical power collected from a single facet (with near-unit collection efficiency) of a deep-etched stripe laser as a function of current for various heat-sink temperatures (solid curves), and voltage versus current characteristic at 7 K heat-sink temperature (dashed curve). The laser emits at $11.5\text{ }\mu\text{m}$ wavelength.

sources may be useful for time-resolved spectroscopy, as well as for the realization of high-speed infrared wireless communication systems.

6.1. Gain switching

Here we describe gain-switched QC lasers, which were used to generate light pulses with duration as short as $\sim 50\text{ ps}$ [79, 80]. Gain switching is a common technique for the generation of pico-second light pulses from injection lasers, which relies on the large buildup and subsequent rapid depletion of the gain-medium population inversion following a short-lived electrical excitation. Common driving sources include comb generators, avalanche transistor generators and photoconductive switches [81]. Gain switching has been successfully applied in the past to interband diode lasers, including mid-infrared lead salt lasers [81], for which a 400 ps (preamplifier-limited) pulse risetime was measured. Its main advantage lies in its inherent simplicity, since it does not require specially fabricated devices, or any external cavity configuration.

The QC lasers described here are gain switched with a comb generator as illustrated schematically in figure 43(a). When driven with a sinusoidal signal, a comb generator, consisting of a step-recovery diode packaged with filtering reactive elements, generates a short negative pulse at the onset of each negative half-cycle, by rapidly releasing the charge stored during the previous positive half-cycle. A commercial comb generator was driven with approximately $0.5\text{--}1\text{ W}$ of RF power from a low-phase-noise synthesized signal generator, giving rise to a train of electrical pulses, each with a FWHM of 90 ps or longer, and a peak amplitude of more than 20 V across a 50Ω load. The pulse repetition rate is set by the driving frequency at $\sim 100\text{ MHz}$. The output of the comb generator was then combined with a dc current in a standard bias ‘tee’ to operate the laser.

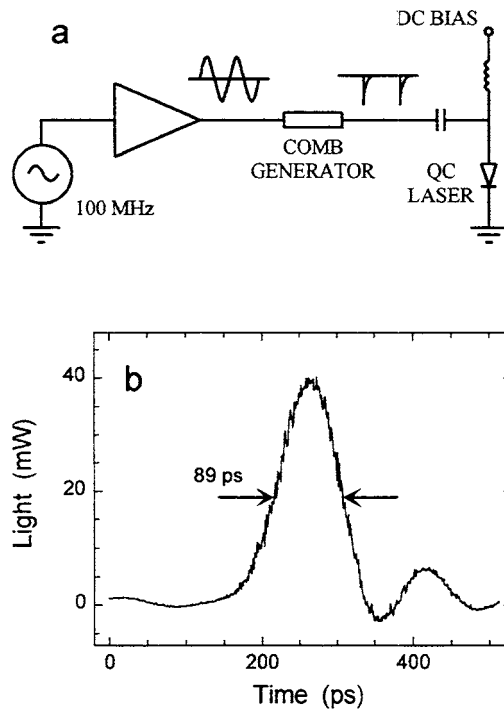


Figure 43. (a) Circuit diagram of the experimental setup used for gain-switching of QC lasers. The laser is driven with a 100 MHz train of \sim 100 ps pulses from the comb generator, combined with a dc current below the cw threshold. (b) Oscilloscope trace of a typical optical pulse generated by the gain-switched QC laser. The optical power has been corrected for the efficiency of the optics used to collect light from the QC laser (\sim 40%) and focus it onto the small QWIP area (\sim 20%).

Several QC lasers, emitting at \sim 8 and \sim 5 μ m wavelength and of the kind described in section 3.1, were gain switched with this approach. Early experiments used conventionally processed lasers [79] whereas improved measurements were performed with lasers optimized for high-speed operation using chalcogenide lateral claddings, as described in [80].

The dynamics of QC lasers is governed by the ultrafast carrier lifetime in these devices, which is comparable to the photon lifetime, a few picoseconds. Consequently, the population inversion overshoot following a current turn-on is strongly reduced, and the relaxation dynamics is expected to be overdamped. This implies that the optical pulse shape will follow more closely the electrical one above threshold, except for an initial delay in photon emission. An indication that this is the case is given by the observation of an increasing pulse width with increasing dc bias, since the larger the dc bias, the longer is the portion of the current pulse above threshold. In any case, infrared pulses of a few tens of picoseconds can be expected using faster comb generators or more sophisticated driving circuitry.

The QC laser is mounted inside a helium-flow cryostat and held at constant cryogenic temperature. The laser chip is bonded to one end of a 50 Ω microstrip transmission line, with several short wires used to reduce the bond inductance; a cryogenic semi-rigid cable, connected to the stripline with the appropriate adapter, is used to deliver the electrical pulses to the laser. Furthermore, the area of the laser top contact was strongly reduced, compared with conventional device processing, in order to reduce its parasitic capacitance. This latter modification directly led to the observation of shorter pulses, by more than 20%. However, the overall frequency response of the QC lasers without chalcogenide claddings remains strongly parasitics limited, to less than 3 GHz, which is nevertheless adequate for this experiment.

The light is collected with large-aperture ZnSe or Ge optics and focused onto a high-speed detector, either a HgCdTe photodiode or—for shorter pulses—a high-speed QW infrared photodetector (QWIP) [82]. The high-speed QWIP used in this work was provided by Liu

of NRC, Canada [83]. It is a GaAs–AlGaAs QWIP, grown by MBE, based on the bound-to-quasi-bound transition design [83]. The bandwidth of this detector is approximately 12 GHz, and it provides an impulse-response risetime of approximately 60 ps. Its high-speed properties are mainly limited by the package parasitics and, to a lesser extent, by its RC time constant. In fact, such bandwidth is rather slower, by a factor of three to four, than the estimated intrinsic response of similar devices [83].

Figure 43(b) shows experimental data of a QC laser held at a heat-sink temperature of 10 K and biased with a dc current of 200 mA, approximately 80% of its cw threshold value. The sinusoidal voltage driving the comb generator was adjusted to minimize the measured pulse widths. In particular, about 1 W of power at 99 MHz was used. From the trace in figure 43(b), an FWHM of 89 ps and a risetime of 71 ps are measured. Similar results are obtained as the current is increased toward the cw threshold.

Assuming a bandwidth risetime product of 0.35, and furthermore assuming that the squares of the risetimes of all components in the setup add to that of the optical pulse, we can extrapolate a value of 36 ps for the actual risetime of the optical pulse. In turn, assuming that the falltime also scales in a similar fashion, this suggests an actual FWHM value of the optical pulse of about 45 ps.

This is rather shorter than the widths of the electrical pulses used to drive the laser, by roughly a factor of two, or more, since the electrical pulses are likely broadened by the package and chip parasitics. The reason is the finite time required for stimulated emission to build up following the arrival of each electrical pulse.

6.2. Active mode locking

While gain-switching as a means to generate mid-infrared short pulses had been used before [81], another method—mode locking—had not yet been demonstrated in conventional mid-infrared semiconductor lasers. However, it is a common technique for near-infrared semiconductor lasers, where it is most often used together with an external cavity configuration [84].

Active mode locking of semiconductor lasers is achieved by modulating the laser current at the cavity roundtrip frequency, so that a large number of longitudinal modes are driven above threshold by the modulation sidebands of their neighbouring modes.

In this section, we discuss active mode locking of a QC laser, with estimated pulse widths of approximately 5 ps, and up to temperatures well above liquid nitrogen [85]. This is also the first example of an actively mode-locked mid-infrared laser. Since optimum performance of QC lasers is achieved with relatively long devices, typically 1.5–3 mm, an external cavity configuration is not necessary. Rather, a monolithic approach is more suitable, e.g. for a 3.75 mm long device we obtain a roundtrip frequency close to 12 GHz, well manageable with the available electronics. The advantage of the monolithic over the external cavity approach is obvious, including the mechanical stability and the fact that no high-quality anti-reflection coatings are needed on the laser.

The roundtrip frequency of 12 GHz is also rather lower than the predicted intrinsic modulation bandwidth of QC lasers. The ultrafast carrier lifetimes, limited to a few picoseconds by LO-phonon-assisted intersubband scattering, should allow intrinsic bandwidths exceeding 100 GHz [86]. The overall frequency response is then limited by package and chip parasitics. Therefore, we are using QC lasers with thick ($\sim 4 \mu\text{m}$) layers of a chalcogenide glass ($\text{Ge}_{0.25}\text{Se}_{0.75}$) as spacer layers between the top-contact metallization and the doped semiconductor ground-plane of the chip. This device layout has been described in detail in section 4.1. Its modulation response was found to remain relatively flat up to about 7 GHz.

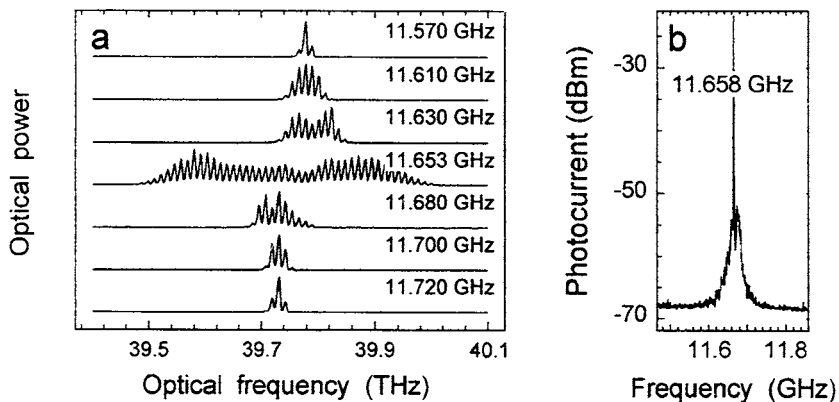


Figure 44. (a) Optical spectra of the actively mode-locked QC laser, at constant dc bias (900 mA) and heat-sink temperature (10 K), for different values of the RF drive frequency. (b) Power spectrum of the photocurrent generated by the mode-locked laser output in a high-speed QWIP at mode-locking resonance. The laser is biased with 1.1 A. The spectrum analyser resolution bandwidth is 30 kHz.

Given the estimated capacitance across the chalcogenide layer, $C \sim 19$ pF, and the measured differential resistance of the laser above threshold, $R < 1$ Ω , this indicates that the modulation response is still largely RC limited.

The QC laser material used is a state-of-the-art 8 μm wavelength structure, based on the ‘vertical’ transition design in a three-coupled-quantum-well active region and described in section 3.1. In the experiment, the laser is mounted inside a helium-flow cryostat, and driven with approximately 23 dB m of RF power from a low-phase-noise synthesized signal generator followed by a high-speed amplifier. A bias ‘tee’ at the input connector of the laser cryostat is used to combine this modulation with the direct dc bias. Direct evidence of mode locking is presented in figure 44(a), where we show several optical spectra of the laser output, corresponding to different values of the drive frequency near the laser roundtrip frequency, ~ 11.653 GHz, for this particular laser. In this measurement the laser was held at a heat-sink temperature of 10 K and biased with a dc current of 900 mA, approximately 11% above the cw threshold value and the RF signal was added. When the detuning between the RF drive frequency and the roundtrip resonance is sufficiently large, e.g. ~ 70 MHz, as in the top and bottom traces of figure 44(a), then the spectrum consists of a single laser mode with its modulation sidebands. As the detuning is decreased, more and more modes are brought above threshold by their neighbours’ sidebands, indicating effective mode locking; at resonance, the spectrum comprises more than 40 modes in this case. This behaviour was observed for the entire temperature range of cw operation of this device, up to over 120 K.

The phase-locked nature of these multimode spectra was verified by detecting the laser output with a fast ~ 12 GHz estimated bandwidth QWIP, as described in section 6.1, and displaying the resulting photocurrent on a spectrum analyser. Near resonance, we observed the feature shown in figure 44(b) for different values of the drive frequency. The sharp spike at the centre of this trace partly consists of a RF pick-up signal; the broad feature, on the other hand, comes entirely from the QWIP photocurrent, arising from the mutual beating of adjacent modes in the optical spectrum. This feature was found to be extremely stable, indicating negligible random drift of the modes’ relative phases, as expected with a mode-locked laser. The large spectral width of the pedestal, ≥ 100 MHz, is due to the variation of

the refractive index, and hence of the mode separation frequency, over the optical bandwidth.

Information about the temporal characteristics of the mode-locked waveform can be inferred from the linear auto-correlation traces generated by the Michelson interferometer inside the Fourier transform infrared (FTIR) spectrometer. The latter is customarily used for spectral characterization of the lasers. An example is shown in the inset of figure 44. If the light beam consists of ultra-short pulses, the interference fringes in the FTIR spectrometer traces can only occur when the pulses from the two arms of the interferometer temporally overlap on the detector, i.e. for delay times between the two arms shorter than the pulse width, or multiples of it. Then, the extremely small amplitude of the fringes observed in the inset of figure 44 for large delay times ≥ 10 ps indicates that the laser indeed emits a train of pulses with good modulation depth. However, these FTIR interferogram traces are not as useful as second-order auto-correlation traces, which, however, are beyond our present mid-infrared experimental capabilities.

An estimate of the pulse width can, however, also be obtained from the shape of the optical spectra, using a procedure first outlined in [87]. Following that [85, 87] results in a pulse width of $\tau_p \sim 5$ ps. This is an approximate result, primarily because it does not account for group-velocity dispersion; the latter, however, is likely to be important, especially at the larger values of the dc bias, due to the concomitant spectral broadening.

Nevertheless, assuming pulses of 5 ps duration, and the average power levels measured, we can infer peak powers at 80 K ranging from 40 to 720 mW for the range of bias currents of 1 to 1.7 A [85].

6.3. Evidence for passive mode locking

The previous two sections discussed ultra-short optical pulse generation in QC lasers that was induced by external factors, in particular a fast modulation of the drive current. However, under proper conditions, lasers in general may self-pulsate without the need for an oscillating external force. Self-mode locking induced by a saturable loss mechanism is one often-employed technique to induce such self-pulsation [88]. The pulse repetition frequency is—as in active mode locking—determined by the laser cavity length, and the pulse width by the particular nature, and specifically the response and recovery times, of the saturable absorption mechanism.

QC-lasers have been experimentally demonstrated to self-pulsate under certain conditions, which can be explained by a saturable loss mechanism, termed ‘self-focusing’ or ‘Kerr-lensing’, involving the optical Kerr-nonlinearity of the intersubband transition [10].

The latter is not only characterized by its ultra-fast relaxation times, but also by its extremely large optical nonlinearity [89]. Although large resonant nonlinearities are found in several other laser systems, their response is always much slower. The unique combination of giant magnitude and ultrafast dynamics of intersubband optical nonlinearities has recently attracted considerable attention, and several applications to high-speed optoelectronic devices have been proposed [90].

The QC-lasers of this study were based on the so-called three-well vertical-transition active regions described in section 3.1. They were conventionally processed (see section 4.1) except for their unusually long waveguides, ~ 3.5 mm. When cooled below their maximum temperature for cw operation, and over a wide range of dc bias, these lasers were found to emit an extremely broad (up to 1.5 THz, about 50% of the gain bandwidth) multimode spectrum, characterized by a smooth multi-peaked envelope. A series of these spectra is shown in figure 45(a), for a 3.5 mm long QC laser emitting around $8\text{ }\mu\text{m}$ wavelength at 80 K heat-sink temperature. At the same time, these devices were found to self-pulse at their cavity roundtrip

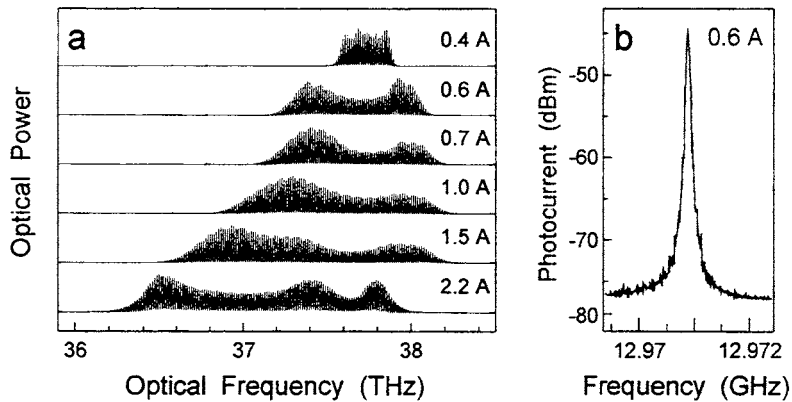


Figure 45. (a) Optical spectra of a 3.5 mm long, $8 \mu\text{m}$ wavelength QC laser held at 80 K heat-sink temperature, under conditions of self-mode locking. The spectra are shown for different values of the laser dc current as indicated. (b) RF spectrum of the photocurrent generated by the same laser (at a bias of 0.8 A) in a high-speed QWIP.

frequency. This was determined by detecting their output with a fast QWIP [83] and displaying the resulting photocurrent on a spectrum analyser, see figure 45(b). As in the active mode-locking case (see previous section 6.2) a clear feature centred at the laser roundtrip frequency (~ 13 GHz for the particular device of figure 45) was observed. Its peak power corresponds to a modulation amplitude of the observed laser light of at least 20% of the measured average optical power. This feature results from the mutual beating of adjacent modes in the optical spectrum. Its large magnitude, evident stability and narrow width (typically less than 100 kHz) indicate negligible random drift of the modes' relative phases, as expected in a mode-locked laser.

Another indicative test of pulsed emission is provided by the linear auto-correlation traces generated by the FTIR spectrometer. An example is shown for both an $8 \mu\text{m}$ and a $5 \mu\text{m}$ wavelength device in figure 46. The negligible amplitude of the FTIR signal between the clearly visible interference spikes suggests that these lasers are indeed emitting a train of ultra-short pulses with good modulation depth. The multi-peaked envelopes observed in the optical spectra of figure 45 are also consistent with pulsed emission and cannot otherwise be explained in terms of unlocked multimode emission, given the primarily homogeneously broadened narrow gain curves of these QC lasers (see figure 4). In particular, these structures are typical of short laser pulses undergoing strong self-phase modulation. These considerations can be used to estimate the width of these pulses resulting in $\tau_p \sim 3$ ps [87]. As in the actively mode-locked case, we emphasize that this is an approximate result, primarily because it does not account for group-velocity dispersion.

A pyro-electric detector was used to measure the emitted average power. The peak power of the pulses can then be estimated, given knowledge of their width and repetition rate: values ranging from several 100 mW to well over 1 W peak power were obtained.

The proposed self-mode locking mechanism is illustrated in figure 47, together with a schematic cross section of the QC waveguide structure and the lateral mode profile(s). If the nonlinear refractive index n_2 of the laser active material is positive, the centre part of the beam transverse profile, where the intensity is higher, experiences a larger refractive index relative to the edges. The resulting nonlinear dielectric waveguide increases the beam confinement near its centre and hence narrows the beam diameter to an extent proportional to the optical power.

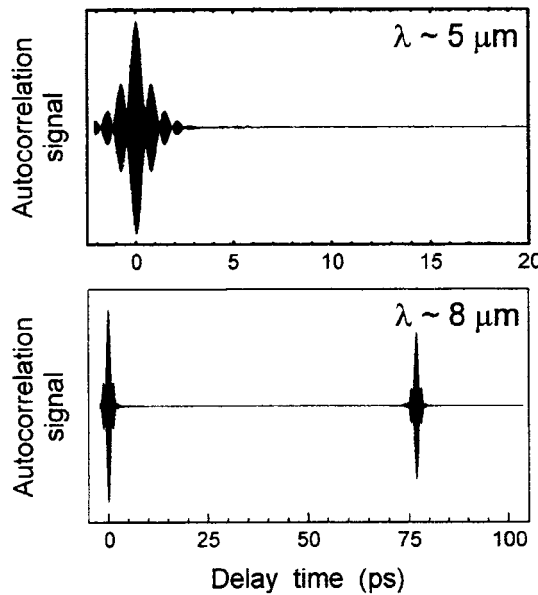


Figure 46. Linear auto-correlation traces of two QC lasers under conditions of self-mode locking: (top) a 3.75 mm long, 5 μm wavelength device held at 25 K heat-sink temperature and at a bias current of 1 A; (bottom) a 3.5 mm long, 8 μm wavelength device at 80 K (the laser of figure 45) also at a bias of 1 A. Note that the time-axes of the two parts of the figure are different.

This effect is known as self-focusing or Kerr lensing [91]. A smaller beam diameter in turn leads to a decreased mode interaction with the external, metallic contact pads. In particular, it reduces the beam coupling to the high-loss surface plasmon mode at the metal–dielectric interface, which is a major source of waveguide losses in QC lasers (see section 4.3). The net result is a decrease in the optical losses with increasing intensity, a so-called saturable loss mechanism, which is the fundamental ingredient for self-mode locking [88]. In the presence of such a mechanism, it becomes favourable for the laser to emit ultra-short pulses because of their higher instantaneous intensity, and hence lower losses, relative to cw emission, where the output energy is spread uniformly in time.

For additional evidence of self-mode locking by Kerr lensing, the far-field beam profile was measured under cw and self-mode-locked operation [10]. In this experiment an 8 μm QC laser was used, in which self-mode locking was found to be non-self-starting but self-sustaining. This device exhibits single-mode cw emission when dc biased; mode locking can be achieved by modulating the current at its roundtrip frequency, as in active mode locking (see previous section). However, the laser then remains in the mode-locked state even after the modulation is switched off. This laser is ideally suited to this measurement, because it allows us to compare the results obtained at the same bias, temperature and so forth under both cw and self-mode-locked conditions. The far-field beam profile under self-mode locking is, in fact, broader than under cw operation, by more than 10%, corresponding to a narrower beam inside the waveguide. Therefore, at the higher instantaneous power levels inherent to pulsed emission, the beam does undergo self-focusing. The narrowing in beam diameter between cw and self-mode-locked operation was found to increase with dc bias and hence optical intensity, also consistent with Kerr lensing.

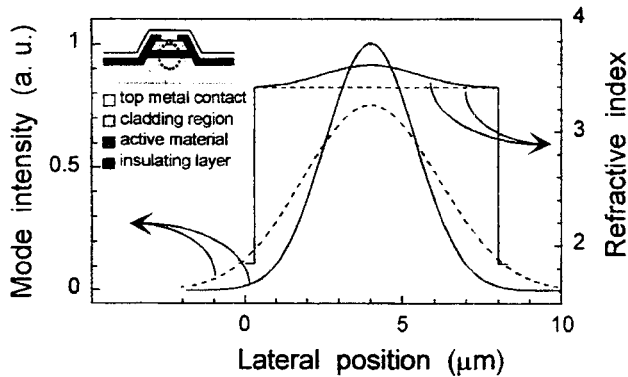


Figure 47. Refractive index profile and resulting intensity distribution of the fundamental waveguide mode along the lateral direction of a conventional, deep-etched QC-laser waveguide. A schematic cross-section of the laser waveguide is shown in the inset. Self-focusing occurs in the lateral direction due to the strong index nonlinearity of the active region: if the intensity increases (as in going from the dashed to the solid curves) the index near the centre of the waveguide increases, and the mode is correspondingly more tightly confined.

7. Application to trace-gas detection by optical methods in the mid-infrared

While optical data-storage evolves towards blue lasers, and optical communications around near-infrared wavelengths, the mid-infrared wavelength range, ranging from ~ 3.5 to $13\ \mu\text{m}$, attracts a lot of attention for trace-gas sensing applications. As noted before, most trace gases of importance, from byproducts of fossil fuel burning to constituents of human breath, have telltale absorption features in this wavelength range—their ‘finger-print’ region of the spectrum—as a result of molecular rotational-vibrational transitions. Narrow-linewidth, tunable semiconductor lasers in this wavelength range are used to spectrally map out and qualitatively and quantitatively detect these trace gases, by a measurement technique called ‘tunable infrared laser diode absorption spectroscopy (TILDAS)’ [92]. The advantage of TILDAS is its high sensitivity and specificity, usually combined with the advantages of the solid state device approach, i.e. the compactness and robustness of a packaged semiconductor laser device.

Soon after single-mode tunable QC-DFB lasers of the kind described in section 4.2 were invented [5], they were put into action for sensing applications [8]. At present, more than ten research groups have reported successful demonstrations of the latter using a large variety of spectroscopic methods. The lasers are typically used under two quite distinct operating conditions, cw at liquid nitrogen temperatures, or pulsed close to RT. The former has the advantage of a very narrow linewidth [93], which is essential for high-resolution spectroscopy of trace gases at low pressure; however, it carries the inconvenience of the need for cryo-cooling. QC-DFB lasers operated in pulsed mode have a broadened emission line due to the thermal chirp from the current pulse; they are, nevertheless, useful for the spectroscopy of pressure-broadened gas samples. The following sections 7.2–7.5 will present several of those results and the introductory section 7.1 will briefly summarize the tuning characteristics of QC-DFB lasers.

7.1. Single-mode tuning of distributed feedback lasers

Section 4.2 described several ways to achieve single-mode operation for QC-DFB lasers. In essence, a grating with period Λ is incorporated into the waveguide, which lowers the threshold gain—by reducing the outcoupling loss—for a distinct wavelength close to the Bragg

wavelength $\lambda_B = 2 \cdot n_{\text{eff}}(T) \cdot \Lambda$. Here, n_{eff} , the effective refractive index of the waveguide mode, is explicitly expressed as being a function of temperature. The latter is a result of the refractive index of every component of the waveguide being temperature dependent. Therefore, a temperature change in the laser will automatically lead to a wavelength shift; with increasing temperature to longer wavelengths.

Changing the heat-sink temperature can certainly control the laser temperature; however, this process is slow, as it typically involves adiabatically changing the temperature of a quite large volume. The more common approach to temperature tuning QC lasers is through adding a dc current-ramp to the laser drive current. A larger current dissipates more heat in the laser and, therefore, very locally changes the temperature. Since a much smaller volume is involved, rapid temperature cycling, with rates around several 10 kHz, is possible.

Figure 30 shows two examples of QC-DFB lasers tuned with current while being held at different heat-sink temperatures. The tuning rates increase with heat-sink temperature and current from 0.3 to 0.4 nm K⁻¹, for a laser emitting around $\lambda_0 \sim 5.2 \mu\text{m}$, and from 0.4 to 0.65 nm K⁻¹, for a laser around 8 μm wavelength. The tuning with current is also noticeably nonlinear (quadratic). For $\lambda_0 \sim 5 \mu\text{m}$, the tuning coefficient increases from 20 to 35 nm A⁻¹ over the range shown in figure 30. For $\lambda_0 \sim 8 \mu\text{m}$ it increases from 20 to 40 nm A⁻¹.

Typical total tuning ranges per current sweep are around 0.3–0.5% of the emission wavelength, i.e. a few wavenumbers, which allows us to scan typically several—often up to ten—isolated absorption features of a trace-gas solution [94, 95].

7.2. Direct and modulated absorption measurements

Namjou *et al* [8] at Stevens Institute of Technology, NJ, used pulsed QC-DFB lasers at near-RT conditions to measure mid-IR ($\lambda \sim 7.8 \mu\text{m}$) absorption spectra of N₂O and CH₄ diluted in N₂ (prepared in a 10 cm long single-pass gas cell) using a measurement technique known as wavelength-modulation spectroscopy. The noise equivalent sensitivity limit of the measurement was 50 ppm. This was also the first example of QC-DFB lasers being used for trace-gas detection.

Sharpe *et al* [94] at the Pacific Northwest National Laboratory (PNNL), WA, conducted high-resolution, Doppler-limited, direct absorption measurements of NO and NH₃ using QC-DFB lasers at 5.2 and 8.5 μm , respectively. The laser drive current was a saw-tooth ratchet with 6–11 kHz repetition rate; with the rising current the laser would tune $\sim 2.5 \text{ cm}^{-1}$, covering e.g. 11 absorption features of NH₃. The noise equivalent sensitivity limit in these measurements was 3×10^{-6} absorbance.

Kosterev *et al* [96] used a QC-DFB laser around 8.1 μm to detect various isotopes of methane (CH₄, CH₃D and ¹³CH₄). They achieved a measurement accuracy of ± 0.5 ppm at a concentration of 15.6 ppm, and a minimum detectable absorption of $\sim 1 \times 10^{-4}$.

Williams *et al* [97] at PNNL in collaboration with Taubman and Hall at JILA, CO, measured the intrinsic linewidth of several QC-DFB lasers around 8 μm wavelength by observing fluctuation of the collected optical intensity when the laser light was passing through a sample cell containing a gas (N₂O) with well known absorption features with the laser being tuned to the side of one such absorption line. This resulted in a linewidth of $\sim 1 \text{ MHz}$ over $\sim 1 \text{ ms}$ integration time. The laser could furthermore be electronically stabilized (and locked to the N₂O absorption feature) by using the detector signal as feedback to the drive current. The thus-stabilized lasers had linewidths <20 kHz, which is very narrow for any as-cleaved semiconductor-DFB laser.

Kosterev *et al* [95] at Rice University developed a variable-duty-cycle, quasi-cw frequency scanning technique for QC-DFB lasers, which mitigates many of the thermally induced effects

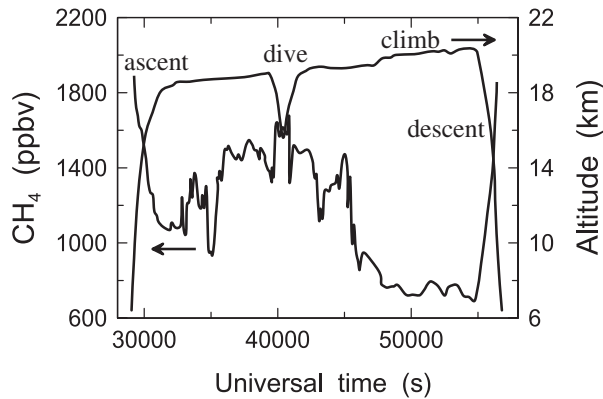


Figure 48. Flight data for methane concentration measurements over Sweden and Russia during ascent, dive, climb, and descent for the 11 March 2000 flight under the NASA SOLVE mission.

of pulsed operation. Combined with a 100 m multi-pass gas cell and zero-air background subtraction, a detection sensitivity close to the ppb concentration level was achieved. Around $7.9\text{ }\mu\text{m}$ wavelength various natural constituents of air were measured as well as ethanol ($\text{C}_2\text{H}_5\text{OH}$) vapour. The latter was detected at concentrations as low as 125 ppb.

In another work, Kosterev *et al* [98] described very short- (5 ns) duration pulse operation of QC-DFB lasers, which led to nearly transform-limited broadening of the laser pulses. This serves as an example of the optimal use of pulsed QC-DFB lasers in trace-gas sensing applications.

Finally, Webster *et al* [99] reported the first atmospheric measurements using QC-DFB lasers. The devices were flown on NASA's ER-2 high-altitude aircraft to monitor stratospheric methane and nitrous oxide over North America, Scandinavia and Russia, see figure 48. The sensitivity limit for methane was ~ 2 ppb.

7.3. Cavity ring-down spectroscopy

Paldus [101] at Informed Diagnostics and coworkers reported the use of a cw operated QC-DFB laser around $8.5\text{ }\mu\text{m}$ wavelength for cavity ring-down (CRD) spectroscopy of ammonia (NH_3) diluted in nitrogen. A noise equivalent absorbance of $3.4 \times 10^{-9}\text{ cm}^{-1}\text{ Hz}^{-1/2}$ was achieved, which corresponds to a detection limit of 0.25 ppbv.

7.4. Photo-acoustic spectroscopy

Paldus *et al* [102] at Stanford University, CA, together with Oomens *et al* at the University of Nijmegen, The Netherlands, reported photo-acoustic (PA) spectroscopy on NH_3 and H_2O diluted in N_2 using a cw QC-DFB laser emitting at $8.5\text{ }\mu\text{m}$ wavelength. The noise-limited minimum detectable concentration of NH_3 was 100 ppbv for 1 s integration time. PA spectroscopy is based on the incident power absorbed by the trace gas (rather than the power transmitted); it is therefore particularly sensitive, if a high-power light source is used. This clearly favours the use of QC lasers over other low-optical-power mid-infrared semiconductor lasers.

Nagele *et al* [103] built a multi-component (ethane, methanol, ethanol) trace-gas monitoring system using QC lasers as pump sources and a resonant multi-pass PA cell.

7.5. Other types of spectroscopy

Remillard *et al* [104] at Ford Research Laboratories used a cw-operated QC-DFB laser around $\lambda_0 \sim 5.2 \mu\text{m}$ to obtain sub-Doppler resolution-limited saturation features in a Lamb-dip experiment on NO. The Lamb-dips appear as transmission spikes with FWHM values around 4.3 MHz. This makes the 73 MHz wide Λ -doubling of the R(13.5)_{3/2} line easily visible beneath the 130 MHz Doppler broadening of the line.

Gittins *et al* [105] at Physical Sciences Inc., used a multi-mode Fabry–Perot type QC laser around 8.0 μm wavelength for quantitative backscatter absorption measurements on isopropanol vapour. They developed and employed a pseudo-random code modulation of the QC laser, and explored its use for differential absorption lidar (DIAL). Even a simple measurement configuration resulted in a detection limit of 12 ppmv or $\sim 3 \times 10^{-3}$ absorption.

Sonnenfroh and coworkers [106] used QC-DFB lasers around 5.4 μm in quasi-cw mode close to RT in conjunction with a balanced ratiometric detection technique to achieve high sensitivity.

Finally, Hvozdara *et al* [107] demonstrated the first use of a GaAs-based QC laser for gas-sensing applications. Their system included a hollow waveguide gas cell through which different mixtures of ethene in helium were flowed. An FTIR spectrometer was used as detector and spectral analyser and the QC laser emitting around 10 μm wavelength took the place of the spectrometer's light source.

8. Conclusion and outlook

Since their first experimental demonstration approximately seven years ago, QC-lasers have rapidly progressed, and their device performance to date has reached impressive quality, with wavelengths spanning the entire mid-infrared wavelength range from 3.5 to 24 μm . RT operation in pulsed mode is achieved over a large portion of this spectrum. QC-DFB lasers already have already been used amply in trace-gas sensing experiments. Recent advances [12, 108] make it appear likely that at least RT-cw operation will be reached in the near future. This breakthrough will have major impact on most applications.

Major challenges for QC laser research are the extension of the wavelength range into the far-infra-red beyond $\lambda_0 > 50 \mu\text{m}$ on one hand [13, 109], and to fibre-optic wavelengths, on the other hand [14, 110]. The former is challenging as population inversion is difficult to attain for such long wavelengths. Energy levels are generally so close that selective injection into a single level is difficult. Furthermore, LO-phonon scattering is replaced by electron–electron scattering as the dominant electron relaxation mechanism, which is in itself more difficult to model accurately. Finally, waveguide losses are expected to be very high. Nevertheless, even very low temperature QC-laser operation would be a major accomplishment due to the lack of narrow band and high power compact sources in the far-infrared wavelength range.

QC lasers, or intersubband-based opto-electronic components in general, are of considerable interest [110] due to their intrinsic high-speed capabilities and predicted low linear chirp. The challenge to achieve 1.3–1.55 μm intersubband laser action lies mainly in finding and optimizing a material system with sufficient band offset to accommodate the large energy level spacing (800 meV for 1.55 μm wavelength).

The quest for shorter wavelengths is one motivation for a more varied selection of materials [111]. We believe, however, that the wide range of device possibilities and physics questions that have been opened by the creative use of band-structure engineering and MBE—as so well demonstrated in QC lasers—are motivating in themselves and will globally grow into numerous research and development efforts.

Acknowledgments

We would like to thank our collaborators and colleagues for their contributions and countless stimulating discussions. Thanks in particular to R Colombelli, G Scamarcio, A Tredicucci, and M C Wanke for their contributions to superlattice quantum cascade lasers, C G Bethea, H Y Hwang, R Martini and R Paiella, for their contributions to the high-speed measurements, J N Baillargeon, R Köhler, and A Straub for their help with distributed feedback quantum cascade lasers. J Faist and C Sirtori were essential to the success of the lasers in the early phase.

We would particularly like to thank M I Blakey, S N G Chu, A L Hutchinson and A M Sergent for their help with processing and material characterization. E E Narimanov took an essential role in explaining the mode behaviour of deformed QC cylinder lasers; and we are grateful to H C Liu for providing the high-speed QW infrared photodetectors.

The positive and encouraging feedback received from numerous users of QC-DFB lasers on the lasers' performance in trace-gas sensing applications motivated a large portion of this work.

We finally would like to acknowledge support by DARPA/US ARO under contract number DAAD19-00-C-0096.

References

- [1] Kazarinov R *et al* 1971 *Fiz. Tekh. Poluprov.* **5** 797–800
- [2] Faist J *et al* 1994 *Science* **264** 553–6
Capasso F *et al* 1999 *Phys. World* **12** 27–33
- [3] Faist J *et al* 1995 *Appl. Phys. Lett.* **67** 3057–9
Faist J *et al* 1995 *Appl. Phys. Lett.* **66** 538–40
- [4] Faist J *et al* 1996 *Appl. Phys. Lett.* **68** 3680–2
- [5] Faist J *et al* 1997 *Appl. Phys. Lett.* **70** 2670–2
- [6] Scamarcio G *et al* 1998 *Semicond. Sci. Technol.* **13** 1333–9
Scamarcio G *et al* 1997 *Science* **276** 773–6
- [7] Gmachl C *et al* 1998 *Science* **280** 1556–64
- [8] Namjou K *et al* 1998 *Opt. Lett.* **23** 219–21
- [9] Sirtori C *et al* 1998 *Appl. Phys. Lett.* **73** 3486–8
- [10] Paiella R *et al* 2000 *Science* **290** 1739–42
- [11] Colombelli R *et al* 2001 *Appl. Phys. Lett.* **78** 2620–2
- [12] Hofstetter D *et al* 2001 *Appl. Phys. Lett.* **78** 1964–6
- [13] Rochat M *et al* 1998 *Appl. Phys. Lett.* **73** 3724–6
- [14] Gmachl C *et al* 2000 *Appl. Phys. Lett.* **77** 3893–5
- [15] Sirtori C *et al* 2001 *Appl. Phys. Lett.* **78** 1029–31
- [16] Dehlinger G *et al* 2000 *Science* **290** 2277–9
- [17] Yang R Q 1994 *Proc. 7th Int. Conf. on Superlattices, Microstructures and Microdevices (Banff, 1994)*
Yang R Q *et al* 2001 *IEEE J. Quantum Electron.* **37** 282–9
Yang R Q *et al* 1997 *Appl. Phys. Lett.* **71** 2409–11
- [18] Lin C-H *et al* 2000 *Proc. SPIE* **3947** 122–8
Bruno J D *et al* 2000 *Appl. Phys. Lett.* **76** 3167–9
Olafsen C J *et al* 1998 *Appl. Phys. Lett.* **72** 2370–2
Felix C L *et al* 1997 *IEEE Photon. Technol. Lett.* **9** 1433–5
- [19] Knoll W *et al* 2001 *Electron. Lett.* **37** 31–3
Schmid W *et al* 1998 *Electron. Lett.* **34** 553–5
Garcia J Ch *et al* 1997 *Appl. Phys. Lett.* **71** 3752–4
- [20] Gauthier-Lafaye O *et al* 1999 *Appl. Phys. Lett.* **74** 1537–9
Julien F H *et al* 1995 *Electron. Lett.* **31** 838–9
- [21] Felix C L *et al* 2001 *Appl. Opt.* **40** 806–11
Bartolo R E *et al* 2000 *Appl. Phys. Lett.* **76** 3164–6

- Lane B *et al* 2000 *J. Cryst. Growth* **221** 679–82
Garbuзов D *et al* 1999 *Appl. Phys. Lett.* **74** 2990–2
Bewley W W *et al* *Appl. Phys. Lett.* **74** 1075–7
Hodges M *et al* 1999 *SPIE Proc.* **3628** 113–21
Lane B *et al* 1999 *Appl. Phys. Lett.* **74** 3438–40
Choi H K *et al* 1998 *SPIE Proc.* **3284** 268–73
Maurus Tacke 1995 *Infrared Phys. Technol.* **36** 447–63
[22] Martini R *et al* 2001 *Electron. Lett.* **37** 191–3
[23] Capasso F 1987 *Science* **235** 172–6
[24] Cho A Y (ed) 1994 *Molecular Beam Epitaxy* (Woodbury, NY: AIP)
[25] Gmachl C *et al* 1998 *Appl. Phys. Lett.* **73** 3830–2
[26] Capasso F *et al* 2000 *IEEE J. Sel. Top. Quantum Electron.* **6** 931–47
[27] Yu P Y and Cardona M 1999 *Fundamentals of Semiconductors: Physics and Materials Properties* (New York: Springer)
[28] Gelmont B *et al* 1996 *Appl. Phys. Lett.* **68** 2171–3
[29] Faist J *et al* 1998 *IEEE Photon. Technol. Lett.* **10** 1100–2
[30] Gmachl C *et al* 1999 *IEEE J. Sel. Top. Quantum Electron.* **5** 808–16
[31] Sirtori C *et al* 1998 *IEEE J. Quantum Electron.* **34** 1772–4
[32] Scamarcio G *et al* 2001 *Electron. Lett.* **37** 295–6
Wilson L R *et al* 1999 *Appl. Phys. Lett.* **75** 2079–81
[33] Troccoli M *et al* 2000 *Appl. Phys. Lett.* **77** 1088–90
[34] Gmachl C *et al* 1998 *Appl. Phys. Lett.* **72** 3130–2
[35] Hakki B W *et al* 1974 *J. Appl. Phys.* **46** 1299–306
[36] Köhler R *et al* 2000 *Appl. Phys. Lett.* **76** 1092–4
[37] Faist J *et al* 1998 *Appl. Phys. Lett.* **72** 680–2
[38] Faist J *et al* 1996 *Phys. Rev. Lett.* **76** 411–4
[39] Helm M 1995 *Semicond. Sci. Technol.* **10** 557–75
[40] Tredicucci A *et al* 1998 *Appl. Phys. Lett.* **72** 2388–90
[41] Tredicucci A *et al* 2000 *IEEE Photon. Technol. Lett.* **12** 260–2
[42] Capasso F 1986 *Annu. Rev. Mater. Sci.* **16** 263–91
[43] Tredicucci A *et al* 2000 *Electron. Lett.* **36** 876–8
Capasso F *et al* 1999 *IEEE J. Sel. Top. Quantum Electron.* **5** 792–807
Tredicucci A *et al* 1998 *Appl. Phys. Lett.* **73** 2101–3
[44] Gmachl C *et al* 1999 *IEEE Photon. Technol. Lett.* **11** 1369–71
[45] Tredicucci A *et al* 1999 *Appl. Phys. Lett.* **74** 638–40
[46] Tredicucci A *et al* 2000 *Appl. Phys. Lett.* **77** 2286–8
[47] Colombelli R *et al* 2001 *Appl. Phys. Lett.* **78** 2620–2
Gianordoli S *et al* 2000 *Appl. Phys. Lett.* **76** 3361–3
Gianordoli S *et al* 2000 *IEEE Photon. Technol. Lett.* **12** 1144–6
Slivken S *et al* 1999 *Appl. Phys. Lett.* **74** 2758–60
Li A Z *et al* 1998 *J. Cryst. Growth* **201–2** 901–4
[48] Ferreira R *et al* 1998 *Phys. Rev. B* **40** 1074–86
[49] Faist J *et al* 2001 *Appl. Phys. Lett.* **78** 147–9
[50] Faist J *et al* 1997 *Nature* **387** 777–82
[51] Gmachl C *et al* 1999 *Science* **286** 749–52
[52] Sirtori C *et al* 1995 *Appl. Phys. Lett.* **66** 3242–4
[53] Wilson L R *et al* 2001 *Appl. Phys. Lett.* **78** 413–15
Becker C *et al* 2000 *Appl. Phys. Lett.* **77** 463–5
Wilson L R *et al* 2000 *Appl. Phys. Lett.* **76** 1801–3
Page H *et al* 1999 *Electron. Lett.* **35** 1848–9
Strasser G *et al* 1999 *Appl. Phys. Lett.* **75** 1345–7
Sirtori C *et al* 1999 *Appl. Phys. Lett.* **75** 3911–13
[54] Faist J *et al* 2000 *IEEE Photon. Technol. Lett.* **12** 263–5
[55] Beck M *et al* 1998 *Proc. SPIE* **3284** 231–6
[56] Farmer C D *et al* 2000 *Appl. Phys. Lett.* **77** 25–7
[57] Gmachl C *et al* 2001 *IEEE Photon. Technol. Lett.* **13** 182–4
[58] Kokorina V F 1996 *Glasses for Infrared Optics* (Boca Raton, FL: Chemical Rubber Company)
[59] Paiella R *et al* 2001 *Appl. Phys. Lett.* **79** 2526–8

- Paiella R *et al* 2000 *Appl. Phys. Lett.* **77** 169–71
- [60] Gmachl C *et al* 1997 *IEEE Photon. Technol. Lett.* **9** 1090–2
- [61] Schrenk W *et al* 2000 *Appl. Phys. Lett.* **76** 253–5
Schrenk W *et al* 2000 *Appl. Phys. Lett.* **77** 2086–8
Schrenk W *et al* 2000 *Appl. Phys. Lett.* **77** 3328–30
Hvozdara L *et al* 2000 *Appl. Phys. Lett.* **77** 780–6
- [62] Finger N *et al* 1998 *IEEE J. Quantum Electron.* **36** 1366–8
Kogelnik H *et al* 1972 *J. Appl. Phys.* **43** 2327–35
Morthier G and Vankwinkelberge P 1997 *Handbook of Distributed Feedback Laser Diodes* (Boston, MA: Artech)
- [63] Köhler R *et al* 2000 *IEEE Photon. Technol. Lett.* **12** 474–6
- [64] Gmachl C *et al* 2000 *Opt. Lett.* **25** 230–2
Gmachl C *et al* 1998 *Appl. Phys. Lett.* **72** 1430–2
- [65] Tredicucci A *et al* 2000 *Appl. Phys. Lett.* **76** 2164–6
- [66] Hofstetter D *et al* 1999 *Appl. Phys. Lett.* **75** 665–7
- [67] Hofstetter D *et al* 1999 *Appl. Phys. Lett.* **75** 3769–71
- [68] Sirtori C *et al* 1998 *Opt. Lett.* **23** 1366–8
- [69] Kuwata-Gonokami M *et al* 1995 *Opt. Lett.* **20** 2093–5
- [70] Faist J *et al* 1996 *Appl. Phys. Lett.* **69** 2456–8
- [71] Gmachl C *et al* 1997 *IEEE J. Quantum Electron.* **33** 1567–73
- [72] Tredicucci A *et al* 2000 *Electron. Lett.* **36** 328–30
- [73] Narimanov *et al* 1999 *Phys. Rev. Lett.* **83** 4991–4
Noeckel *et al* 1997 *Nature* **385** 45–7
- [74] Gianordoli S *et al* 2000 *IEEE J. Quantum Electron.* **36** 458–64
- [75] Sirtori C *et al* 1998 *Opt. Lett.* **23** 463–5
- [76] Colombelli R *et al* 2000 *Appl. Phys. Lett.* **77** 3893–5
Tredicucci A *et al* 1998 *Nature* **396** 350–3
- [77] Wanke M C *et al* 2001 *Appl. Phys. Lett.* at press
- [78] Wanke M C *et al* 2001 *IEEE Photon. Technol. Lett.* **13** 278–80
- [79] Paiella R *et al* 1999 *Appl. Phys. Lett.* **75** 2536–8
- [80] Paiella R *et al* 2000 *IEEE Photon. Technol. Lett.* **12** 780–2
- [81] Bethea C G *et al* 1989 *Appl. Phys. Lett.* **66** 963–5
Lin C *et al* 1980 *Electron. Lett.* **16** 600–1
- [82] Levine B F 1993 *J. Appl. Phys.* **74** R1–81
- [83] Liu H C *et al* 1996 *IEEE J. Quantum Electron.* **32** 1024–8
- [84] Yariv A 1991 *Optical Electronics* (Philadelphia, PA: Saunders)
Kuijenga D J *et al* 1970 *IEEE J. Quantum Electron.* **6** 694–708
- [85] Paiella R *et al* 2000 *Appl. Phys. Lett.* **77** 169–71
- [86] Mustafa N *et al* 1999 *IEEE Photon. Technol. Lett.* **11** 527–9
- [87] Lin C H *et al* 1972 *IEEE J. Quantum Electron.* **77** 429–30
- [88] Spuhler G J *et al* 2001 *Appl. Phys. Lett.* **78** 2733–5
Sutter D H *et al* 1999 *Opt. Lett.* **24** 631–3
Jacobovitz-Veselka G R *et al* 1992 *Opt. Lett.* **17** 1791–2
- [89] Rosenthaler E *et al* 1996 *Science* **271** 168–73
Capasso F *et al* 1994 *IEEE J. Quantum Electron.* **30** 1313–26
Fejer M M *et al* 1989 *Phys. Rev. Lett.* **62** 1041–4
- [90] Akiyama T *et al* 2000 *Electron. Lett.* **36** 362–4
Neogi A *et al* 1999 *J. Appl. Phys.* **85** 3352–8
Segev M *et al* 1992 *Appl. Phys. Lett.* **61** 2403–5
- [91] Boyd R W 1992 *Nonlinear Optics* (San Diego, CA: Academic)
- [92] Schiff H I, Mackay G I and Bechara J 1994 *Air Monitoring by Spectroscopic Techniques* ed M W Sigrist (New York: Wiley-Interscience)
- [93] Myers T *et al* 2001 *Opt. Lett.* accepted
Williams R M *et al* 1999 *Opt. Lett.* **24** 1844–6
- [94] Sharpe S W *et al* 1998 *Opt. Lett.* **23** 1396–8
- [95] Kosterev A A *et al* 2000 *Appl. Opt.* **39** 4425–30
Gmachl C *et al* 2000 *IEEE Circuits Devices* **16** 10–18
- [96] Kosterev A A *et al* 1999 *Opt. Lett.* **24** 1762–4

- [97] Williams R M *et al* 1999 *Opt. Lett.* **24** 1844–6
- [98] Kosterev A A *et al* 2000 *Appl. Opt.* **39** 6866–72
- [99] Webster C R *et al* 2001 *Appl. Opt.* **40** 321–6
- [100] Paldus B A *et al* 2000 *Opt. Lett.* **25** 666–8
- [101] Baldus B A *et al* 2000 *Opt. Lett.* **25** 666–8
- [102] Paldus B A *et al* 1999 *Opt. Lett.* **24** 178–80
- [103] Nagele M *et al* 2000 *CLEO Europe Conf. Digest*
- [104] Remillard J T *et al* 2000 *Opt. Express* **7** 243–8
Samman A *et al* 2000 *IEEE Vehicular Technology Conf. 2000 Proc.* vol 5 pp 2084–9
- [105] Gittens C M *et al* 2000 *Opt. Lett.* **25** 1162–4
- [106] Sonnenfroh D M *et al* 2001 *Appl. Opt.* **40** 812–20
- [107] Hvozdara L *et al* 2000 *Appl. Opt.* **39** 6926–30
- [108] Hofstetter D *et al* 2001 *Appl. Phys. Lett.* **78** 396–8
Spagnolo V *et al* 2001 *Appl. Phys. Lett.* **78** 2095–7
Tahraoui A *et al* 2001 *Appl. Phys. Lett.* **78** 416–18
Hofstetter D *et al* 2000 *IEEE Photon. Technol. Lett.* **12** 1610–12
Matlis A *et al* 2000 *Appl. Phys. Lett.* **77** 1741–3
Gmachl C *et al* 2000 *Electron. Lett.* **36** 723–5
Slivken S *et al* 1999 *Appl. Phys. Lett.* **74** 173–5
- [109] Rochat M *et al* 2001 *Appl. Phys. Lett.* **78** 1967–9
Ulrich J *et al* 2000 *Appl. Phys. Lett.* **77** 1928–30
Ulrich J *et al* 2000 *Appl. Phys. Lett.* **76** 19–21
- [110] Gmachl C *et al* 2001 *Electron. Lett.* **37** 378–80
Iizuka N *et al* 2000 *Appl. Phys. Lett.* **77** 648–50
Neogi A *et al* 1999 *IEEE Photon. Technol. Lett.* **11** 632–4
Jancu J M *et al* 1998 *Appl. Phys. Lett.* **73** 2621–3
- [111] Akimoto R *et al* 2001 *Appl. Phys. Lett.* **78** 580–2
Garcia C P *et al* 2000 *Appl. Phys. Lett.* **77** 3767–9
Iizuka N *et al* 2000 *Appl. Phys. Lett.* **77** 648–50
Gmachl C *et al* 2000 *Appl. Phys. Lett.* **77** 334–6
Mozume T *et al* 1998 *Proc. 25th Int. Symp. on Compound Semiconductors (Nara, 1998)* (Bristol: Institute of Physics Publishing) pp 131–6
Suzuki N *et al* 1997 *Japan. J. Appl. Phys.* **36** L1006–8